

1998

Gamma-ray imaging detector for small animal research

Andrew Gerard Weisenberger
College of William & Mary - Arts & Sciences

Follow this and additional works at: <https://scholarworks.wm.edu/etd>



Part of the [Biomedical Engineering and Bioengineering Commons](#), and the [Investigative Techniques Commons](#)

Recommended Citation

Weisenberger, Andrew Gerard, "Gamma-ray imaging detector for small animal research" (1998).
Dissertations, Theses, and Masters Projects. Paper 1539623944.
<https://dx.doi.org/doi:10.21220/s2-r3zj-7990>

This Dissertation is brought to you for free and open access by the Theses, Dissertations, & Master Projects at W&M ScholarWorks. It has been accepted for inclusion in Dissertations, Theses, and Masters Projects by an authorized administrator of W&M ScholarWorks. For more information, please contact scholarworks@wm.edu.

INFORMATION TO USERS

This manuscript has been reproduced from the microfilm master. UMI films the text directly from the original or copy submitted. Thus, some thesis and dissertation copies are in typewriter face, while others may be from any type of computer printer.

The quality of this reproduction is dependent upon the quality of the copy submitted. Broken or indistinct print, colored or poor quality illustrations and photographs, print bleedthrough, substandard margins, and improper alignment can adversely affect reproduction.

In the unlikely event that the author did not send UMI a complete manuscript and there are missing pages, these will be noted. Also, if unauthorized copyright material had to be removed, a note will indicate the deletion.

Oversize materials (e.g., maps, drawings, charts) are reproduced by sectioning the original, beginning at the upper left-hand corner and continuing from left to right in equal sections with small overlaps. Each original is also photographed in one exposure and is included in reduced form at the back of the book.

Photographs included in the original manuscript have been reproduced xerographically in this copy. Higher quality 6" x 9" black and white photographic prints are available for any photographs or illustrations appearing in this copy for an additional charge. Contact UMI directly to order.

UMI[®]

Bell & Howell Information and Learning
300 North Zeeb Road, Ann Arbor, MI 48106-1346 USA
800-521-0600

GAMMA-RAY IMAGING DETECTOR FOR SMALL
ANIMAL RESEARCH

A Dissertation

Presented to the Faculty of the Department of Applied Science

The College of William and Mary in Virginia

In Partial Fulfillment

of the Requirements for the Degree of

Doctor of Philosophy

By

Andrew G. Weisenberger

August 1998

UMI Number: 9936910

UMI Microform 9936910
Copyright 1999, by UMI Company. All rights reserved.

This microform edition is protected against unauthorized
copying under Title 17, United States Code.

UMI
300 North Zeeb Road
Ann Arbor, MI 48103

APPROVAL SHEET

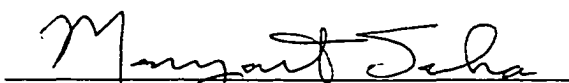
This dissertation is submitted in partial fulfillment of
the requirements for the degree of

Doctor of Philosophy.

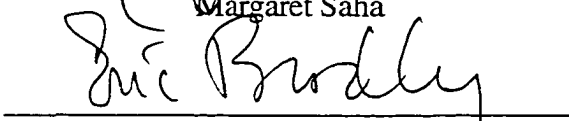


Andrew G. Weisenberger


Approved, August 1998




Margaret Saha



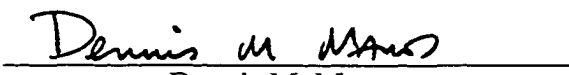
Eric Bradley
Department of Biology



Mark Hinders



Stan Majewski
Department of Physics



Dennis M. Manos

This work is dedicated to my wife,

Jill,

who is my best friend,

...forever.

CONTENTS

ACKNOWLEDGMENTS	VII
LIST OF TABLES	IX
LIST OF FIGURES.....	X
ABSTRACT.....	XII
CHAPTER 1. INTRODUCTION.....	2
1.1 RADIATION DETECTION APPLIED TO MOLECULAR BIOLOGY	2
1.2 A NOVEL DETECTOR SYSTEM.....	4
1.3 ORGANIZATION OF THIS THESIS	5
CHAPTER 2. NUCLEAR MEDICINE IMAGING IN ANIMAL RESEARCH.....	6
2.1 NUCLEAR MEDICINE IMAGING MODALITIES.....	6
2.1.1 <i>Functional Imaging</i>	7
2.1.2 <i>Gamma Camera</i>	8
2.1.2.1 Collimators.....	10
2.1.2.2 Scintillators and photomultiplier tubes.....	16
2.1.3 <i>SPECT Imaging</i>	17
2.1.4 <i>PET Imaging</i>	19
2.2 NUCLEAR MEDICINE DETECTOR DEVELOPMENT FOR ANIMAL IMAGING.....	21
2.2.1 <i>Pinhole Collimated Gamma Cameras</i>	24
2.2.2 <i>Parallel hole Collimated Gamma Cameras</i>	25
2.2.3 <i>Focused Collimator Tomograph</i>	26
2.2.4 <i>PET</i>	27
2.2.5 <i>Small Animal Imaging Discussion</i>	34
CHAPTER 3. DEVELOPMENT OF AN ¹²⁵I IMAGING DETECTOR SYSTEM	36
3.1 PROJECT OVERVIEW	37
3.1.1 <i>Existing In Vivo Methods</i>	38
3.1.2 <i>In Vivo Gene Studies</i>	38
3.1.2.1 Reporter Gene Detection	39
3.1.2.2 Gene Imaging via Antisense RNA.....	40
3.2 IODINE 125.....	42
3.2.1 <i>Properties of Iodine 125</i>	43
3.2.2 <i>Iodine 125 Production</i>	45
3.3 DETECTOR INSTRUMENTATION	45
3.3.1 <i>Position Sensitive Photomultiplier Tubes</i>	46
3.3.2 <i>Readout of Position Sensitive Photomultiplier Tubes</i>	48
3.3.3 <i>Position Determination</i>	49
3.3.4 <i>Data Acquisition System</i>	52
3.3.5 <i>Coincident Radiation Detection</i>	53
3.4 PROTOTYPE YAP BASED GAMMA-RAY IMAGING SYSTEM.....	55
3.4.1 <i>R2486 Position Sensitive Photomultiplier Tube Based Detector</i>	55
3.4.1.1 Preliminary Detector Imaging Tests	56
3.4.1.2 Detector Properties.....	58

3.4.2	<i>Detector Performance During Animal Laboratory Tests</i>	60
3.4.2.1	Animal Studies with ¹²⁵ I.....	60
3.4.2.2	Animal Studies with ¹²⁵ I-labeled Melatonin.....	63
3.4.3	<i>Discussion of the First Prototype Results</i>	67
3.5	GAMMA-RAY IMAGING SYSTEM BASED A ON CsI(Na) CRYSTAL ARRAY	67
3.5.1	<i>R3292 Position Sensitive Photomultiplier Tube Based Detector</i>	68
3.5.1.1	Scintillating Crystal Arrays	68
3.5.1.2	Hamamatsu R3292 Position Sensitive Photomultiplier Tube.....	70
3.5.2	<i>CsI(Na) Scintillating Crystal Array Performance and Mapping</i>	71
3.5.2.1	CsI(Na) Scintillating Crystal Array Performance.....	71
3.5.2.2	Crystal Array Mapping	73
3.5.3	<i>Detector Performance Imaging ¹²⁵I Labeled Melatonin in a Live Mouse</i>	75
3.5.4	<i>Discussion of the CsI(Na) Array Based Results</i>	78
3.6	GAMMA-RAY IMAGING SYSTEM BASED ON AN ARRAY WITH 1.0 MM X 1.0 MM ELEMENTS	78
3.6.1	<i>CsI(Na) Array with 1.0 mm x 1.0 mm Elements</i>	79
3.6.1.1	Raw Flood Image Using 662 keV Gamma-rays.....	79
3.6.1.2	Array Mapping.....	81
3.6.2	<i>High Resolution Copper Collimator</i>	84
3.6.2.1	Collimator Construction.....	84
3.6.2.2	Collimator Performance.....	85
3.6.3	<i>Phantom Imaging Detector Performance Tests</i>	86
3.6.3.1	Singles Mode Phantom Studies	86
3.6.3.2	Coincidence Mode Phantom Studies	90
3.7	<i>Imaging Iodine Uptake in a Mouse</i>	91
CHAPTER 4. IMAGING RECEPTOR BINDING IN THE MOUSE BRAIN		95
4.1.	<i>Static Biodistribution of RTI-55</i>	96
4.2.	<i>Dynamic Dependence of the Biodistribution RTI-55</i>	99
4.3	<i>Apparent Brain Accumilation of RTI-55</i>	111
4.4	<i>Discussion of RTI-55 Results</i>	113
CHAPTER 5. DISCUSSION AND FUTURE DIRECTIONS		114
5.1	MOLECULAR BIOLOGY ASSAYS	114
5.2	CONCLUSION	118
APPENDIX A. MOLECULAR BIOLOGY BACKGROUND		119
A.1	MOLECULAR BIOLOGY THEORY: THE "CENTRAL DOGMA"	119
A.1.1	<i>DNA</i>	120
A.1.2	<i>RNA</i>	120
A.1.3	<i>Protein Formation</i>	122
A.1.4	<i>Post Translational Modification</i>	124
A.2	MOLECULAR BIOLOGY TECHNIQUES	125
A.2.1	<i>Making a Recombinant Molecule</i>	125
A.2.1.1	Restriction Enzymes and Ligases	125
A.2.1.2	Vectors	126
A.2.2	<i>cDNA Libraries and Genomic Libraries</i>	128
A.2.3	<i>Analyzing Transcription</i>	129
A.2.3.1	Northern Blotting.....	130
A.2.3.2	RNase Protection Assays	131
A.2.3.3	In Situ Hybridization	131
A.2.3.3	Analysis of Promoter Activity.....	132
A.2.4	<i>Analyzing Proteins</i>	133
A.2.4.1	Western Blotting.....	134
A.2.4.2	Immunocytochemistry	134

A.2.4.3 Ligand Binding	134
A.2.5 <i>Analyzing Gene Function</i>	135
A.2.5.1 Homologous Recombination	135
A.2.5.2 Transgenics.....	136
A.2.5.3 Reporter Genes.....	136
A.2.5.4 <i>In Vivo</i> Gene Imaging.....	138
A.3 MOLECULAR BIOLOGY CONCLUSION	138
APPENDIX B. RADIATION DETECTOR PRINCIPLES.....	140
B.1 RADIOACTIVE DECAY	140
<i>B.1.1 Radiation Dose and Exposure</i>	143
B.2 DECAY PROCESSES	146
<i>B.2.1 Emission of Alpha Particles</i>	147
<i>B.2.2 Ejection of Energetic Electrons</i>	147
<i>B.2.3 Ejection of High Energy Photons</i>	150
B.3 RADIATION DETECTION.....	152
<i>B.3.1 Beta Particles</i>	152
<i>B.3.2 Gamma-Rays and X-Rays</i>	153
<i>B.3.3 Scintillators</i>	158
<i>B.3.4 Photomultiplier Tubes</i>	164
<i>B.3.5 Final Detector Assembly</i>	167
BIBLIOGRAPHY	168
VITA	178

Acknowledgments

Many people have helped in the completion of this work. I would like to express great appreciation to the members of my committee: Dr. Eric Bradley, Dr. Mark Hinders, Dr. Stan Majewski, Dr. Dennis Manos, and Dr. Margaret Saha.

I thank my thesis advisor, Dr. Margaret Saha of Biology for opening the fascinating world of molecular biology and neurobiology research to me, for helping me design and complete my project, and for helping secure funding for much of it. I thank her for the many hours she spent sharing her enthusiasm for science, making it possible for me to do molecular biology research and for her encouragement.. I thank Dr. Dennis Manos for encouraging me in the realization of a project which spans several fields. His support, guidance, and participation in my project were vital to the reaching of my goal. I wish to thank Dr. Stan Majewski of Physics for sharing with me his vast knowledge of particle physics detection, for the many hours he spent helping me with my detector development, and for making it possible for me to be involved in applying nuclear physics detector research techniques to problems in various fields. I thank greatly Dr. Eric Bradley of Biology for teaching me laboratory techniques needed to do research using live animals, and for working closely with me during the animal studies. Because of his many discussions with me, his assistance in handling the animals in laboratory studies, and for showing me how to interpret and describe biological results, the completion my project was possible. I also want to thank Dr. Mark Hinders for his encouragement, and for the valuable discussions I had with him.

I also thank Kathee Card in Applied Science for all her assistance with university requirements. Her encouragement and helpfulness was greatly appreciated. I want to thank the graduate students in the Department of Applied Science for making me feel part of a special group. I also thank the students and staff in the Department of Biology for all of their help and encouragement.

I thank all the members of the Thomas Jefferson National Accelerator Laboratory Detector Group. I thank Brian Kross for fabricating much of the mechanics of the gantry and for constructing several phantoms used in this study. I also thank Randy Wojcik for his assistance with many electronic requirements of the project. Thanks to Dr. Carl Zorn for his helpful discussions, suggestions, and his thorough reading of the detector physics part of this thesis. And I also thank Dr. Howard Fenker for the discussions we have had regarding some computational aspects of my work. I also thank Tom Carstens of Jefferson Lab for the design and assembly of the amplifier boards used in this detector.

I thank Dr. Simon Cherry of the UCLA Crump Institute for the many valuable discussions regarding the construction of this detector system and for his many helpful suggestions. I would like to express my appreciation to Dr. Paul Heideman of the Biology Department of the College of William and Mary for his assistance with the melatonin study. I also thank Dr. Kwamena Baidoo of the Department of Environmental Health Sciences at Johns Hopkins University for suggesting I use RTI-55 in my research.

I also thank Earl Hergert, Seiji Suzuki, and Yuji Yoshizawa of Hamamatsu for use of the position sensitive photomultiplier tube. I gratefully acknowledge the funding assistance from the Southeastern Universities Research Association (SURA) which operates the Thomas Jefferson National Accelerator Facility for the United States Department of Energy under contract DE-AC05-84ER40150. In addition I acknowledge funding received for part of this project obtained through NSF grant # IBN9602865.

I also want to thank my parents Andy and Maura Weisenberger for their encouragement and faith in me. They helped instill in me a thirst for understanding. I also want to thank all my family and friends who have been offering me encouragement.

Most importantly, I want to thank “my girls”: my wife Jill and our two daughters Erin and Emily. Their love, understanding, and patience made it possible for me to complete this task. I cannot express enough my gratitude to my wife for the many times she had to manage our lives while I was busy with my work.

List of Tables

Table 2.1: Table of positron emitting isotopes	22
Table 2.2: Table of gamma-ray emitting isotopes.....	23
Table B.1. Various properties of crystal scintillators.....	163

List of Figures

Figure 2.1:	Schematic diagram of the modern clinical gamma camera.....	10
Figure 2.2:	Diagram of the three basic gamma camera collimator designs	11
Figure 2.3:	Basic design of a typical clinical pinhole collimator.....	12
Figure 2.4:	Magnified picture of a parallel hole collimator	15
Figure 2.5:	Diagram showing a side and front view of a clinical SPECT scanner	18
Figure 2.6:	Diagram showing a side and front view of a clinical PET scanner.....	20
Figure 3.1:	Antisense RNA probe linked to ^{125}I	41
Figure 3.2:	Decay scheme for ^{125}I to a nuclear excited state of tellurium 125.....	44
Figure 3.3:	Schematic of the operation of a position sensitive photomultiplier tube	47
Figure 3.4:	Schematic showing the basics of the charge division readout	48
Figure 3.5:	Four images for four selected values of the truncation factor (F)	51
Figure 3.6:	Block diagram of the data acquisition electronics	54
Figure 3.7:	Detector arrangement for coincident detection of x-ray and gamma-ray.....	56
Figure 3.8:	Raw image obtained in singles mode of an ^{125}I calibration source	57
Figure 3.9:	Raw image of the same ^{125}I calibration source coincidence mode.....	58
Figure 3.10:	^{125}I pulse height (energy) spectrum.....	59
Figure 3.11:	Raw image obtained using coincidence data acquisition mode.....	61
Figure 3.12:	Image data scaled and then overlaid onto a photograph of the mouse.....	62
Figure 3.13:	Raw image obtained in coincidence mode of ^{125}I in the mouse	63
Figure 3.14:	Image of ^{125}I labeled melatonin distribution in mouse.....	64
Figure 3.15:	Data from Figure 14 on top of a photograph of a mouse	65
Figure 3.16:	Time change of melatonin in the head compared to the chest	66
Figure 3.17:	Cross sectional view of R3292 coupled to the CsI(Na) crystal array.	70
Figure 3.18:	The full raw flood image of the crystal array.....	72
Figure 3.19:	Pulse height spectrum for the image taken in coincidence mode.....	73
Figure 3.20:	Map of crystal regions	74
Figure 3.21:	Raw image obtained using the CsI(Na) array	76
Figure 3.22:	Corrected image from data in Figure 3.22.....	77
Figure 3.23:	The full flood raw image of the 1 mm crystal array	80
Figure 3.24:	Enlargement of a 3x3 cm ² area of the flood image of 1 mm crystal array....	81
Figure 3.25:	Iodine 125 pulse height (energy) spectra for five adjacent crystals.....	82
Figure 3.26:	Two dimensional representation of pulse height spectra peak value.....	83
Figure 3.27:	A precision stack lamination copper-beryllium collimator	85
Figure 3.28:	Image of a cross pattern made by imaging two plastic tubes filled ^{125}I	87
Figure 3.29:	Image obtained of a loop constructed out of plastic tube filled with ^{125}I	88
Figure 3.30:	Image of a ^{125}I filled grid phantom	90
Figure 3.31:	Two corrected images obtained with a three minute acquisition time.....	91
Figure 3.32:	Images obtained of iodine distribution in 17.5 gm male mouse.....	93
Figure 4.1:	Image of the biodistribution of RTI-55 in a 25 gm male CD-1 mouse.....	97
Figure 4.2:	Side-view image of the biodistribution of RTI-55 in the same mouse.....	98
Figure 4.3:	Image of the accumulated biodistribution of RTI-55 in the CD-1 mouse....	100
Figure 4.4:	A series of images of the distribution of RTI in a mouse.....	101
Figure 4.5:	Two images of the biodistribution of RTI with regions of interest.....	105
Figure 4.6:	Plot of the change over time of the total counts and center head region	106
Figure 4.7:	Plot of the change over time of the total counts and the lower head region. .	107
Figure 4.8:	Graph total counts with the counts in the region of the gut.....	108
Figure 4.9:	Graph of counts in lower head region plotted with Johns Hopkins data	109

Figure 4.10: Graph of counts of two head regions and total with Johns Hopkins data . . .	110
Figure 4.11: Graph over time of counts in head region divided by total image counts . . .	113
Figure 4.12: Images overlaid onto photographs of the experimental mouse	112
Figure 5.1: A schematic of the gantry to be used to obtain SPECT images	116
Figure 5.2: A photograph of the gantry to be used to obtain SPECT images	117
Figure A.1. The process of transcription from DNA to mRNA	121
Figure A.2. Translation of mRNA into a polypeptide chain by ribosomes.	122
Figure A.3: The sequence of transcription from DNA to mRNA to protein.	123
Figure A.4: Restriction site in a DNA molecule for the restriction enzyme Eco RI.	126
Figure A.5: Example of two vectors	128
Figure A.6: Basic structure of a eukaryotic gene which codes for a protein	133
Figure A.7: Schematic of reporter gene technique	137
Figure B.1: Illustration of photoelectric absorption	155
Figure B.2: Illustration of the Compton scattering	156
Figure B.3: General shape of a spectrum illustrating of combined absorption	157
Figure B.4: Energy level diagram of the π -electron structure of an organic molecule	160
Figure B.5: Illustration of the energy bands in a scintillation crystal	162
Figure B.6: Diagram illustrating the two types of photomultiplier tubes	165

Abstract

A novel radiation imaging technology for *in vivo* molecular imaging in small mammals is described. The goal of this project is to develop a new type of imaging detector system suitable for real-time *in vivo* probe imaging studies in small animals. This technology takes advantage of the gamma-ray and x-ray emission properties of the radioisotope iodine 125 (^{125}I) which is employed as a label for molecular tracers. The radioisotope ^{125}I is a gamma-ray emitting radioisotope that can be commercially obtained already attached to biologically relevant molecules to be used as tracers for biomedical and molecular biology research.

The isotope ^{125}I decays via electron capture consequently emitting a 35 keV gamma-ray followed by the near coincident emission of several 27-32 keV $\text{K}\alpha$ and $\text{K}\beta$ shell x-rays. Because of these phenomena, a coincidence condition can be set to detect ^{125}I thus enabling the reduction of any background radiation that could contaminate the image. The detector system is based on an array of CsI(Na) crystal scintillators coupled to a 125 mm diameter position sensitive photomultiplier tube. An additional standard 125 mm diameter photomultiplier tube coupled to a NaI(Tl) scintillator acts as the coincident detector. To achieve high resolution images the detector system utilizes a custom-built copper laminate high resolution collimator. The ^{125}I detector system can achieve a spatial resolution of less than 2 mm FWHM for an object at a distance of 1.5 cm from the collimator. The measured total detector sensitivity while using the copper collimator was 68 cpm/ μCi . The electronic readout and analog to digital electronics make use of modular electronics that are commercially available. The data acquisition and user interface is performed by a Power PC Apple Macintosh desktop computer.

Results of *in vivo* mouse imaging studies of the biodistribution of iodine, melatonin, and a neurotransmitter analog (RTI-55) are presented. Many studies in molecular biology require an analysis of the expression and regulation of a gene at different stages of an organism's development or under different physiological conditions. This detector system makes it possible for laboratories without access to standard nuclear medicine radiopharmaceuticals to perform *in vivo* imaging research on small mammals using a whole range of ^{125}I labeled markers that are obtainable from commercial sources.

GAMMA-RAY IMAGING DETECTOR FOR SMALL
ANIMAL RESEARCH

Chapter 1

Introduction

1.1 Radiation Detection Applied to Molecular Biology

Currently molecular biology techniques are contributing to the understanding of the mechanisms of gene expression and the myriad consequences of that expression. It is the instructions encoded in genes, defined by sequences of DNA molecules, that direct the cell to grow, differentiate, and divide. The mouse is one of the most frequently used mammals for molecular biological research studies on gene expression. The primary methods available to follow and study gene expression currently employ RNase protection assays, Northern blots, *in situ* hybridization, and immunocytochemistry. These methods are typically used to study gene expression at single moments in time for an individual mouse. One must sacrifice the mouse to make a measurement, essentially taking a snapshot of the state of expression of the gene of interest. An ability to detect the distribution of gene expression and receptor binding *in vivo* for a single mouse is needed. To be useful, the *in vivo* gene imaging technique should be real-time, quantitative, and able to follow the organism over hours to weeks.

The goal of the project described here is to develop a new type of imaging detector system suitable for real-time *in vivo* probe imaging studies in small animals. In order to be

practical, the detector system would have to make use of gene detection materials readily available to most molecular biology researchers. Much of molecular biology research utilizes specially constructed tracer molecules that will bind to specific target molecules to enable the detection and study of specific genes. Tracer molecules called probes can be constructed out of sequences of nucleic acid that bind to specific target RNA molecules. Other tracer molecules called ligands can be designed to bind to specific target proteins. The tracers, in addition to having the ability to bind to the target, must also have a property that allows them to be detected. To make detection possible, tracers are labeled with radioactive isotopes. Commercially produced tracers are labeled with radioactive isotopes of phosphorus (^{32}P), carbon (^{12}C), sulfur (^{35}S), hydrogen (^3H), or iodine (^{125}I and ^{131}I). The main application of these tracers is in assays involving paper thin slices of tissue samples that are placed in contact with a specially designed photographic film; this technique of detection is called autoradiography. Film exposure times of hours to months may be needed to obtain an image of the distribution of the radioisotope in the sample.

Only ^{125}I and ^{131}I emit both x-rays and gamma-rays suitable for *in vivo* studies involving small animals. This is because the other isotopes emit only electrons (beta particles) that have a range of less than 1 mm in tissue and therefore get absorbed by the tissue before emerging from the body of the animal being studied. The isotope ^{125}I compared to ^{131}I is more readily available as a label for tracers for molecular biology research and thus more suitable for *in vivo* small animal imaging. In addition, the high energy gamma-rays (364 keV and 637 keV) ^{131}I emits, and its short half-life (8 days) makes it less suitable for small animal imaging. It is difficult to construct high resolution small animal imaging detectors for the high energy gamma-rays emitted by ^{131}I . The long half-life (60 days) and lower energy gamma-rays (~35 keV) are well suited for small animal imaging detectors. The biotechnology company Dupont NEN, Inc. has over 150 biochemical tracers that are labeled with ^{125}I [1].

1.2 A Novel Detector System

This thesis describes the development and testing of a novel radiation imaging detector system that was designed specifically to detect and generate high resolution images of the distribution ^{125}I in small animals. Radiation imaging techniques similar to those employed with a nuclear medicine gamma camera have been developed to do high spatial resolution, real-time planar imaging of molecules in live small animals. The radiation imaging system makes use of new types of radiation detection materials and methods such that two ^{125}I point sources, separated by less than 2 mm, can be resolved. Such resolutions of < 2 mm full width half maximum (FWHM) for the imaging of ^{125}I is currently not possible with existing clinical nuclear medicine imaging detectors. The detector developed here is the only system capable of allowing a researcher to test a whole series of biological tracers in small animals such as mice *in vivo*. This detector system provides the ability to follow biological processes on a molecular level that are of considerable general importance for both theoretical and therapeutic reasons.

As will be pointed out in Chapter Two, within the last five years there has been work in the area of detector development for designing animal imaging systems appropriate for nuclear medicine type research that utilizes animals. Attempts are being made to scale down standard nuclear medicine imaging systems to facilitate *in vivo* nuclear medicine research using live animals. The detector system developed here was designed with the goal of providing the best detector system to image ^{125}I in small animals for the primary purpose of molecular biology research. Though the low energy gamma- and x-rays (28-35 keV) and long half-life (60 days) are not suitable for imaging in humans, any tracers labeled with ^{125}I can also be labeled with ^{123}I which emits gamma-rays at higher energy (159 keV). Moreover, ^{123}I has a much shorter half-life (13.3 hours) which together with its energy makes it more suitable for human imaging applications [2].

1.3 Organization of this Thesis

Since the development of the detector system involves both detector physics and molecular biology, two concise appendices present background material which will provide information for the topics covered in the chapters. Appendix A outlines basic molecular biology as well as research techniques presently used to study genes. Appendix B provides background material regarding elementary concepts of detector physics used in particle physics and nuclear medicine. Basic detector topics, such as scintillators and photomultiplier tubes, are covered as well.

The first part of Chapter Two describes nuclear medicine imaging detector techniques that are pertinent to biomedical research involving small animals. The last part of Chapter Two provides a review of the state of the art of the detector development utilizing nuclear medicine techniques in animal research and will describe the advantages of the detector system developed for this dissertation. Chapter Three describes the different stages of design and testing of the radiation imaging detector that was developed. Presentations of part of this research have been made at various conferences and in different journals where the discipline was medical imaging, detector development, or developmental biology. Chapter Four presents initial results from a mouse imaging study involving the time dependence of accumulation of a brain specific molecular probe, RTI-55. Chapter Five reviews the present stage of the project and discusses the future directions for continuation of this project.

Chapter 2

Nuclear Medicine Imaging in Animal Research

This chapter describes the basic concepts involved in nuclear medicine imaging detector systems that are pertinent to biomedical research involving small animals. The last section provides a summary of the state of the art of other detector development research utilizing nuclear medicine techniques in animal research. The detector system which is the central topic of this dissertation will be compared to these other imaging systems.

2.1 Nuclear Medicine Imaging Modalities

Nuclear medicine imaging diagnostic procedures for patients involves the imaging of the distribution in the patient's body of injected biochemical compounds that have been labeled with a radioactive nuclide. These tracer compounds, whose biodistribution is sought, are referred to as radiotracers, or radiopharmaceuticals [3]. Imaging detectors may be used to image the distribution of the radiopharmaceutical after the tracer has been injected into a patient. The temporal and spatial manner in which a radiopharmaceutical compound is distributed in the tissue of the patient is dependent on the metabolism and biological function of that compound. Thus, by imaging the biodistribution of the

radiopharmaceutical, information about the tissue uptake rate and distribution is obtained. For example, the radioisotope fluorine-18 is employed to label glucose (^{18}F -fluoro-2-deoxyglucose), so that when injected into a patient it accumulates in metabolically active tissue just as glucose would [4].

Cancer cells lock into an uncontrolled growth phase and replicate at an accelerated rate. It is believed because of this rapid growth and tumor cell specific enzyme abnormalities (isoenzymes of hexokinase), cancerous tissue has a high glucose requirement compared to normal tissue and enhanced glucose uptake can be quantified by using a nuclear medicine imaging detector[4].

This imaging modality is quite different from x-ray imaging, in which externally produced x-rays are directed through the patient to generate a structural image. In x-ray imaging a detector is used to record the tissue attenuation of the x-rays which is a function of tissue density.

2.1.1 Functional Imaging

The measure of the rate and distribution pattern of an injected radiotracer facilitates the diagnosis of a disease through the imaging of some anomalous bioactivity of the injected radiopharmaceutical. In addition to glucose, other compounds such as amino acids, nucleic acids, and peptides can be labeled with radioactive isotopes. The imaging of the biodistribution of these compounds provides information on the development and growth of body tissues under different conditions, such as that brought on by injury or drug therapy. For functional imaging, two different classes of radioactive nuclides are used, those whose radioactive decay results in the emission of single gamma-rays and x-rays, and those whose decay results in the emission of a positron (the anti-particle of an electron).

The first class of emitters are used to obtain planar nuclear medicine images (also known as scintigraphy) and single-photon emission computed tomography (SPECT) images [5]. The most common radioactive isotope used for radiopharmaceuticals as a label for planar imaging and SPECT imaging is technetium-99m (^{99m}Tc , 140 keV gamma-ray, 6 hour half-life), other elements such as radioisotopes of thallium (^{201}Tl , 68 to 80 keV x-rays, 167 and 135 keV gamma-rays, 73 hour half-life), gallium (^{67}Ga , 93 and 184 keV gamma-rays, 78 hour half-life), and xenon (^{133}Xe , 31 keV x-ray and 81 keV gamma-ray, 5.3 day half-life) are also used. The second class of emitters, positron emitting isotopes, are used to generate positron emission tomography (PET) images [6]. The most common radionuclide used as a label for PET radiopharmaceuticals is fluorine-18 (^{18}F , 110 minute half-life). Other positron-emitting isotopes such as radioisotopes of oxygen (^{15}O , 2 minute half-life) and carbon (^{11}C , 20 minute half-life) are also used.

In planar imaging, the three dimensional distribution of the radioactive tracer in the patient is seen as a two dimensional image of the superposition of the tracer at different depths along the line of sight of the gamma-ray camera, also referred to as a gamma camera, which was developed in the 1950's by Hal Anger [7]. With SPECT imaging, computer algorithms based on the Radon transform reconstruct the volume distribution of the radiotracer by processing several projection images taken at different angles around the patient. The basic detector element for SPECT is also the gamma camera.

2.1.2 Gamma Camera

For planar imaging and tomographic (i.e. SPECT) imaging the basic detector element is the gamma camera, a typical clinical gamma camera is 50 cm in diameter. For certain medical imaging diagnostic procedures, such as cardiac and thyroid studies, a single gamma camera is employed to obtain planar images. A typical clinical gamma camera is made of an array of photomultiplier tubes that have their entrance windows coupled by a

light guide to a large plate of a crystal scintillator material. The gamma-ray emitted by the isotope interacts in the crystal scintillator resulting in the emission of a scintillation light pulse that is then detected by the bank of photomultiplier tubes. The location of the interaction point is determined from the relative intensity of the light pulse signal simultaneously detected by all of the photomultiplier tubes. A high density material (usually lead, but sometimes tungsten) is used to make a collimator which restricts the direction of gamma-rays so that an image can be obtained. High spatial resolution images are obtained by choosing high resolution collimators and photon detectors that have a high intrinsic position resolving capability. However, the tradeoff of high resolution is low sensitivity, since higher resolution requires smaller openings in the collimator thus permitting fewer gamma-rays to reach the scintillator detector. Sensitivity is the ratio of counts detected per unit time divided by the activity of the radioactive source. Sensitivity is usually quoted for a collimator-detector system in terms of counts per second (cps) / mCi [8].

The central components of a gamma camera are a matrix of standard photomultiplier tubes, a disk of crystal scintillator (typically NaI) and a lead collimator. This design was first reported by Anger [7]. The mathematics in the following section were used to design a special copper collimator which is described in Chapter Three. Figure 2.1 shows a schematic of the major components of a modern clinical gamma camera.

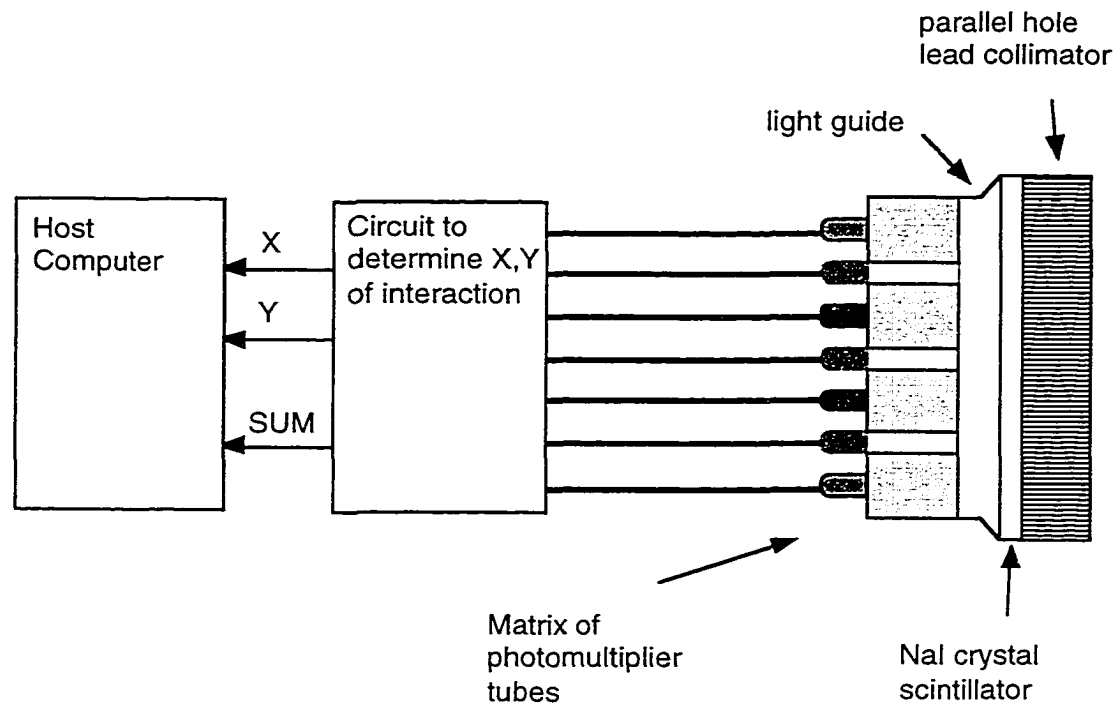


Figure 2.1: Schematic diagram of the major components of the modern clinical gamma camera.

The NaI(Tl) crystal scintillator is attached to the matrix of photomultiplier tubes via a light guide whose purpose is to transmit the scintillation light to the array of photomultiplier tubes. A scintillation light pulse is generated as a result of the total or partial absorption of ionizing radiation in the scintillation crystal. In nuclear medicine, the ionizing radiation is either gamma-rays or x-rays. This scintillation light produced by the gamma-ray or x-ray interaction transmits out of the crystal, through the light guide, to the matrix of photomultiplier tubes.

2.1.2.1 Collimators

The purpose of the lead collimator is to act as a means to constrain along a single direction the detection of the gamma-rays. Since gamma-ray photons cannot be focused with lenses one achieves "focusing" by using a bore hole made into lead or some other high Z material. A collimator can be merely a single hole to construct a "pinhole camera" or can

be made from a series of holes in lead to make three types of collimators: a parallel hole collimator, a converging collimator, or a diverging collimator. Figure 2.2 illustrates the three types of collimators.

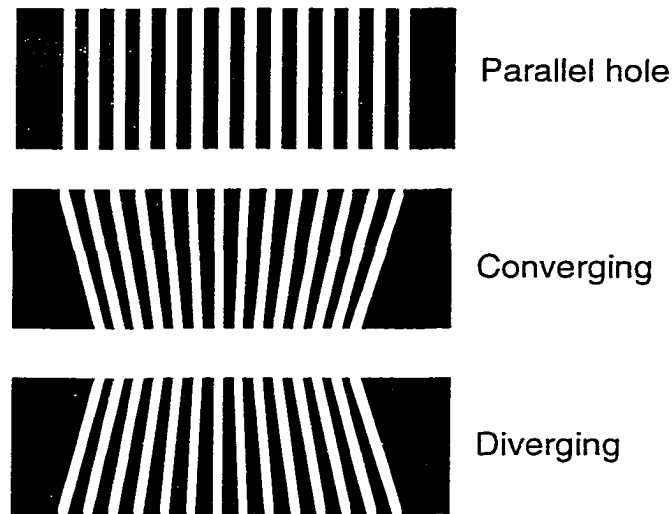


Figure 2.2: Diagram of the three basic gamma camera collimator designs.

The material of the collimator (lead, tungsten, copper etc.), the diameter of the bore hole, the thickness of the septa, and the thickness of the collimator are the collimator parameters that determine the sensitivity and spatial resolution of the gamma camera. The sensitivity as defined here, refers to the measure of acceptance of the gamma-rays being emitted by the radioactive source that actually hit the scintillator. Sometimes sensitivity is expressed in percentage or fractional terms from purely geometric means as in geometric acceptance in addition in terms of counts/sec/mCi. The latter case also takes into account the total sensitivity of the collimator-scintillator-photomultiplier combination and is obtained empirically. For instance, the typical sensitivity of a clinical gamma camera equipped with a high resolution collimator is less than 5000 counts/sec/mCi [9].

A pinhole gamma camera operates under the same principle as the optical pinhole camera. This was the collimator first employed by Anger and is still used to image a small

object by using the magnifying properties of a pinhole camera. The pinhole collimator is usually used in nuclear medicine to image small organs and is used in laboratory research involving imaging of animals.

The major limitation of the pinhole camera is its poor sensitivity and the dependence of sensitivity on the angle of the object from the normal direction. Figure 2.3 shows a diagram illustrating the basic design of a pinhole collimator.

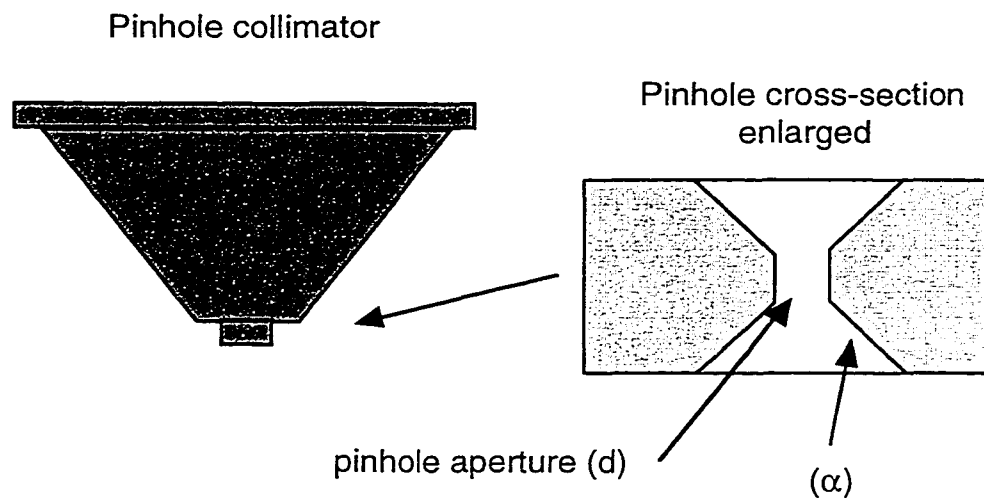


Figure 2.3: Basic design of a typical clinical pinhole collimator and a magnified view of a cross-section the pinhole aperture.

The resolution (R_g) and sensitivity are described by the following equations using the notation used by Anger [10]:

$$R_g = (a + b)d_e/a \quad (2.1)$$

where:

R_g is the collimator resolution,

a is the distance from the pinhole aperture to the front of the scintillator,

b is the distance from the object to the pinhole aperture, and

d_e is the effective size of the pinhole opening expressed by:

$$d_e = [d(d + 2/\mu \tan(\alpha/2))]^{1/2} \quad (2.2)$$

where:

d is the pinhole opening diameter,

μ is the total linear attenuation coefficient of the collimator material at the energy of the gamma-rays, and

α is the taper angle of the pinhole.

The total system resolution (R_s) is:

$$R_s = [R_g^2 + ((b/a)R_i)^2]^{1/2} \quad (2.3)$$

where:

R_i is the intrinsic resolution of the gamma camera.

The sensitivity is dependent upon the distance between the aperture and the object. The geometric efficiency is the fraction of isotropically emitted gamma-rays which are properly collimated. The on-axis geometric efficiency (g) for the pinhole collimator is:

$$g = d_c^2/16b^2 \quad (2.4)$$

This geometric efficiency decreases in the radial direction with $\sin^3(\theta)$ where θ is the off-axis angle. Often the main body of the pinhole collimator is constructed out of lead and the actual pinhole is made out of tungsten to reduce edge penetration of the gamma-rays.

Pinhole collimators on standard gamma cameras have been employed to perform high resolution imaging [11, 12]. By taking advantage of the magnification effect, one can achieve high resolution and good sensitivity by bringing the object to be imaged close to the pinhole. However, in order to image the full field of view it might be necessary to move the object farther from the pinhole, greatly reducing the sensitivity. For instance, to obtain planar images of a small tissue with a system resolution of 1.5 mm and a field of view 7 cm

a 0.6 mm diameter pinhole is required. The pinhole would need to be placed 6 cm in front of the scintillator and the tissue would need to be placed at a distance of 5 cm from the collimator. In this geometry the on-axis and 60° off-axis geometric acceptances are 7×10^{-6} and 3.0×10^{-6} respectively. The geometric acceptances improve to 4×10^{-5} and 2×10^{-5} by bringing the tissue 3 cm from the pinhole collimator for a reduced total field of view of 4 cm.

The most frequently used collimator is the parallel hole collimator because it offers higher sensitivity than the pinhole. The sensitivity is not dependent on distance between the object and aperture and is only a function of aperture opening, the septa thickness, and bore length [13]. The resolution and geometric efficiency are expressed by the following equations taken from Anger [14] and Keller[15]:

$$R_c = d(a_e + b + c)/a_e \quad (2.5)$$

$$a_e = a - 2/\mu \quad (2.6)$$

where:

R_c is the collimator resolution,

d is the size of the openings,

a is the core length (collimator thickness),

a_e is the effective core length,

μ is the total linear attenuation coefficient of the collimator material at the energy of the gamma-rays,

b is distance between the source to be imaged and the collimator face, and

c is the distance between the back of the collimator and the front of the scintillator.

The combined system resolution, R_s , can be described by the following equation:

$$R_s = (R_c^2 + R_i^2)^{1/2} \quad (2.7)$$

where:

R_i is the intrinsic resolution of the gamma camera.

One can see from the above equations that the realized resolution varies with distance to the object to be image. Closer objects are imaged at a higher resolution than farther ones. The geometric efficiency can be described by the following equation:

$$g = k^2(d^2/(a_e(d + s)))^2 \quad (2.8)$$

where:

k is an aperture shape dependent factor; it is 0.263 for hexagonal openings and 0.282 for square openings, and

s is distance between each opening (the septa thickness).

Parallel hole collimators for medical imaging are made either by gluing folded sheets of lead together in a hexagonal pattern (Figure 2.4) or are made by lead molds.

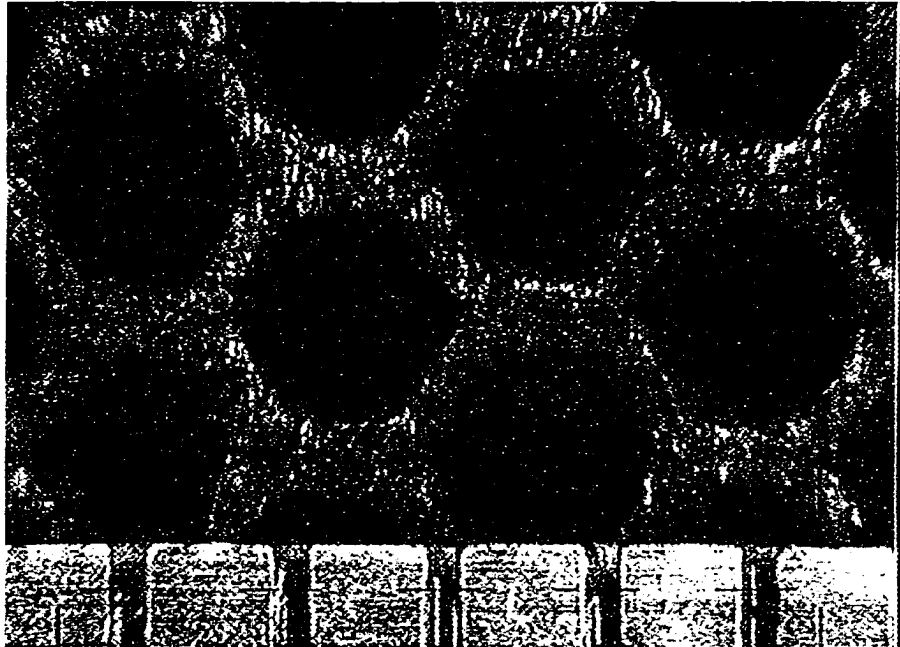


Figure 2.4: Magnified picture illustrating the hexagonal pattern hole structure of a parallel hole collimator made of folded sheets of lead which are glued together. The marks of the scale at the bottom of the picture are 1 mm apart.

Diverging collimators (see Figure 2.2) are used to image a small organ onto the detector surface to achieve higher position resolution, and converging collimators are used to image a large organ onto a smaller area detector surface. The main drawbacks of both designs are reduced sensitivity and image distortion, especially for thicker objects.

2.1.2.2 Scintillators and photomultiplier tubes

The crystal scintillator usually employed in a clinical gamma camera is thallium activated NaI which is an inorganic halide crystal. The high light output and good energy resolution of this scintillator make it an ideal scintillator for medical imaging applications. The wavelength of its scintillation light is well-matched to the wavelength sensitivity of a typical photomultiplier tube. The thickness of the scintillator is chosen to be sufficiently thick to provide maximum sensitivity to the incident gamma-ray photon but not too thick as to degrade position resolution caused by depth of interaction effects such as the differences in the geometry of light spread on the photodetector surface which impacts energy and spatial resolutions. The scintillation photons can be produced anywhere along the path length of the penetrating gamma-rays as a result of scintillator excitation. Scintillators are described in detail in Appendix B.

In a standard gamma camera typically, 37 or more, two inch diameter photomultiplier tubes are arranged in a matrix pattern and attached to the scintillator either via index of refraction matching optical grease alone or with a light guide (see Figure 2.2) [16]. The light pulse from the scintillator following the gamma-ray interaction is detected by the photomultiplier tubes resulting in an electrical output signal which is proportional to the amount of light detected in each photomultiplier tube. The output electrical signals, connected to a charge-division circuit, are used to determine the energy and location of the gamma-ray interaction point. For every gamma-ray event the output of the charge division circuit provides three analog signals, two signals representing the orthogonal coordinates of

the location of the origin of the light pulse and one signal representing the sum of all the photomultiplier tube signals. These signals are then digitized and stored in a computer for image reconstruction.

Since the intensity of the light pulse emitted by the scintillator is proportional to the energy of the incident ionizing radiation (e.g., x-rays or gamma-rays) the energy spectrum of the incident ionizing radiation can be obtained from a pulse height spectrum of the photomultiplier output pulses [17]. The sum signal is used to construct a pulse height spectrum which is the energy spectrum of the radiation striking the scintillator. This energy spectrum is then used to set data acquisition trigger thresholds, based on the energy acceptance window chosen, on the image generation. By placing conditions based on the sum signal, scattered gamma-rays not originating from the direction of the actual radiopharmaceutical uptake sites are excluded from the image. The scattered, thus lower energy, gamma-rays are the result of the primary gamma-ray Compton scattering in the patient, the collimator, or the scintillator. These processes lower the gamma-ray energy. A pulse height analysis is used to limit the processing of photon events to reduce the effect of scattered, low energy gamma-rays.

2.1.3 SPECT Imaging

As mentioned before, the gamma camera is the primary detector used in SPECT images. SPECT is used when tomography is required to obtain three dimensional tumor localization, such as in brain and internal organ cancer diagnostics. A SPECT image is obtained with a single gamma camera or with multiple gamma cameras to get several required views of the object to be imaged. After obtaining a sufficient number of views (60-100) a chosen slice through the patient is reconstructed via a computer [18].

A typical clinical SPECT system involves a gantry with three detector heads. An example of this type of detector configuration is shown in Figure 2.5. The patient is

positioned lying flat and perpendicular to the plane formed by the gantry which contains the gamma camera detector heads. Tomographic slices of the patient are obtained by scanning the patient horizontally through the gantry and acquiring multiple projections by rotating the gamma camera around the patient. The best resolution obtained so far for a clinical three head SPECT scanner while imaging a point sources is 7.5 mm full-width at half maximum in the center of the field of view.

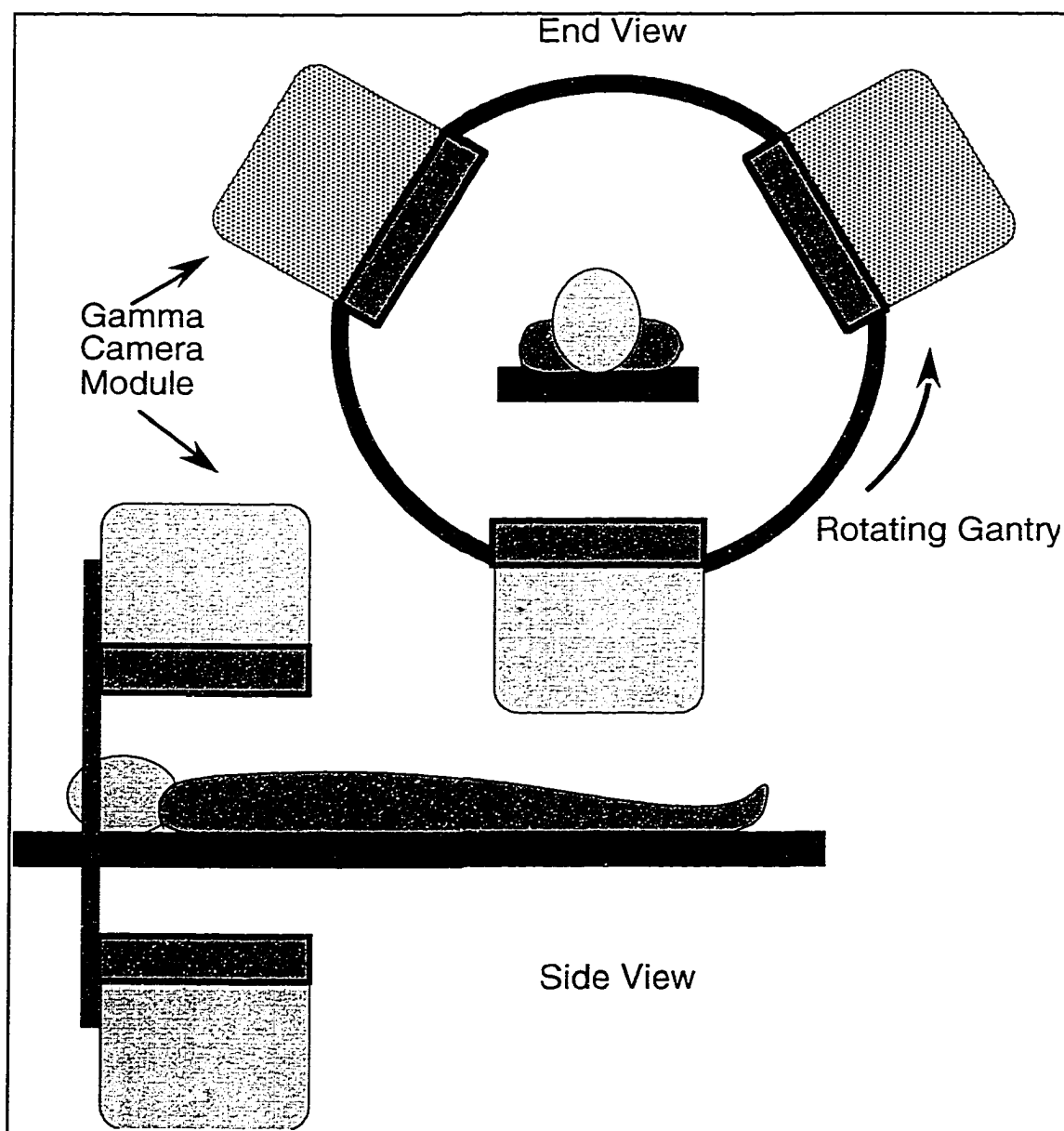


Figure 2.5: Diagram showing a side and front view of a clinical SPECT scanner based on a rotating ring of gamma camera detector modules which surround the patient.

2.1.4 PET Imaging

SPECT is similar to Positron Emission Tomography (PET) which uses positron emitting radiopharmaceuticals. With PET three dimension information may also be obtained of the biodistribution of the radiopharmaceutical. PET has advantages over SPECT since no collimator is needed, thus sensitivity is high, and spurious events in the detector that have no origin in the radiopharmaceuticals are rejected. In PET, the radioisotope decays by a physical process called positron emission (also called β^+ emission). The positron that is emitted in the nuclear decay is an example of a class of particles known as anti-matter. The positron is the anti-particle of an electron, it has the same mass of an electron however it has the opposite charge. A property of anti-matter is that when anti-matter and matter interact, the encounter results in the annihilation of the two with the release of energy. When a positron and an electron collide they annihilate resulting in the complete conversion of the electron and positron into a pair of 511 keV gamma-rays traveling at nearly 180° opposite directions from the annihilation point. It is the coincident detection of the two oppositely directed 511 keV gamma-rays that is used to compute a tomographic back projection and thus reconstruct a three dimensional image of the biodistribution of the emitting source [18].

The distance traveled by the positron prior to annihilation sets the lower limit of resolution for PET imaging. A typical clinical PET system is made of a stationary ring of detector modules made of crystal scintillators that are read out by individual arrays of photomultiplier tubes similar to the method used in gamma cameras (minus the lead collimators). PET typically uses photomultiplier tubes smaller in size than those used in a SPECT gamma camera. The patient is positioned lying flat and perpendicular to the plane formed by the ring. Tomographic slices of the patient are obtained by scanning the patient horizontally through the ring. A diagram of a PET system is shown in Figure 2.6.

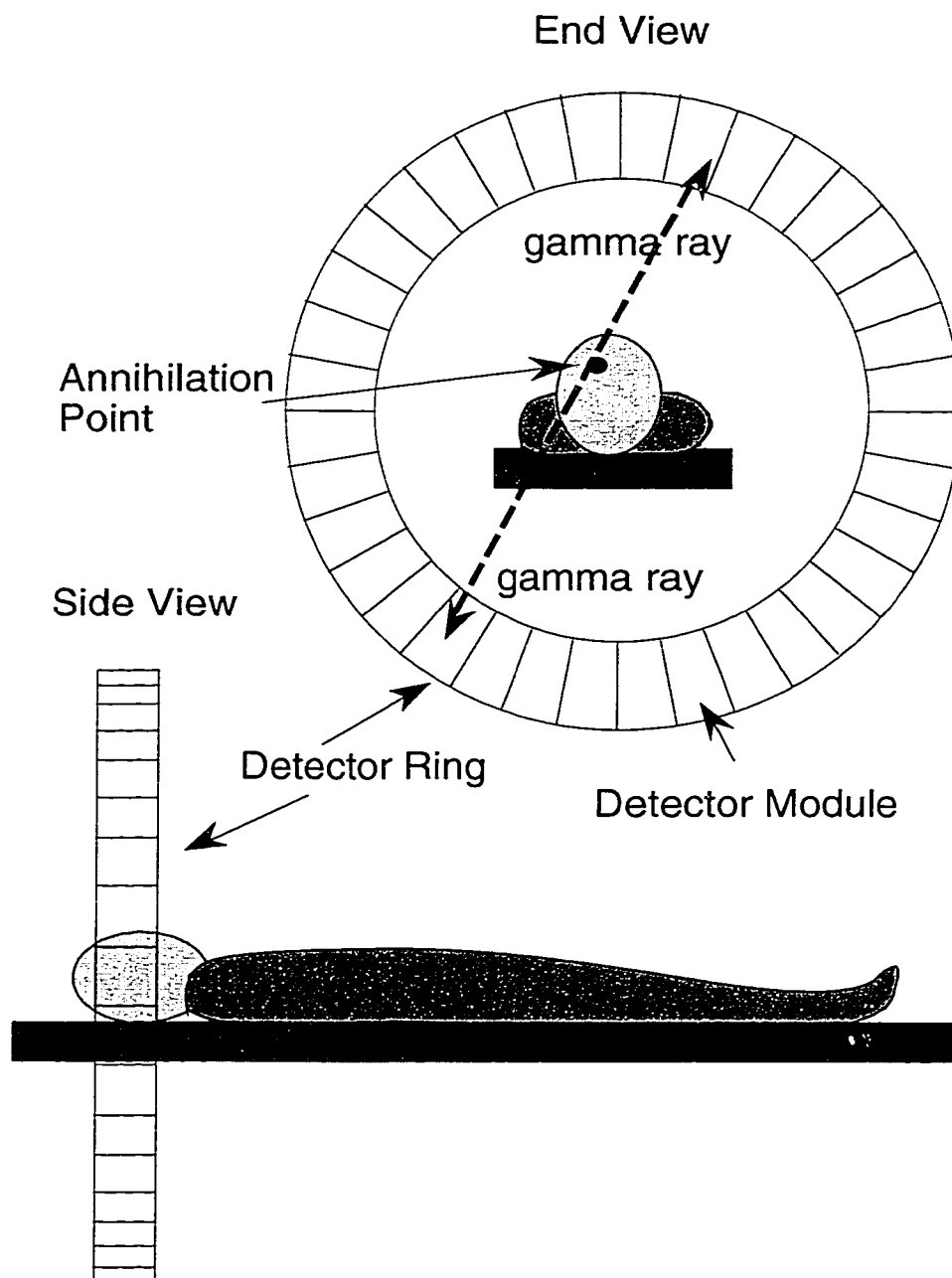


Figure 2.6: Diagram showing a side and front view of a clinical PET scanner based on a ring of detector modules which surround the patient. The case of brain PET imaging is depicted.

The line of response is determined by the coincident detection of the two gamma-rays resulting from the positron-electron annihilation. This line of response is used to build an image of the distribution of the radiotracer in a slice through the patient defined by the

plane of the detector ring. After this line is determined, all pixels of a data matrix that represent that line in the plane of the detector ring are incremented by one. A tomographic slice defined by the plane of the ring is built up after many angles of different lines of response are superimposed.

2.2 Nuclear Medicine Detector Development for Animal Imaging

The remainder of this chapter will summarize some of the detector development conducted in the application of nuclear medicine techniques to the construction of detector systems designed to do small animal imaging. Standard medical imaging devices made for clinical applications have been used for animal research. For example, Bakker et al. [19] used a standard gamma camera to investigate a tumor detection technique that used a radiolabeled ligand (Tyr-3-octreotide) that was designed to bind to specific receptor molecules (somatostatin) that are found on the surface of certain tumor cells. Bakker et al. localized pancreatic tumors in rats using this method.

The work being done to construct animal-imaging-specific detectors can be divided into two categories. The first includes the use of imaging devices that use collimators to image the radiopharmaceuticals and the second category uses electronic collimation to image the biodistribution of PET radiopharmaceuticals. Most of the detector systems described here have been used in actual animal studies within the last five years. The primary motivation is to design instruments that will allow extensive testing of newly developed radiopharmaceuticals *in vivo* in animals prior to clinical use in humans [20]. The method for screening novel radiopharmaceuticals is through post mortem tissue studies involving mice and rats [21]. These detector systems are of interest to pharmaceutical

companies since drug development can cost over several million dollars per new compound and take 10-15 years [22].

The detector system characteristics of spatial resolution, usually quoted as full-width at half maximum (FWHM) for an imaged point source, and sensitivity represent the primary parameters by which to compare different detector systems. PET systems use detection methods which do not require physical collimators, consequently they have the highest sensitivity. The sensitivity of a typical small animal PET system is of the order of 100-200 cps/ μ Ci for a resolution of 2-3 mm FWHM. The sensitivity of a gamma camera system using a high resolution collimator appropriate for small animal imaging would have a sensitivity of an order of magnitude lower to achieve the resolution comparable to a PET system. However, present day PET imaging requires the use of positron emitting isotopes with half-lives of less than a couple of hours which limit their use to short duration studies and requires that the isotope be locally produced. Since PET has great clinical value in human diagnostics it is necessary to use animal models to test new PET pharmacological agents before they are used in humans [20]. Below is a table highlighting some of the most commonly used positron emitting isotopes used in nuclear medicine which are produced by using large expensive on-site production devices (cyclotrons)[23, 24].

Positron Emitting Isotope	half-life (minutes)	Positron E_{\max} (MeV)
oxygen-15 (^{15}O)	2.07	1.72
nitrogen-13 (^{13}N)	9.96	1.19
carbon-11 (^{11}C)	20.4	0.96
fluorine-18 (^{18}F)	109.7	0.64

Table 2.1: Table of positron emitting isotopes that are most commonly used as radiopharmaceutical labels in nuclear medicine applications.

Note that ^{18}F is the one of the most often used for positron imaging as it has the longest half-life and its low maximum positron kinetic energy (E_{\max}) results in a 2.4 mm

maximum range in water. As mentioned earlier, the best theoretical resolution obtainable in PET is a function of the range of the positron in the tissue before it annihilates resulting in the two gamma-rays. Table 2.2 lists gamma-ray emitting isotopes that are most commonly used as radiopharmaceutical labels in nuclear medicine planar and SPECT imaging applications [2, 25, 26]. The radioisotope ^{99m}Tc is the most often used nuclear medicine radiopharmaceutical and is obtainable from molybdenum-99/technetium-99m generators which need to be re-stocked every few days [27].

Isotope	Half-life	Photon energies (keV) (photon abundance)
technetium-99m (^{99m}Tc)	6.02 hours	140 (89%)
indium-111 (^{111}In)	2.83 days	170 (94%), 240 (90%)
gallium-67 (^{67}Ga)	3.25 days	93 (37%), 185 (20%), 300 (17%), and 394 (4%)
iodine-123 (^{123}I)	13.3 hours	159 (84%)

Table 2.2: Table of gamma-ray emitting isotopes that are most commonly used as radiopharmaceutical labels in nuclear medicine applications.

It is therefore clear that both PET and single photon imaging have their place in biomedical research. Resolution and sensitivity, as will be pointed out, are not the only important characteristics of a detector system. For instance, the need to optimize imaging for a particular isotope may be an important detector characteristic for a particular animal imaging application. However, for research imaging of mice and rats, the main parameter to consider is spatial resolution. If a detector system cannot achieve the spatial resolution needed for small animal research it will not be useful regardless of its sensitivity. Often low sensitivity can be compensated for by extended imaging times which is usually possible with animals.

All but three of the detector systems described below were designed and tested to be used to image nuclear medicine radiopharmaceuticals such as found in SPECT and PET imaging. Although it is possible to label many compounds with SPECT and PET isotopes this requires special expertise and, for the case of PET, expensive on-site production

facilities. A discussion pointing out the unique capabilities of the detector system that is the topic of this dissertation will follow the summary of present detector development.

2.2.1 Pinhole Collimated Gamma Cameras

The first nuclear medicine imaging research involving animals used standard clinical gamma cameras with pinhole collimators. The use of pinhole collimators still continues with the application of new techniques to obtain SPECT images with pinhole collimators[28]. As discussed earlier, the major limitation of the pinhole camera is its relatively poor sensitivity compared to parallel hole collimators. It also suffers from limited field of view at high magnification.

Weber et al. [29] and Jaszczak, et al [30] describe a pinhole SPECT using a single pinhole collimator attached to a clinical single head SPECT scanner. Recently, Ishizu et al.[28] report using four pinhole collimators attached to a standard clinical four-head SPECT scanner. They obtained a spatial resolution of 1.65 mm FWHM to obtain images of rat brains using ^{99m}Tc -hexamethyl-propyleneamine oxime (HMPAO) and to perform heart imaging studies with ^{99m}Tc -methoxyisobutyl isonitrile (MIBI). By taking advantage of the magnification effect of a pinhole camera one achieves high resolution and the best sensitivity is obtained if the animal is close to the pinhole. Weber and Ivanovic [31] give a concise appraisal of the present state of nuclear medicine imaging using pinhole SPECT. Present pinhole based SPECT detectors achieve a sensitivity on the order of 5 cps/ μCi with resolutions of 4.0 mm for source distances of 5.0 cm. This low position resolution makes it unacceptable for studies utilizing laboratory mice. In addition, the detector systems were standard expensive nuclear medicine SPECT systems which were outfitted with specially designed pinhole collimators. This type of system could not be made generally available to molecular biologists.

2.2.2 Parallel hole Collimated Gamma Cameras

Dilmanian et al. [32] reported on the development of a high resolution SPECT system to image ^{125}I in rats and mice. The scintillation light detector of their gamma camera was quite different from the typical detector used in SPECT and PET. They used a very expensive micro-channel plate dynode structure photomultiplier tube that had an active diameter of only 15 mm, called a Photon-Counting Image Acquisition System (PIAS) made by Hamamatsu Corporation [33]. The tube has a fiber optic face plate window 15 mm in diameter, a bialkali photocathode, a three stage micro-channel plate dynode structure, and a silicon position sensitive detector. This type of expensive detector is no longer available, but at the time no practical position sensitive photomultiplier tubes were yet obtainable. The scintillator was a 0.7 mm thick NaI(Tl) plate with a lead glass parallel hole collimator. They employed a fiber optic taper to enlarge the area imaged to 26 mm in diameter and achieved a spatial resolution of 0.7 mm FWHM with a sensitivity of 3.6 counts/minute/ μCi . The instrument was used to obtain SPECT images of a rat's thyroid gland and a mouse's lungs. This detector system is one of the three systems described here which was optimized for ^{125}I . Though it had a resolution of the order of 1 mm it had a very limited field of view, the active area of their detector with the use of an fiber optic taper was only 26 mm diameter. The detector system developed for this dissertation has a resolution of 1.76 mm FWHM and an active area of 110 mm.

Antich et al. [34, 35, 36] developed two systems for small animal imaging that used plastic scintillators and the Hamamatsu R2486 position sensitive photomultiplier tube to image ^{125}I . Their first system was based on the use of a 56 mm diameter, 1.5 mm thick plastic scintillator plate and a pinhole collimator. With this system they reported high resolution imaging of rat brain blood flow with ^{125}I labeled compound. To allow for whole body imaging they devised their latest system with two layers of plastic scintillating fibers to form a cylinder around the animal. One layer of fibers had a right-hand pitch and the

other had a left-hand pitch. They could determine the location of the gamma-ray interaction in the fibers by reading out the right and left-hand pitch fibers separately. The collimator was a multi-hole large-mesh cage-type collimator with an average spatial resolution of 3.1 mm and a tomographic slice thickness of 6.6 mm. This device would only be useful for low energy gamma-rays because of poor absorption of the gamma-rays by the plastic scintillator. Their detector systems were also designed with ^{125}I imaging as the target isotope. However their low position resolution (>3 mm FWHM) make it marginally useful for small animal imaging.

A collaboration of researchers in Rome, Italy, led R. Pani, have reported development of a small gamma camera based on a 40 mm x 40 mm size scintillator array of 0.6 x 0.6 mm x 10 mm array elements made out of the recently developed crystal scintillator Yttrium Aluminate Perovskite (YAP) [37, 38, 39]. Their detector used the Hamamatsu R2486 position sensitive photomultiplier tube and a parallel hole lead collimator that had 0.9 mm diameter openings and 0.25 mm thick septa. The resulting spatial resolution of the system for imaging $^{99\text{m}}\text{Tc}$ was 1.4 mm +/- 0.2 mm. The authors reported obtaining bone images of a rat that had been injected with $^{99\text{m}}\text{Tc}$ -methylene diphosphonate (MDP).

2.2.3 Focused Collimator Tomograph

Ochoa et al. [40] have been developing a unique x-ray/gamma-ray counter detector system that uses a large solid angle, focusing collimator to image radiopharmaceuticals labeled with a dual photon emitting radioactive nuclide. This type of radioisotope emits gamma-rays and x-rays in near coincidence but not in a collinear direction. For instance, ^{125}I is this type of dual photon emitting isotope. The detector system using the focused collimator cannot be used to image positron emitting isotopes since the two gamma-ray emitting in positron annihilation travel collinear in opposite directions. This collimator

could not work with positron emitters. Ochoa et al. are currently constructing a collimator that completely surrounds the volume to be imaged. They use NaI(Tl) crystal scintillator coupled to a standard photomultiplier tube (not position sensitive). The volume to be scanned is moved in all three coordinates so that the focal point of the collimator is used to take data at a single volume element at a time. The electronics only accepts data if a two photon event is detected. They anticipate a resolution of 1.4 mm FWHM.

This is the third system that was designed to image ^{125}I and their anticipated resolution of 1.4 mm FWHM is certainly adequate for small animal imaging. The major limitation of their system is the inability to perform a whole body dynamic imaging. This system is only appropriate to image small volumes such as the brain of a mouse or rat and is not be appropriate for whole body dynamic imaging studies because all of the sensitive volume data are collected sequentially.

2.2.4 PET

Spatial resolution of present clinical PET systems is between 4-6 mm. It is clear that this needs to be improved for small animal research. Most PET research involving small animals use radiopharmaceuticals labeled with the positron emitting isotopes ^{18}F , ^{13}N , or ^{11}C . To obtain the best position resolution ^{18}F is used since it has a short positron range. It has been shown with phantom studies utilizing iterative image reconstruction algorithms that a resolution of 1.1 mm FWHM is possible with PET [41].

Recently there has been much work on the development of PET detectors for small animal research as compared to non-PET imaging. Described below are examples that highlight some of the recent detector development work being done by various groups around the world in this area. Groups that have actually used their system in animal studies will be the primary focus of this summary. The primary goal for the development of these instruments is to allow extensive testing of newly developed PET radiopharmaceuticals *in*

vivo in animals before they are tested in humans [20]. Moreover, these detector systems require the use of short lived positron emitting isotopes that need to be produced locally and chemical expertise in the field isotope labeling is essential if special tracer molecules are to be used. One group which has a PET isotope facility is attempting to utilize PET isotopes to investigate gene therapy imaging rats using the UCLA MicroPET system which will now be described [42,43].

UCLA

Several researchers at UCLA have collaborated on the development and use of a animal PET scanner called MicroPET [44, 45, 46, 47, 48]. This high resolution PET scanner consists of a ring of 30 position sensitive scintillation detectors, each consisting of an 8x8 array of small lutetium oxyorthosilicate (LSO) scintillation crystals connected by plastic optical fibers to a Phillips Photonics Inc. [49] XP1722 multi-channel photomultiplier tube. LSO is a recently developed crystal scintillator whose properties such as high density and fast speed make it a good choice for PET scanners. The UCLA detectors have an intrinsic resolution averaging 1.68 mm and a 2.4 nanoseconds (ns) timing resolution for 511 keV gamma rays. These parameters demonstrate that the system is well suited for PET imaging of animals as small as mice. The timing resolution indicates that the detector can be brought close to the animal to achieve good sensitivity. The detector ring diameter is 17.2 cm with an imaging field of view of 112 mm transaxially by 18 mm axially. These dimensions indicate that the system can be used with animals as large as small monkeys. The authors report a reconstructed image resolution of 2.0 mm at a distance of 1 cm from the center of the scanner resulting in a volume resolution of 8 mm³. The UCLA scanner has the highest combined resolution and sensitivity of any multi-ring scintillator based PET scanner currently in active use.

The MicroPET has been used in brain amino acid pathway studies in primates and rodents involving the injection of 6-[^{18}F]fluoro-L-m-tyrosine. The *in vivo* metabolic pathway of this compound was compared to that of 4-[^{18}F]fluoro-L-m-tyrosine and 6-[^{18}F]fluoro-L-3,4-dihydroxyphenylalanine to study dopamine receptors in the brain [50]. In another study, the scanner was used to study cerebral metabolic rates for glucose by feeding ^{18}F -fluoro-2-deoxyglucose (FDG) to monkeys and then imaging the dynamic biodistribution of the FDG [51]. Most recently the MicroPET has been used in research that utilized PET labeled marker substrates to detect the presence of particular enzymes resulting from the expression of a virus gene that was introduced into cultured tumor cells that were then injected into rats. The researchers used radiolabeled 5-iodo-2'-fluoro-2'-deoxy-1-beta-D-arabino furanosyluracil (FIAU) as a marker substrate to measure the effectiveness of gene transfer techniques being tested for gene therapy.

National Institutes of Health (NIH)

At NIH in Bethesda, MD, researchers have been developing high resolution PET detectors for use in small animal research at NIH [52, 53]. Their latest design is based on the use of arrays of LSO scintillating crystals coupled to Hamamatsu R5900-C8 position sensitive photomultiplier tubes. By using three-dimensional image reconstruction computer codes they have been able to approach one millimeter resolution. In addition, the group is pursuing higher resolution PET for small animal imaging by combining different types of scintillators to reduce the inherent uncertainty of determining at what depth the 511 keV gamma-rays interact within the scintillating crystal before releasing scintillation photons. This depth of interaction uncertainty contributes to the final spatial resolution in the reconstructed image. Improved spatial resolution can be realized if this depth of interaction uncertainty can be reduced. The solution, based on the so-called phoswich concept, is to

employ columns of three different scintillator types, such as BGO-GSO-LSO, instead of uniform scintillator pixels.

RATPET

A collaboration, between the MRC Cyclotron Unit at Hammersmith Hospital in London, CTI PET Systems in Knoxville, Tennessee, and Byars Consulting in Oak Ridge, Tennessee has produced a small-diameter positron emission tomograph for small animal PET studies. The detector system is referred to by the collaboration as RATPET. The device uses BGO scintillating crystals in 16 detector blocks that are configured such that the axial field of view is 5.0 mm and the tomograph diameter is 115 mm. The best spatial resolution the detector can achieve at the center of the field of view is 2.3 mm FWHM. The system has been in use since 1993 and has been used primarily to perform rat brain imaging studies [21].

Julich, Germany

Weber et al., in Julich, Germany are developing a PET system for small animal research which utilizes arrays of YAP crystal scintillator mounted to Hamamatsu R3941 position sensitive photomultiplier tubes. Their detector, which they refer to as the TierPET, ("Tier" is German for animal) consists of four detector heads positioned on a rotating gantry. Preliminary results indicate a spatial resolution of 2.0 mm FWHM. They report their intention of adding more detector heads to improve the system performance. A useful feature of this animal PET scanner is its ability to be positioned in various detector-to-detector spacings to optimize either the spatial resolution or the sensitivity for dynamic studies of radiopharmaceutical uptake. Sensitivity increases when the detector heads are brought closer together, however, at the expense of spatial resolution. During instrument

testing the TierPET system has been successfully used to image the dopamine D₂ receptor binding in the rat brain using as the ligand [¹⁸F]methyl-benperidol [54].

HIRESPET Collaboration

A group of researchers from six institutions in Italy have formed a HIRESPET collaboration to develop high spatial and temporal resolution detector systems for nuclear medicine tomography using PET and SPECT. The collaboration has constructed a two-head PET scanner suitable for small animal research. The scanner is based on two arrays of YAP scintillating crystal attached to Hamamatsu R2486 position sensitive photomultiplier tubes. The authors report obtaining a spatial resolution of 1.2 mm FWHM [55]. In order to improve sensitivity, their detector system makes use of the Compton scattered portion of the energy spectrum since the photopeak fraction for YAP at 511 keV is only 3% which is much lower than in scintillators such as BGO, GSO and LSO which are other crystal scintillators used to detect 511 keV gamma-rays.

Oxford Positron Systems Ltd., England

The company Oxford Positron Systems Ltd. in England in collaboration with Packard Instrument Company in the USA sells a small animal PET scanner developed by Alan Jeavons [56]. This detector is based on a high density avalanche chamber (HIDAC) developed at CERN, Geneva, Switzerland. The HIDAC uses an enclosed gas chamber that electrically detects the ionization of the passing 511 keV gamma-rays with a spatial resolution of 0.75 mm FWHM for ¹¹C imaging. This type of detector is common in nuclear particle physics research and is based on the multiwire proportional chamber (MWPC) that was invented by Dr. George Charpak in 1968 at CERN, Geneva, Switzerland [57]. The ionizing gamma-ray is converted (inducing the emission of electrons) by a lead converter foil, and the secondary electron passing through the gas

induces an avalanche charge multiplication that amplifies the ionization signal. No scintillators or photomultiplier tubes are used in this detector. The HIDAC has high sensitivity, however, it practically lacks energy resolution, a limitation which precludes this device from being used in situations where scattered radiation is a concern. However, the HIDAC was able to delineate regional tissue function using ^{18}F -fluoro-2-deoxyglucose (FDG) at a resolution of 2.6 mm FWHM within small tumors in a study that imaged 30 mice with implanted tumors [58]. The system offers the highest spatial resolution of any small animal PET.

Hamamatsu Corporation, Japan

Researchers at Hamamatsu Corporation in Japan have been developing a PET system for small animal studies [59 & 60]. They have developed a detector using a large number of small BGO scintillator crystals (2.8 mm x 6.8 mm x 30 mm) coupled to R5900-C8 position sensitive photomultiplier tubes. They are achieving position resolutions on the order of 3 mm (FWHM) for monkey studies using ^{11}C labeled ligands. The detector system is composed of 240 block detectors, each of which consists of a R5900-C8 position sensitive photomultiplier tube, and an 8x4 BGO scintillating crystal array; a total of 7,680 crystals, 480 per ring are used. Their system was specially designed to investigate various brain specific PET pharmaceuticals prior to applications in humans by using a monkey in a sitting position. The researchers at Hamamatsu are also developing a detector system based on LSO scintillating crystals.

Sherbrooke University in Quebec, Canada

Researchers at the Sherbrooke University in Quebec, Canada have developed and are using a PET system which uses avalanche photodiodes (APD) instead of photomultiplier tubes as scintillation light detectors. Avalanche photodiodes are solid state light detectors that take the place of photomultiplier tubes. They can be made to be very compact, are fast, and have a very high quantum efficiency. Although their gain is low compared to photomultiplier tubes, they can be used in many applications that do not need as much signal amplification. The arrays of APDs used at Sherbrooke University are coupled to BGO scintillator crystal arrays and the authors report a spatial resolution of 3 mm FWHM. Studies of mammary adenocarcinoma tumor studies with the positron emitter ^{64}Cu were performed with this system [61].

Some Other Related Efforts

Other PET detector development research not yet involving animals is ongoing based on new PET configurations. For example Fries et al. also report developing an APD based PET detector. In their case they use the crystal scintillator LSO coupled to avalanche photodiodes arranged in a 2x8 array to form a detector module taking the place of a photomultiplier based detector module [62]. In addition, a group of researchers in Brussels, Belgium have developed a small animal PET scanner that actually combines scintillator technology with wire chamber technology [63, 64]. The cylindrical ring configured detector uses arrays of BaF_2 scintillation crystals and a photosensitive wire chamber filled with tetrakis-dimethylamine-ethylene (TMAE) gas. The main advantage of using a wire chamber is the ability of achieving good resolution over a large area with a much lower cost compared to using photomultiplier tubes. They report a system spatial resolution of 3 mm to 6 mm FWHM.

APD technology has also recently been applied to the development of an radioactive isotope imaging device called the IDE Bioscope 3250 marketed by the company Integrated Detector and Electronics [65]. The device is designed to replace autoradiographic film for imaging of thin tissue samples that have been labeled with electron or gamma-ray emitters. The detector is a 300 μm thick double-sided silicon sensor which they claim can do real-time imaging at a resolution of 10 μm .

2.2.5 Small Animal Imaging Discussion

The advances in the last ten years in PET and non-PET imaging gamma-ray detector development for small animal imaging has been rapid. The biological animal studies that have occurred are mainly concerned with radiopharmaceutical development for later applications in disease progression and response to therapy in humans. Such areas as cancer research and neurobiology research (i.e. dopamine and cocaine receptor studies) are the main areas of animal research which have recently been taking advantage of small animals detector systems.

There exist many application specific concerns that dictate the design of a particular detector system. Spatial resolution clearly needs to be improved to facilitate animal research involving small animals such as mice and rats. For dynamic studies sensitivity is of great concern since detection rate limits the rate at which biological processes can be detected. Both animal SPECT and PET are achieving spatial resolutions on the order of 1 to 2 mm FWHM. It is not clear if PET techniques can be used to go below 1 mm FWHM because of the inherent distance that a positron can travel before annihilating in a collision with an electron. SPECT, in principle, has no such limitation, however there is always the trade-off between higher resolution resulting in lower sensitivity when conventional collimators are employed.

The next chapter will outline the development of a non-PET detector system which has been optimized to detect the x-ray and gamma-ray emission of iodine 125 (^{125}I). This isotope can be of particular importance for molecular biologists doing imaging research involving mice and rats. As set forth in the Introduction, the detector developed here is the only imaging system capable of allowing a researcher to test a large number of commercially available biological tracers in small animals such as mice. This detector system provides the ability to follow biological processes on a molecular level that are of considerable general importance for both theoretical and therapeutic reasons. As mentioned earlier Dupont NEN, Inc. [1] has over 150 tracers (proteins, anti-bodies, and nucleotides) labeled with ^{125}I which were intended for *in vitro* non-imaging applications but can also be used for *in vivo* imaging studies involving small animals with the novel detector system described here.

Chapter 3

Development of an ^{125}I Imaging Detector System

This chapter will describe the development of a novel imaging system designed for the detection of the x-ray and gamma-ray emissions of ^{125}I . Some of the results outlined in this chapter have been reported in several publications [66, 67, 68, 69]. The primary focus of the development of this detector system was the utilization of recently available position sensitive photomultiplier tubes coupled to scintillator crystals. The detector development progressed through three stages. In the first stage, the feasibility of imaging the gamma-ray and x-ray emissions of ^{125}I was tested by using a small area detector system (active field of view of ~ 50 mm in diameter) that utilized a crystal scintillator plate. In this case the position sensitive photomultiplier tube was a 75 mm diameter (model R2486) manufactured by Hamamatsu Inc. In the second stage, the Hamamatsu 125 mm diameter position sensitive photomultiplier tube (model R3292) was coupled to an array of small scintillating crystals instead of a scintillator plate. The primary detector component used throughout the development of this detector system is the position sensitive photomultiplier tube manufactured by Hamamatsu Corporation. Both tubes are very similar in design and operation with the primary difference being the size of the detection area. At the third stage

of the project a matrix crystal array with smaller individual elements and an optimized collimator design were implemented.

This chapter will first describe the goals of the project by introducing the molecular biology applications motivating the specific design requirements of the detector system for imaging the gamma-ray and x-ray emissions of ^{125}I . Following this will be a detailed description of the detector prototype instrumentation that eventually resulted in the final system. The main detector instrumentation difference between the early YAP crystal based prototype and the final CsI(Na) crystal scintillator based device was the use of different position sensitive photomultiplier tubes and different scintillators; the basic electronic readout method for both are the same. Following this will be detailed descriptions of the performance of the YAP based and CsI(Na) based detectors. The performance of the final optimized detector system in a mouse study with ^{125}I will be detailed.

3.1 Project Overview

The goal of this project was to develop a prototype small field-of-view, high resolution, gamma camera that would have a suitable spatial resolution to investigate the possibility of imaging gene expression in live small animals, particularly in mice. The scientific motivation for developing this detector system is the desire to image gene expression and regulation in the mouse brain and nervous system. Such a detector system could provide a tool to investigate *in vivo* gene expression and regulation with ^{125}I incorporated into molecular probes to study neural gene expression *in vivo* using antisense RNA techniques. These techniques are described in Appendix A.

As part of the research and development process, prototype detectors were built and tested in biological studies using mice. The biological investigations done in the prototype development stages provided valuable insight which guided the final system design.

3.1.1 Existing *In Vivo* Methods

Most methods to study gene expression in animals are performed *in vitro*. The methods require that the animal be sacrificed and then very thin slices are made from either the whole animal or of organs of interest. At present, *in situ* hybridization and immunochemical assays are the primary methods to follow gene expression and regulation in small animals. The ability to detect gene expression, *in vivo*, for an extended period of time in a given organism allows the researcher to follow gene expression through various stages of organism development and under different biological conditions for the same organism. By attempting *in vivo* to detect the protein products of gene expression much can be learned about the function of a gene. This is possible with the use of radioisotope labeled ligands and antibodies (see Appendix A) and using conventional nuclear medicine imaging devices when done with humans and large animals. A more direct way would be to detect the mRNA resulting from transcription of a gene. In either case, as attested by the work described in Chapter Two of this dissertation, small animal specific medical imaging type gamma cameras and PET systems are of great interest. To be fully useful, the *in vivo* gene imaging technique should be real-time, quantitative and able to follow an organism over extended periods of time, i.e., several days. It is clear that the ability to follow biological processes on a molecular level *in vivo* is of considerable general importance for both theoretical and therapeutic reasons.

3.1.2 *In Vivo* Gene Studies

Presently there are two direct means of imaging gene expression (transcription) and regulation *in vivo* that are currently in use. One method uses a technique in which the coding region for a gene is attached (ligated) to a promoter sequence of a gene being studied which is then incorporated into a target organism. This gene, ligated to the

promoter of the gene under study, is referred to as a reporter gene. When the reporter gene is expressed its gene product, which is not normally endogenous to the organism, is expressed and various methods could be used to detect it. The second method is the “antisense” method that uses a chain of nucleotides that are complementary to an mRNA molecule under investigation [70, 71, 72].

3.1.2.1 Reporter Gene Detection

One reporter gene technique uses the expression of a green fluorescent protein (GFP) fused to a specific gene promoter that is being studied, but the GFP method only works for small transparent animals [73]. This fluorescence detection method uses a reporter gene which codes for a protein, first isolated from jellyfish, called a green fluorescent protein (GFP) [73]. The detection of the expression of this reporter gene is confirmed by viewing the specimen when it is illuminated with UV light. This method requires that the gene expression occurs in a transparent animal or is close to the surface of the animal.

Another method is the “light method” which uses reporter genes that express light emitting proteins without the need of fluorescence [74, 75]. This method incorporates into an organism a reporter gene which codes for a protein called luciferase, which is the compound that allows fireflies to glow. When the reporter gene is expressed, light is emitted without the need of a UV light source to cause fluorescence. This method also requires that the gene that is being expressed exist near the surface of the animal or is used in transparent animals.

In a variation on the reporter gene method, Tjuvajev et al. [76, 77] report using radiolabeled marker substrates to detect the presence of particular enzymes resulting from the expression of a virus reporter gene they call a “marker gene” that was introduced into cultured tumor cells that were then injected into rats. The researchers used a radiolabeled

thymidine analog, 5 -iodo-2'-fluoro-2'-deoxy-1-beta -D -arabino furanosyluracil (FIAU), as a marker substrate to measure the effectiveness of gene transfer techniques using mice that were being tested for gene therapy. They introduced into mouse tumor cells a gene from the herpes simplex virus (HSV) that codes for an enzyme called thymidine kinase (TK). The enzyme HSV-TK attaches phosphates to thymidine resulting in thymidine triphosphate, one of the four precursor nucleotides used in DNA synthesis [78]. Tjuvajev, et al. then injected ^{131}I labeled FIAU, a thymidine analog, acted upon by the enzyme HSV-TK to attach phosphates to the molecule.

FIAU normally passes back and forth through cell walls but with phosphates attached, it gets trapped in cells expressing HSV-TK to accumulate FIAU. After sacrificing the animals Tjuvajev, et al. used quantitative autoradiography to measure enhanced radioactivity in the regions of the rat brain that had been the target of the gene therapy[76]. In addition, they also used a standard clinical gamma camera for limited *in vivo* imaging to test the presence of the marker gene in tumors that had been injected into the flanks of rats [77]. Gamma camera imaging and SPECT were performed using a dual-head, ADAC Genesys gamma camera with a high efficiency-high-resolution medical collimator. The best resolution this gamma camera could give them was ~0.5 cm. They showed accumulation of the radiolabel in the tumor site. Srinivasan et al. [42] reported a very similar study involving mice with FIAU labeled with ^{18}F , a PET isotope. Both of these methods require a large investment in time and experience in breeding a transgenic animal which has the reporter gene.

3.1.2.2 Gene Imaging via Antisense RNA

Antisense RNA probes have been constructed and introduced into live organisms. These probes make use of radioactive labeling to facilitate the detection method. When the information stored in the sequence of DNA molecule of a gene is "expressed" it

is transcribed into an RNA molecule referred to as a messenger RNA (mRNA) transcript. The process by which RNA polymerase produces a mRNA from DNA template is called transcription. The mRNA is then acted upon by cellular processes that translate the unique nucleotide sequence into a particular protein molecule. It is the unique mRNA molecule which is the target molecule to be studied in antisense imaging. A complementary or “antisense” molecule contains a sequence of bases which will bind to the “sense” part of the RNA molecule. For instance, an RNA sequence with a series of bases UUGU would require an antisense sequence with the bases AAC A since A binds to U and C binds to G. RNA is described in more detail in Appendix A.

The antisense complement to the target RNA molecule is labeled with an isotope such that a detectable amount of labeled antisense RNA molecule will bind to enough target RNA to allow for the biodistribution of that gene expression to be determined. Figure 3.1 illustrates the use of the antisense mRNA molecule as the probe for the target molecule.

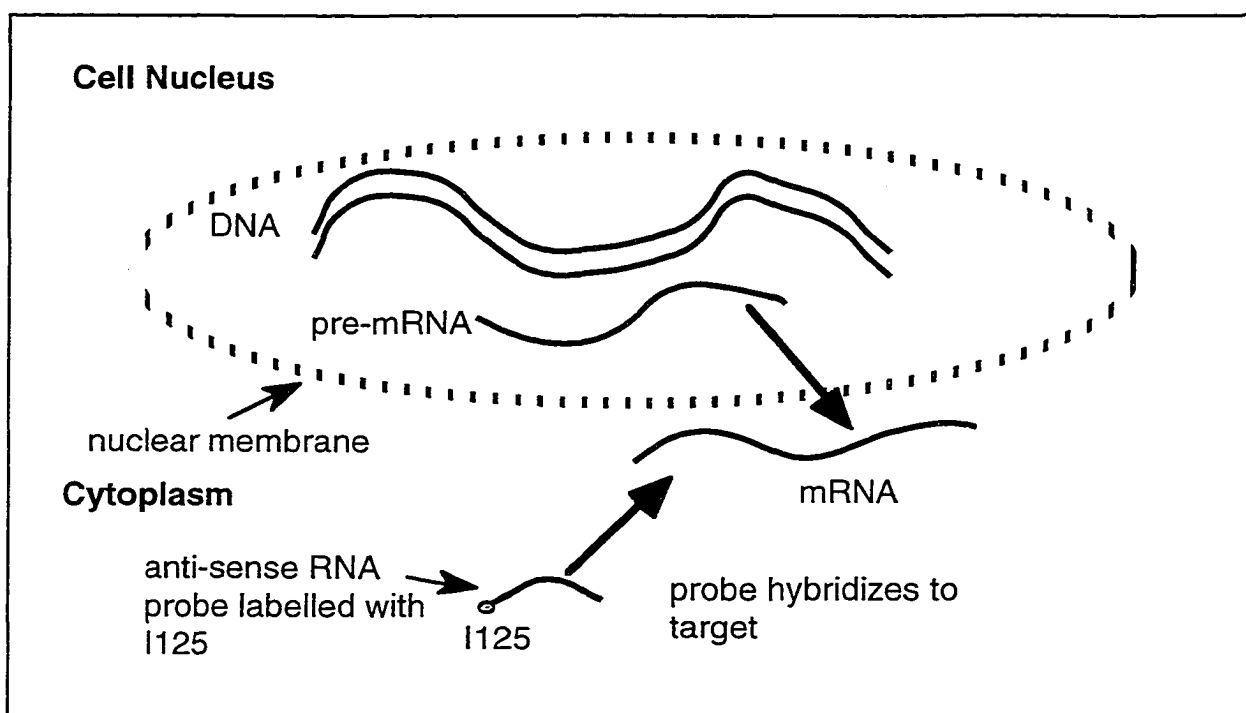


Figure 3.1: Antisense RNA probe linked to ^{125}I .

Dewanjee et al. [70, 71, 72] have shown that it might be possible to construct and successfully use radiolabeled antisense RNA probes to detect target mRNA *in vivo* in laboratory animals using a standard gamma camera as the detector system. Dewanjee et al. injected ^{111}In (171.2 keV) radiolabeled antisense and sense mRNA probes into mammary tumor-bearing BALB/c mice. Tumor cells are replicating at an abnormal high rate thus they are producing unusually large amounts of specific mRNAs. Dewanjee and his colleagues constructed antisense RNA probes to the *c-myc* oncogene gene that was being expressed at an exaggerated rate, thus there was sufficient mRNA to which to bind. The gamma camera system they used produced images demonstrating the presence of binding of the antisense molecule to its target mRNA with a spatial resolution of the order of 0.5 cm.

A possible drawback to this approach is that the cell mechanism to make the translated protein may be blocked, depending on the number of antisense mRNA molecules that bind up the endogenous mRNA. This could have unwanted physiological effects on the animal that could affect experimental results and possibly, in the extreme case, eventually harm the animal. The reporter gene technique, though complicated to achieve, does not have the consequence of interfering with the function of the gene of interest though it is not gene imaging under normal conditions.

3.2 Iodine 125

As described earlier, the goal of this project is to develop a detection system capable of testing the use of radioactive ^{125}I as a label to study gene expression in a live mouse. The radioisotope ^{125}I is commonly used in molecular biology and medical research. It is readily available linked to nucleic acids, antibodies, and other ligands from companies such as DuPont-NEN which provide probes for molecular biology research [1]. Its primary applications is in *in vitro* studies. For instance, Sasaki et al. [79] used a single crystal

scintillator coupled to a photomultiplier tube to perform physiological and pharmacological studies of a class of neuroreceptor known as brain muscarinic acetylcholinergic receptors in the brains of live mice using [^{125}I]-4-iododexetimide and [^{125}I]-4-iodolevetimide as ligands. In addition, it is possible to construct DNA and RNA probes, by obtaining from DuPont-NEN, ^{125}I labeled nucleotides such as 5-[^{125}I]iodo dCTP and 5-[^{125}I]iodo dU.

3.2.1 Properties of Iodine 125

The radioisotope ^{125}I ($Z=53$) has a half-life of 60.2 days. It decays via electron capture to the excited state of ^{125}Te which leads to the emission of a 35 keV gamma-ray followed by the prompt emission (1.5 nanoseconds) of several 27-32 keV $K\alpha$ and $K\beta$ shell x-rays from the daughter product ^{125}Te [80]. The 35 keV gamma-ray is emitted in 7% of the de-excitations of ^{125}Te and in the remaining 93% of the de-excitations, ^{125}Te decays via a process called internal conversion [81]. The internal conversion process results in vacancies occurring in the inner electron shells which are filled by nearby outer orbital electrons. The energy difference between the two orbitals is released in the form of x-rays or is transferred to outer orbital electrons which are thereby ejected. These low energy electrons (a few keV), termed Auger electrons, are easily absorbed by nearby material. It is these low energy electrons which allow the visualization of a ^{125}I labeled tracer in thin tissue samples that are placed in contact with autoradiographic film [81]. The decay scheme for ^{125}I is shown in Figure 3.2.

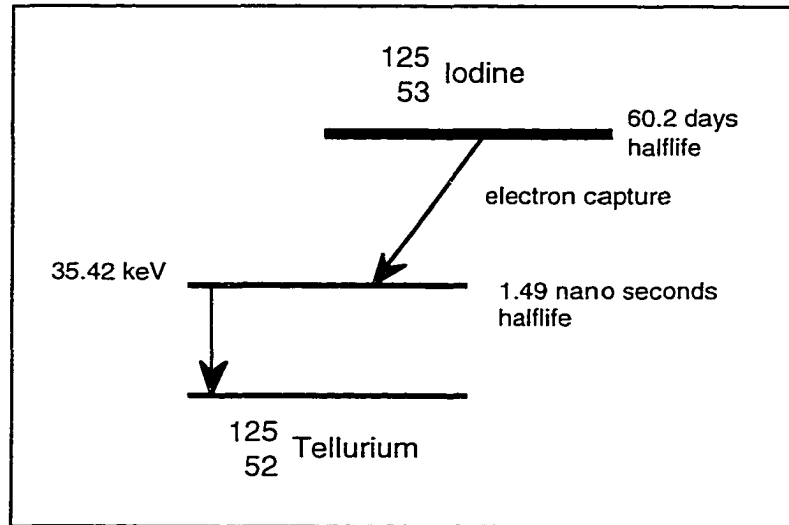


Figure 3.2. Decay scheme for ^{125}I to a nuclear excited state of tellurium 125.

The long half-life, and therefore low specific activity (2200 Ci/mole), compared to isotopes used in nuclear medicine, makes ^{125}I particularly useful for following gene expression over an extended period of time in the same animal. Eighty percent of the electron captures of the decay of ^{125}I result in K shell vacancies. After electron capture and internal conversion there are 142 detectable photons (gamma-rays and x-rays) for every 100 disintegrations of ^{125}I [81]. As many as 53.2% of the decays of ^{125}I result in coincident radiation, either in the form of two x-rays, or a single x-ray and the 35 keV gamma ray [82]. The average path length is about 1 cm in a small animal and no more than about 75% of the 35 keV photons will exit the body (assuming $0.3 \text{ cm}^2/\text{g}$ for water). The estimated probability of detecting a coincident event would be then at best 56%, obtained from squaring the probability of passage of a single photon. Because of these correlated phenomena, a coincidence condition can be set to detect preferentially the ^{125}I decays, thus reducing background radiation that constrains the lowest limit of detection of the isotope.

By using the coincidence detection mode, a definitive distribution of the ^{125}I isotope in the tissue can be obtained, even if present in minute quantities. This could be important in some applications when one is attempting to detect receptor binding without over-

saturation of the endogenous target molecule or receptor. This coincidence technique to reduce the effect of background events originating from cosmic radiation and the photomultiplier tube itself has already been shown to be useful in non-imaging applications for the detection of extremely low concentrations (on the order of an attomole) of ^{125}I linked to a probe [83].

3.2.2 Iodine 125 Production

The radioisotope ^{125}I , like many artificially generated radioactive elements is produced in nuclear reactors that utilize the fission of uranium-235 (^{235}U). For the case of ^{125}I , xenon-124 (^{124}Xe) is used as target nuclei, placed in a high neutron flux reactor. The ^{124}Xe nuclei capture a neutron resulting in the production of unstable ^{125}Xe nuclei. The ^{125}Xe nuclei then decay via electron capture resulting in radioactive daughter product ^{125}I [84].

3.3 Detector Instrumentation

As mentioned in Chapter Two, for planar single photon imaging in nuclear medicine the standard detection device is the Anger gamma camera. The best intrinsic spatial resolution of standard medical gamma cameras is about 3.5 mm FWHM which is not sufficient for experiments involving small animal imaging. It is clear that improved position resolution over a smaller area than available with clinical gamma cameras is needed. The use of smaller diameter photomultiplier tubes to construct a higher resolution gamma camera becomes a problem because of the increased dead space between photomultiplier tubes that results in a limiting packing fraction for arrays made from these tubes. However, the recently available position sensitive photomultiplier tubes make it possible to construct an improved gamma camera of a small size.

3.3.1 Position Sensitive Photomultiplier Tubes

In the last ten years, reliable high performance compact position sensitive photomultiplier tubes have been made available from industry for research[85]. By using these photomultiplier tubes, high resolution compact gamma cameras better suited for small animal imaging can now be designed. For this project the Hamamatsu R2486 and the Hamamatsu R3292 position sensitive photomultiplier tubes were used to image the scintillation light from the gamma-ray and x-ray photons emitted from the decay of ^{125}I . Many groups have been working on the development of specialized detector systems based on the position sensitive photomultiplier tube, for example Pani, et al. [86] and Yasillo et al. [87]. The operation of standard photomultiplier tubes is discussed in detail in Appendix B.

Both the model R2486 (75 mm diameter) and R3292 (125 mm diameter) operate the same way. The size of the detection area (the photocathode) is the only difference. Both photomultiplier tubes have 12 grid mesh dynode stages, arranged in the proximity focusing geometry and crossed wire anodes, the R2486 has 16(x) and 16(y) anodes whereas the R3292 has 28(x) and 28(y) anodes. A light photon entering the window and striking the photocathode, liberates photoelectrons that are directed through the dynode stages by an electric potential of typically 1200 volts. The photoelectrons are accelerated and directed to strike the dynodes resulting in a multiplication of secondary electrons which are likewise accelerated. At the end of the multiplication stage an electron cloud with a width of about 1 cm reaches the crossed wire anode stage. The individual anode wires of each axis are separated by 3.75 mm. In Figure 3.3 is a diagram demonstrating how a scintillation photon incident on the photocathode of the position sensitive photomultiplier tube results in output signals at the anodes.

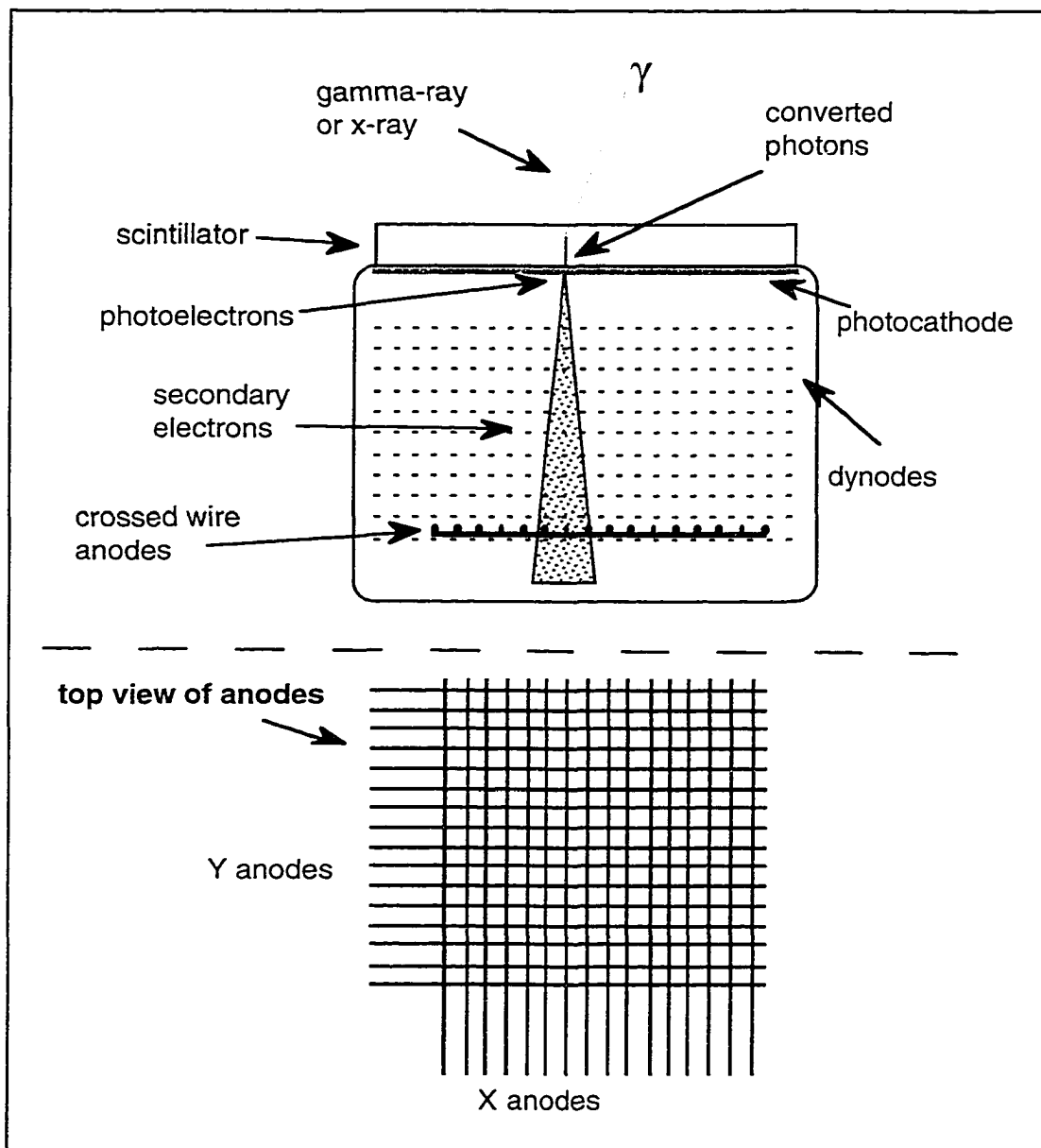


Figure 3.3: Schematic of the operation of a position sensitive photomultiplier tube with a twelve stage mesh dynode stack to provide multiplication of secondary electrons. Incident γ or x-rays induce scintillation photons in the crystal scintillator. Readout of the secondary electron shower is achieved by the crossed wire anodes.

A standard gamma camera utilizes an array of photomultiplier tubes, each requiring a separate dynode voltage divider circuit. With a gamma camera based on the position sensitive photomultiplier tube only one voltage divider circuit is needed.

3.3.2 Readout of Position Sensitive Photomultiplier Tubes

The manufacturer of the position sensitive photomultiplier tube, Hamamatsu Inc., has shown that it is possible to obtain sub-millimeter resolution with these devices if the number of primary and photoelectrons produced by the scintillation light is sufficient [88]. The larger the number of secondary electrons, the better the signal to noise ratio for a given pulse of charge resulting from the photon interaction on the photocathode. This high resolution is even possible with an inexpensive charge division readout circuit that can be purchased from the manufacturer. Figure 3.4 is a schematic diagram of the charge division readout circuit demonstrating how the signals from each anode in the same axis are joined together with resistors.

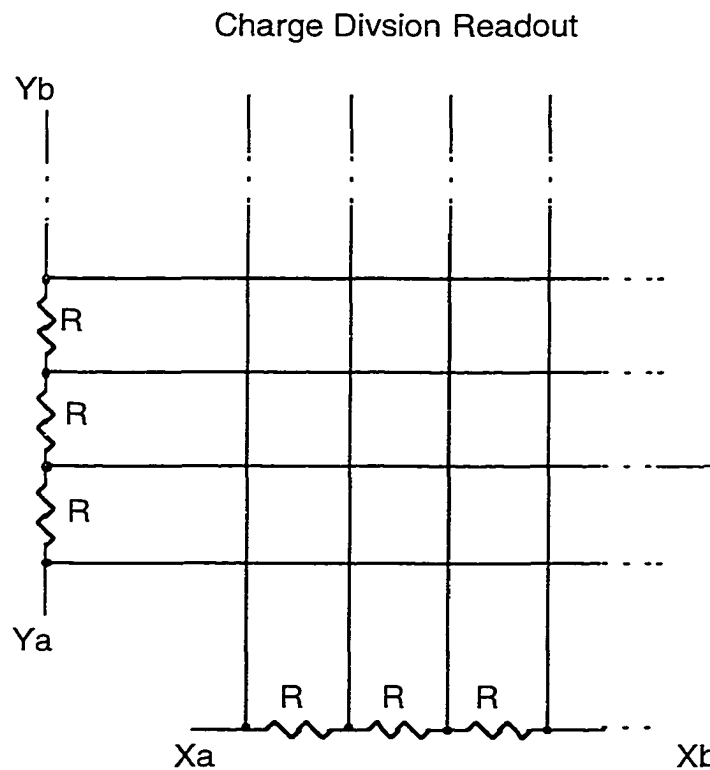


Figure 3.4: Schematic showing the basics of the charge division readout. Individual resistors (R) are placed between each anode wire in X and Y directions. The charge amplitude detected at Xa and Xb are used to determine the X location of the secondary electron shower and likewise for the Y direction.

To simplify the figure, only four anode wires per coordinate are shown in the schematic. The amplitude of the charge pulses detected at Xa and Xb, and at Ya and Yb are used to determine the X and Y location of the center of the secondary electron shower, respectively. This readout method requires only four signals to be read out by the data acquisition electronics. The disadvantage of the charge division readout is that the information about the distribution of the signal on the individual anode wires is lost since only the integrated signal is preserved and the special algorithms (discussed below) improving spatial resolution are not possible.

In applications, such as with the detection of the low energy gamma-ray and x-ray emissions of ^{125}I , if the number of photoelectrons is not sufficient to achieve the maximum designed intrinsic spatial resolution of the position sensitive photomultiplier tube, the charge division method will prove inadequate. Moreover, a non-linear spatial response occurs when the peak of the secondary electron cloud distribution is near the edge of the sensitive area and therefore the peak is no longer symmetrical. This non-linear spatial response has the effect of limiting the useful active area of the position sensitive photomultiplier tube. The best way to extract as much information on the extent of secondary electron shower in order to determine the center of gravity of the electron distribution, is to read out, individually, each anode wire. The electronic signals appearing at the anode wires are converted to digital signals by standard analog to digital converters. It is from these digitized signals that the centroid of the electron cloud needs to be computed.

3.3.3 Position Determination

Determination of the position of gamma-ray interaction in the scintillator is determined by computing a centroid of the signal distribution on the x and y anode sectors of the position sensitive photomultiplier tube. Equation 3.1 provides the centroid

calculation to determine position (X) of the interaction by using the counts (C_n) for each anode wire (X_n).

$$X = \frac{\sum_{n=1}^{\text{total}} X_n \cdot C_n}{\sum_{n=1}^{\text{total}} C_n} \quad (3.1)$$

Because of the cylindrical symmetry when the centroid of the electron cloud is calculated for the event occurring in the center of the detector, the location of the interaction point is calculated with minimal distortion. However, an edge effect occurs when a photon is detected near the outer perimeter of the area covered by the photocathode yielding an asymmetry in the charge distribution. This asymmetry results in a shift of the computed centroid value towards the center of the detector. Therefore, a resulting “crowding” of the image at the edges of the detector is observed. This can be demonstrated, for example, when an image of a mask made from a regular array of holes in a lead plate is produced.

A way to partially compensate for this image distortion is to exclude or truncate from the center of gravity calculation the anode wire sectors that carry low signals. The calculation of the truncated centroid is accomplished by using only the digitized signal of those anode wires in the calculation that have an empirically determined optimum fraction of the sum of the anode signals. This truncation fraction (F) is typically 5 to 10% and is determined experimentally by conducting imaging trials using various fraction values. The effect of this procedure is to weight the centroid calculation to follow closer the peak of the distribution rather than the center of its gravity which includes the data in the tails of the distribution.

The use of this truncated centroid technique is essential to maximizing use of the active area the position sensitive photomultiplier tube [89]. Using truncation values that are too large constrains the center of gravity calculation to too few channels and results in

distortions by producing artifacts in the form of spikes in the image. These artifacts and distortions are easily seen in Figure 3.5.

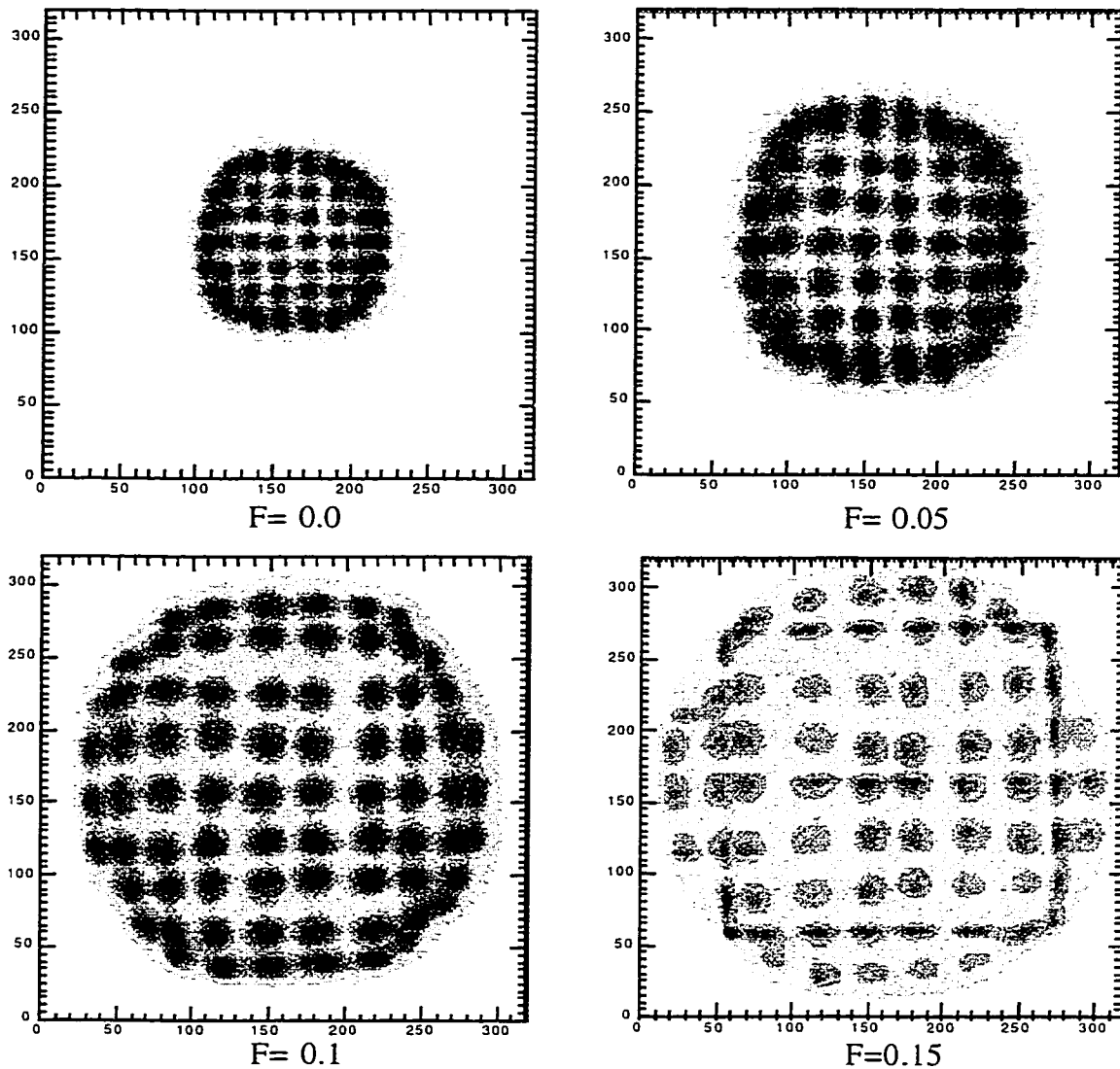


Figure 3.5: Four images for four selected values of the truncation factor (F) taken with a NaI(Tl) scintillating crystal flooded with 122 keV gamma-rays using a ^{57}Co source masked with an array of 2.5 mm diameter holes, spaced 5 mm apart. Better hole separation, especially at the edges, is possible for higher F values, until the artifacts start dominating, as seen here for the highest F -value.

Additionally, the number of electronics channels to amplify, digitize, and readout was reduced by two through connecting adjacent pairs of anode wires in the position sensitive photomultiplier tube. The original number of anode wires built into the position

sensitive photomultiplier are necessary to provide the maximum performance in applications that have sufficient number of photoelectrons and the charge division readout method is used. The pairing of anode wires in a multi-anode position sensitive photomultiplier tube is analogous to choosing the optimum width and spacing of the cathode strips of a type of detector used in high energy physics research called a multi-wire proportional chamber [90]. To minimize electronics in the multi-wire proportional chambers, it has been shown that a centroid calculation to localize the positive ion avalanche only requires three cathode stripes to be readout if the charge avalanche is centered about these strips [91].

3.3.4 Data Acquisition System

The data acquisition system used was CAMAC based, with a Macintosh Power PC workstation as the host computer interfaced to the CAMAC crate through the Jorway 73A SCSI crate controller. All data acquisition and computer imaging control software was developed with the Kmax data acquisition development system purchased from Sparrow Inc. [92]. The Kmax data acquisition system allows the user to construct software “instruments” to control the flow of data from the analog-to-digital converters (ADCs) residing in the CAMAC crate to the host computer. In addition, the Kmax development system made it possible to perform real-time computations on the data and to display the data as one- and two-dimensional histograms. The position of the interaction was computed in real-time using a centroid calculation of the anode wire outputs for both dimensions.

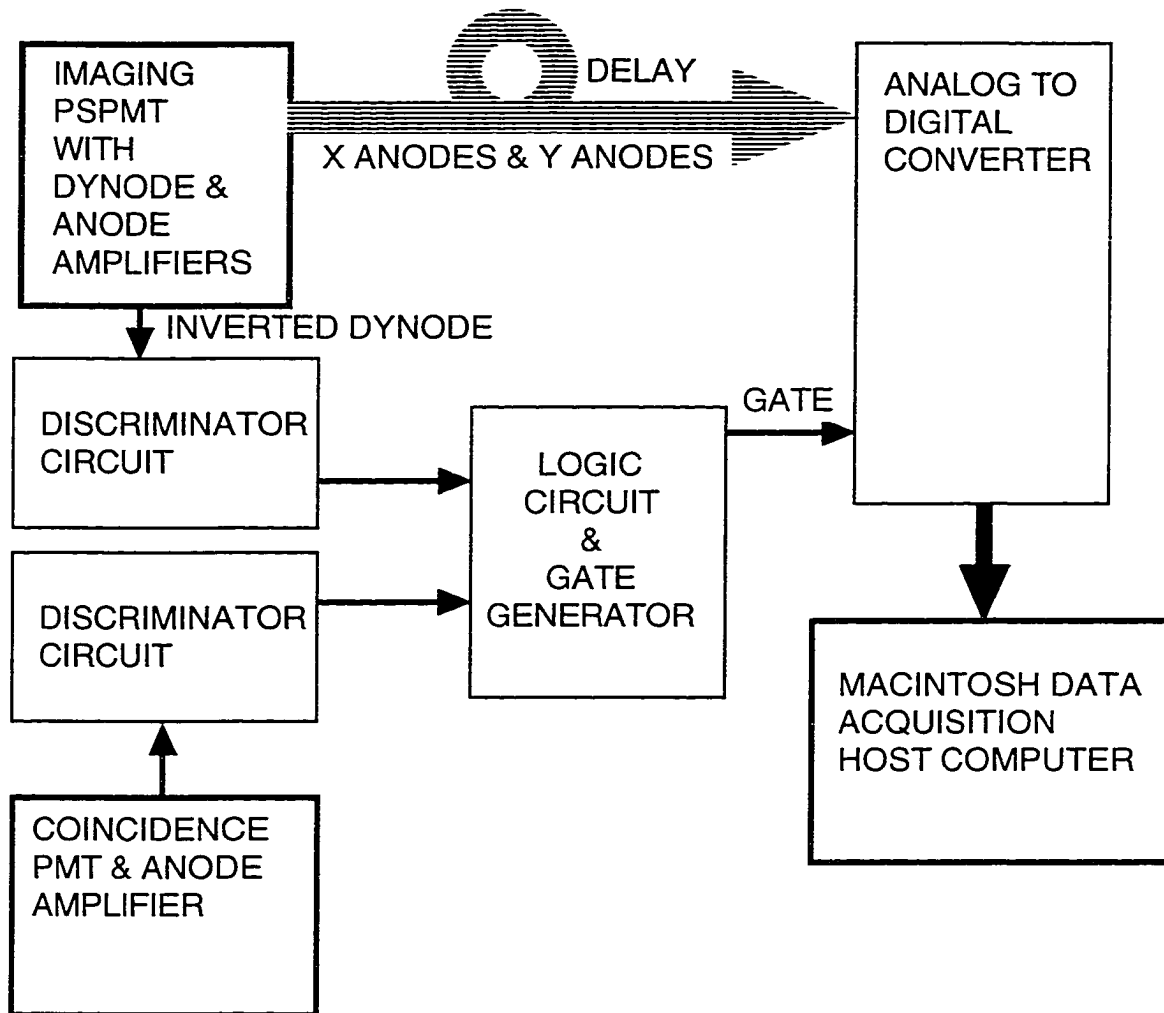
Digitization of the charge from the anode wires of the position sensitive photomultiplier tube is achieved by using CAMAC charge analog-to-digital converters (ADCs). The signals from the paired anode wires of the position sensitive photomultiplier tube were first amplified with LeCroy TRA1000 monolithic preamplifiers. The signal from

the last dynode of the position sensitive photomultiplier tube is inverted and passed through discriminator electronics to generate a timing signal. This signal is used to gate the analog-to-digital converters after it passes through a logic circuit. The purpose of the discriminator electronics is to restrict the generation of output gate pulses to dynode pulses that exceed an empirically determined threshold level. The threshold level was set high enough to exclude low energy noise, but low enough to allow the generation of gate pulses. This enabled the data acquisition process when the pulse height resulting from the scintillation event is above a desired threshold.

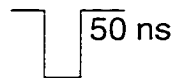
3.3.5 Coincident Radiation Detection

To detect the coincident radiation of ^{125}I , a standard photomultiplier tube attached to a crystal scintillator was positioned near the object to be imaged. The anode of the second photomultiplier tube used as the coincident detector was discriminated and passed to the logic unit. This signal was then logically multiplied with the discriminated dynode signal from the position sensitive photomultiplier tube to produce a gate for the coincidence mode. The resolving time of the coincidence circuit was 20 ns.

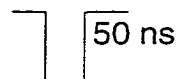
The output pulses from the dynode of the position sensitive photomultiplier tube and the anode of the coincident photomultiplier tube both had ~ 50 ns shaping and a timing jitter of ~ 10 ns. The total width of the gate was 150 ns for the YAP detector and was 1.0 μs for the CsI(Na) based detector. This difference is that the light pulse decay constant for YAP is 25 ns and is 630 ns for CsI(Na). A schematic representation of the electronics and timing diagram is shown in Figure 3.6. The detector system was always first operated in a non-coincident (single) mode, in which only the dynode signal from the position sensitive photomultiplier tube is used to generate the trigger for the ADC.



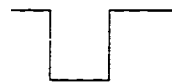
Discriminated dynode from PSPMT



Discriminated anode from PMT



output from coincidence unit



output from gate generator



Figure 3.6: Block diagram of the data acquisition electronics showing the path of the signals from the position sensitive photomultiplier tube (PSPMT) and the photomultiplier tube (PMT) used for coincidence detection.

3.4 Prototype YAP Based Gamma-ray Imaging System

The goal of the first phase of development of the detector system involved two tasks. The first task was to investigate the performance of Hamamatsu position sensitive photomultiplier tubes in imaging the gamma-ray and x-ray emissions of ^{125}I . In this stage of the project a YAP crystal scintillator mounted to the Hamamatsu R2386 position sensitive photomultiplier tube comprised the prototype detector system. This was put through rudimentary imaging performance studies to determine the detector properties by imaging sealed ^{125}I calibration sources. In addition, the concept of using the coincidence detection of the gamma-rays and x-rays of ^{125}I to generate low background images of ^{125}I was also tested. This was accomplished by using an additional standard photomultiplier tube with another scintillator as the coincident detector.

After tests were first performed using sealed ^{125}I calibration sources, animal studies were performed as the task of this phase. This was undertaken to evaluate the performance of the prototype system in the imaging of ^{125}I in a live animal. Imaging tests involving laboratory mice were done to gain insight into the optimization of the detector system and the experimental procedure for later animal studies.

3.4.1 R2486 Position Sensitive Photomultiplier Tube Based Detector

The R2486 position sensitive photomultiplier tube is 75 mm in diameter and has a standard alkali photocathode deposited on the entrance window resulting in a detection area of approximately 50 mm in diameter. The crystal scintillator, cerium doped (0.1%) yttrium aluminum Perovskite ($\text{YAlO}_3:\text{Ce}$) also known as YAP, has many properties that make it appropriate for imaging gamma- and x-rays resulting from the decay of ^{125}I . YAP has a decay time of 25 ns, is non-hygroscopic, and has a density of 5.37 g/cm^3 [93]. Tests

were performed with a 60 mm x 60 mm x 1 mm plate of YAP crystal scintillator using a 250 nanoCurie ^{125}I calibration source. The detector arrangement is shown in Figure 3.7.

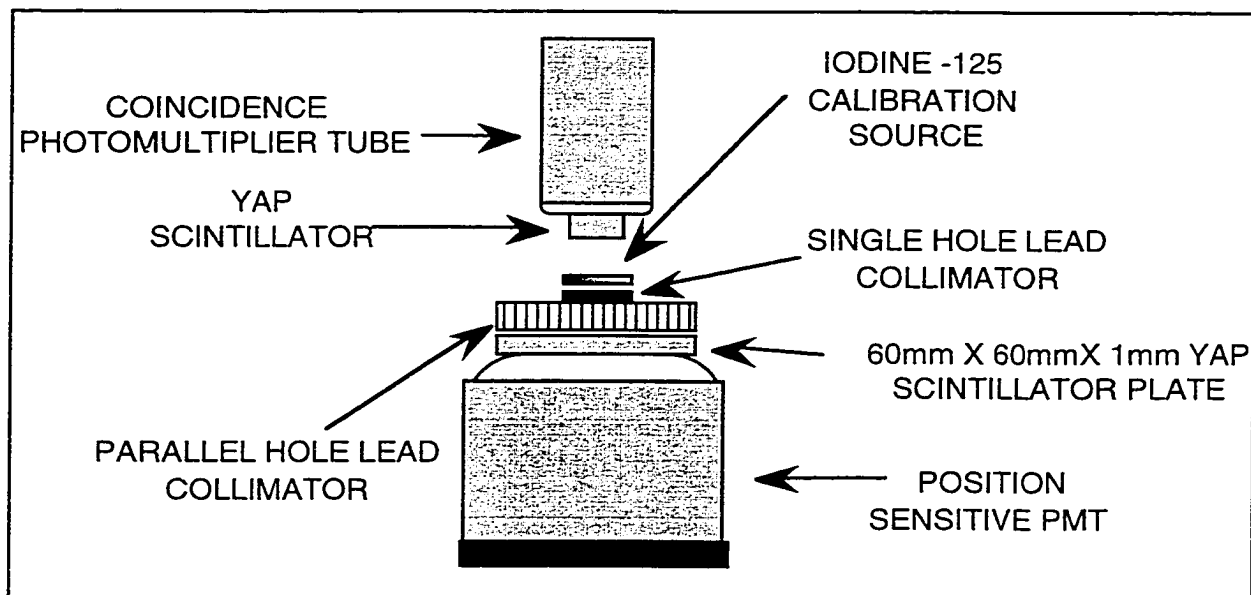


Figure 3.7: Detector arrangement for coincident detection of x-ray and gamma-ray emissions from ^{125}I . During the mouse study the ^{125}I source and single hole lead collimator were removed.

The plate of YAP was optically coupled to the position sensitive photomultiplier tube with optical grease that had an index of refraction of 1.465. The top of the scintillator was covered with Teflon tape and made light tight with black tape. A standard 2 inch diameter photomultiplier tube with a 3 cm x 3 cm x 1 cm YAP scintillator was used as the coincident detector.

3.4.1.1 Preliminary Detector Imaging Tests

The first imaging tests were performed using a sealed ^{125}I calibration source obtained from Isotope Products Laboratories [94]. An example of a raw uncorrected image of the source obtained using singles mode is shown in Figure 3.8. The total field of view

is a circular area 50 mm in diameter. The source size was constrained to a diameter of 2 mm by masking the source with a 3 mm thick lead mask comprised of a single 2 mm diameter hole. A 1 cm thick high resolution parallel hole lead collimator core that had 0.5 mm diameter size openings and 0.3 mm thick septa was used to image the masked ^{125}I calibration source.

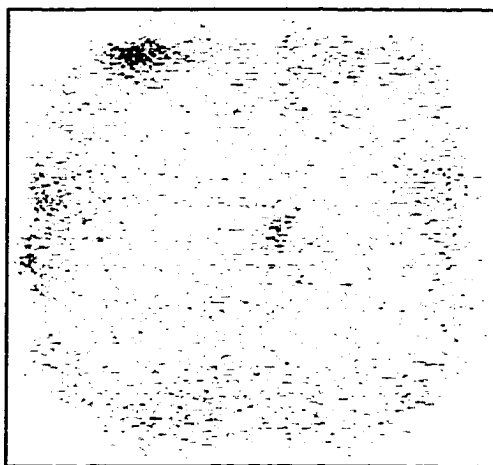


Figure 3.8: Raw image obtained in singles mode of an ^{125}I calibration source using 1 cm thick parallel hole lead collimator and a single 2 mm diameter hole in a 3 mm thick sheet of lead to form a source size of 2 mm in diameter. The field of view is 50 mm in diameter.

Figure 3.9 is an image obtained in coincidence with a 3 cm x 3 cm x 1 cm YAP crystal scintillator placed on the other side of the source, as shown above. In this configuration the coincident detector was placed in contact with the unmasked side of the calibration source. One can see that the background is considerably less than in the singles case. Both images were obtained by accumulating data for several hours. Energy acceptance windows were applied to accept only events in the range of energy for the decay of ^{125}I .

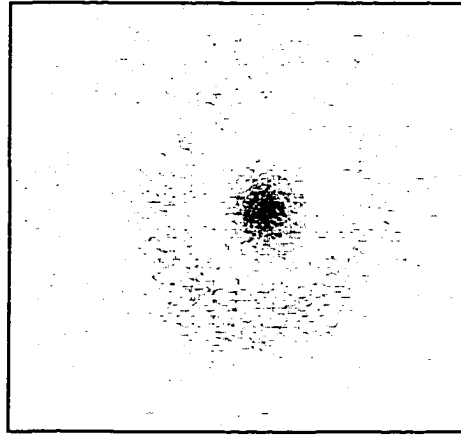


Figure 3.9: Raw image of the same ^{125}I calibration source as in Figure 3.8 obtained in coincidence mode.

The sum of the anode signals for each event was used to define a single energy window for the detector. No regional energy thresholds were set since the defined energy window was broad enough to accommodate the position dependent gain variation of the position sensitive photomultiplier tube.

3.4.1.2 Detector Properties

The intrinsic average position resolution across the active area of the position sensitive photomultiplier tube was measured to be 2.1 mm FWHM for 35 keV photons. This was obtained by imaging a ^{125}I sealed calibration source that was collimated with a 1 mm diameter pinhole in a 3 mm thick sheet of lead. A position resolution of 1.2 mm FWHM using the same technique with 122.5 keV gamma-rays from a ^{57}Co source was achieved. As mentioned before, the position resolution of the Hamamatsu R2486 position sensitive photomultiplier tube improves with number of photoelectrons [95]. This occurs because the higher number of photoelectrons generated results in a larger signal at the anode wires centered under the secondary electron cloud resulting in a improved signal to noise ratio. The intensity of the scintillation light pulse is proportional to the energy of the gamma-ray or x-ray photon. The gamma-ray and x-ray photons resulting from the decay

^{125}I (~35 keV) are relatively low energy compared to more commonly used nuclear medicine isotope such as $^{99\text{m}}\text{Tc}$ (~140 keV). Thus as expected a higher position resolution can be achieved with $^{99\text{m}}\text{Tc}$ than with ^{125}I .

The detector was equipped with a 1 cm thick high resolution parallel hole lead collimator. The collimator has 1.27 mm diameter apertures in a hexagonal pattern and the septa thickness is 0.15 mm. The system resolution with the collimator in place for a ^{125}I source placed 1.5 cm from the collimator was determined to be 3.5 mm.

The sensitivity of the detector system operated without the coincident detector (i.e., in singles mode) for a source placed in the center of the detector was measured to be 366 cpm/ μCi . In coincidence mode, with the coincident detector and imaging detector 2.5 cm apart, the sensitivity was measured to be 4.3 cpm/ μCi . The random coincidence rate in this arrangement with only background radiation was only 1.6 cpm.

The energy acceptance window was set to include the x-rays and gamma-rays emitted by ^{125}I . An example of a ^{125}I pulse height spectrum, taken in coincidence mode is shown in Figure 3.10.

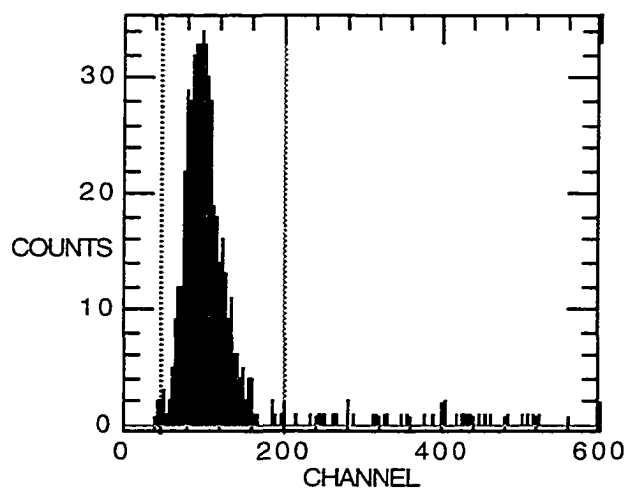


Figure 3.10: ^{125}I pulse height (energy) spectrum generated from the sum of the anode signals using coincidence mode of detection. Dotted lines indicate the energy acceptance window which includes energies from approximately 20 to 50 keV.

The peak, centered near channel 100, is the superposition of the 35 keV gamma-ray and the 27.2, 27.5, and 31 keV x-rays resulting from the decay of ^{125}I . The energy acceptance window is indicated by the dotted lines.

3.4.2 Detector Performance During Animal Laboratory Tests

The prototype detector performance in an animal study was evaluated in tests involving the uptake of iodine in the Prairie Deermouse (*Peromyscus maniculatus*) and melatonin uptake in the Swiss mouse (*Mus musculus*). For the first case, ^{125}I was intraperitoneally injected into the mouse and the iodine accumulation in the thyroid was followed. The second study involved the imaging of the biodistribution of tail vein injected melatonin labeled with ^{125}I . All animals were fed *ad lib* on a standard laboratory rat, hamster and mouse diet using Agway Pro Lab 2000 feed. These animal studies were instrumental in evaluating the experimental detector setup.

3.4.2.1 Animal Studies with ^{125}I

An intraperitoneal injection (IP) of ^{125}I into a 15 gm female *Peromyscus maniculatus* was performed following anesthetization with IP injection of 4% chloral hydrate. The ^{125}I was obtained from DuPont-NEN, Inc. in the form of NaI in 10^{-5} M NaOH. The sample was diluted with sterile water to a concentration of $10\ \mu\text{Ci}/\mu\text{L}$ and $2\ \mu\text{L}$ ($20\ \mu\text{Ci}$ of ^{125}I) was injected.

A time record of the uptake of the iodine from the injection site to the eventual concentration into the thyroid gland was imaged over two days. Figure 3.11 depicts an image obtained in coincidence acquisition mode representing a collection time of 50 minutes obtained beginning at 8 hours post injection of ^{125}I . The detectors were placed 1.5 cm apart.

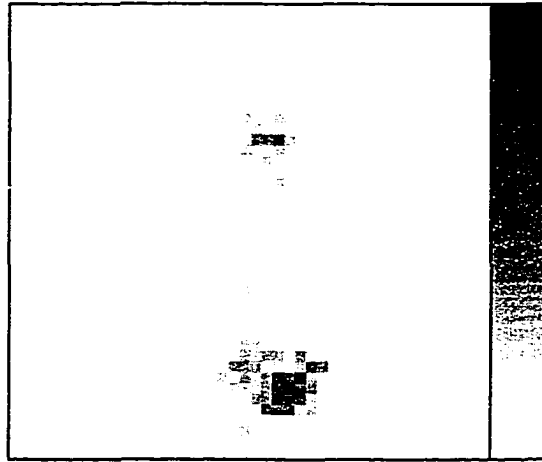


Figure 3.11: Raw image obtained using coincidence data acquisition mode of the distribution of ^{125}I in mouse 8 hours post injection. The lower hot spot corresponds to the injection site. Some iodine accumulation is seen in the neck region, the location of the thyroid gland. The range of pixel values in the image, indicated by the gray scale, is from 0 to 22 counts. The field of view is 50 mm in diameter.

In the Figure 3.11 one sees iodine concentration in the region of the injection site and some accumulation in the thyroid. The image count rate was approximately 20 image counts/minute, which is the rate of coincidence events satisfying the energy window. The ^{125}I image obtained was processed with NIH Image software [96] and then overlaid onto a digital photograph of the actual experimental mouse as shown in Figure 3.12.

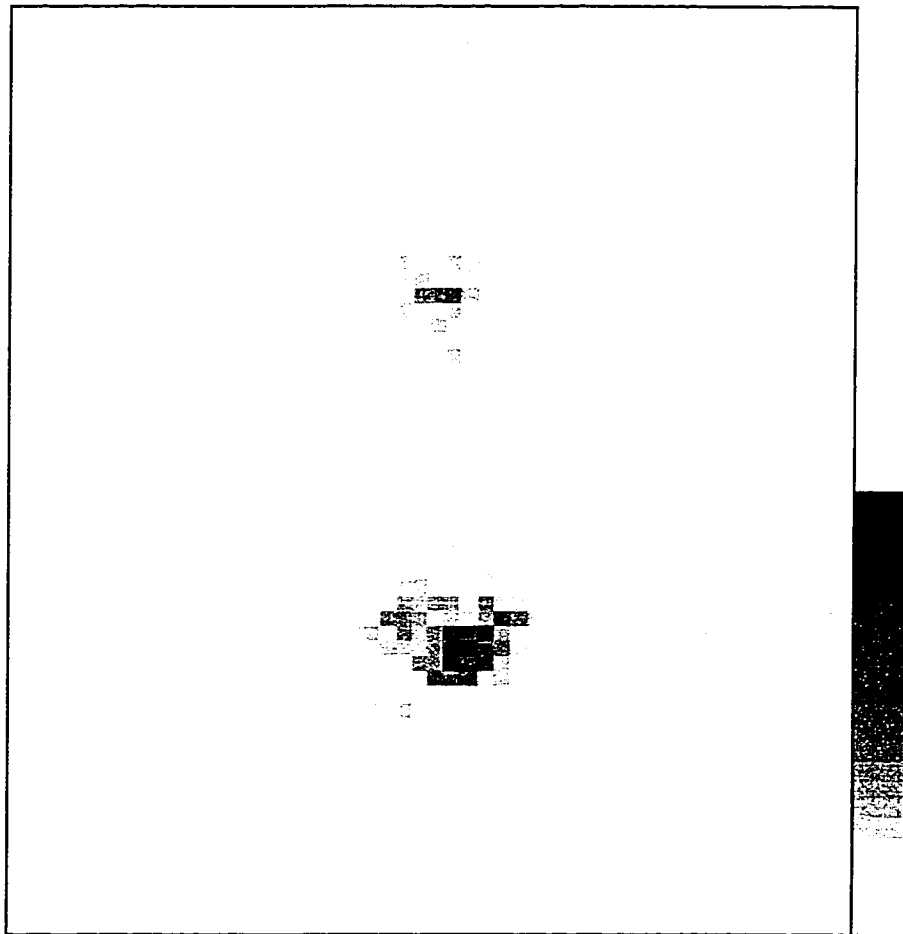


Figure 3.12: Image data from Figure 3.11 scaled and then overlaid onto a photograph of the mouse. The range of pixel values in the image and indicated by the gray scale is from 0 to 22 counts.

The mouse was allowed to recover from the anesthesia and was given food and water *ad lib*. Another image was obtained 24 hours post injection and the thyroid gland was found to contain the majority of the radioactivity at 23 image counts/minute (Figure 3.13). The total dose still in the live mouse after 24 hours post injection measured from the image was estimated at 5.3 μCi or 27% of the original dose. The experimental results provide an initial baseline example of the nature of the distribution of injected iodine and the eventual accumulation in the thyroid gland of the mouse. It is clear that soon after injection the ^{125}I becomes distributed throughout the mouse. By 8 hours after injection concentration

begins to appear in the thyroid region and by 24 hours the ^{125}I is cleared from the mouse showing only an accumulation in the thyroid. These results are then be compared to results from the injection of ^{125}I -labeled melatonin into a mouse which was the next phase of the mouse study.

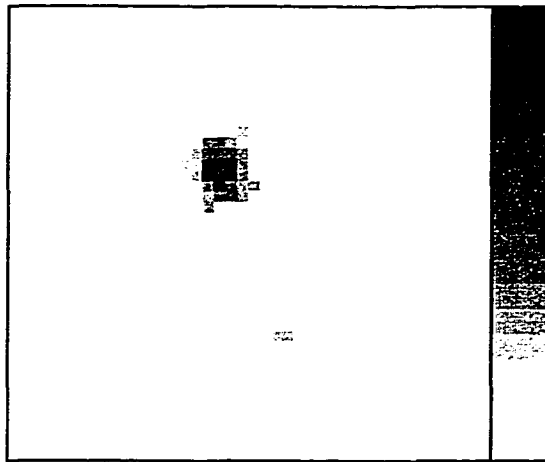


Figure 3.13: Raw image obtained in coincidence mode of the distribution of ^{125}I in the mouse 24 hours post injection indicating maximum concentration of most of the iodine in the thyroid gland. The range of pixel values in the image and indicated by the gray scale is from 0 to 17 counts.

3.4.2.2 Animal Studies with ^{125}I -labeled Melatonin

One of the goals of this project was to develop an imaging system which could be used to study neurological processes in the brain of a live mouse by way of various neural specific radioiodinated ligands. A major challenge is to test various ligand delivery techniques that can get labeled molecules into the brain. This is very difficult because of inherent physiology (blood-brain barrier) that keeps the brain partially isolated from the body's general circulatory system. To test the ability of the detector to image the accumulation of a ^{125}I -labeled ligand in the mouse brain, ^{125}I labeled melatonin was injected into a live mouse. Melatonin is known to pass through the blood-brain barrier and to have binding sites in the brain as well as in other organs of an adult mouse [97]. A dose of

approximately $5\ \mu\text{Ci}$ ^{125}I -labeled melatonin (Amersham Inc.[98]) in $5\ \mu\text{l}$ was injected into the tail vein of a 20 gm male Swiss mouse that had been anesthetized with pentobarbital. Imaging was started 12 minutes after injection and a series of images were obtained approximately every 8 minutes, and an image representing an acquisition time of 8 minutes. Most images were obtained using the coincidence acquisition mode. For comparison, several images were also obtained with the coincidence mode disabled to investigate the effect of lost statistics because of the more restrictive coincidence mode of image acquisition.

Figure 3.14 depicts an image obtained from the sum of all the images taken with coincidence radiation. The image was made from a composite of images totaling 72 minutes acquisition time and a total of 1375 imaging events.

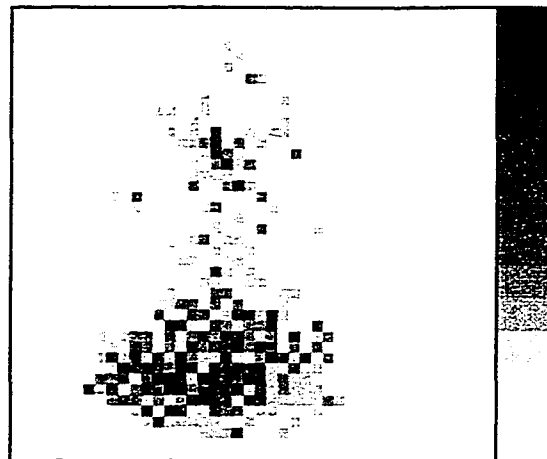


Figure 3.14: Image of ^{125}I labeled melatonin distribution in mouse using coincidence radiation detection. The head of the mouse is towards the top of the image. Only events falling in the energy window of 50 to 200 channels were used to form the image. The range of pixel values in the image and indicated by the gray scale is from 0 to 8 counts.

In Figure 3.15 the data from Figure 3.14 has been scaled and superimposes onto a photograph of a mouse to indicate the approximate distribution of the melatonin in the mouse. Two regions of interest were chosen for comparison to determine if there is an enhanced uptake of melatonin in the head region. The first region included the head area

and another of the same size located in the chest (abdomen/thorax). The plot shown in Figure 3.15 indicates the time change of the ratio of melatonin concentration in the head compared to the chest.

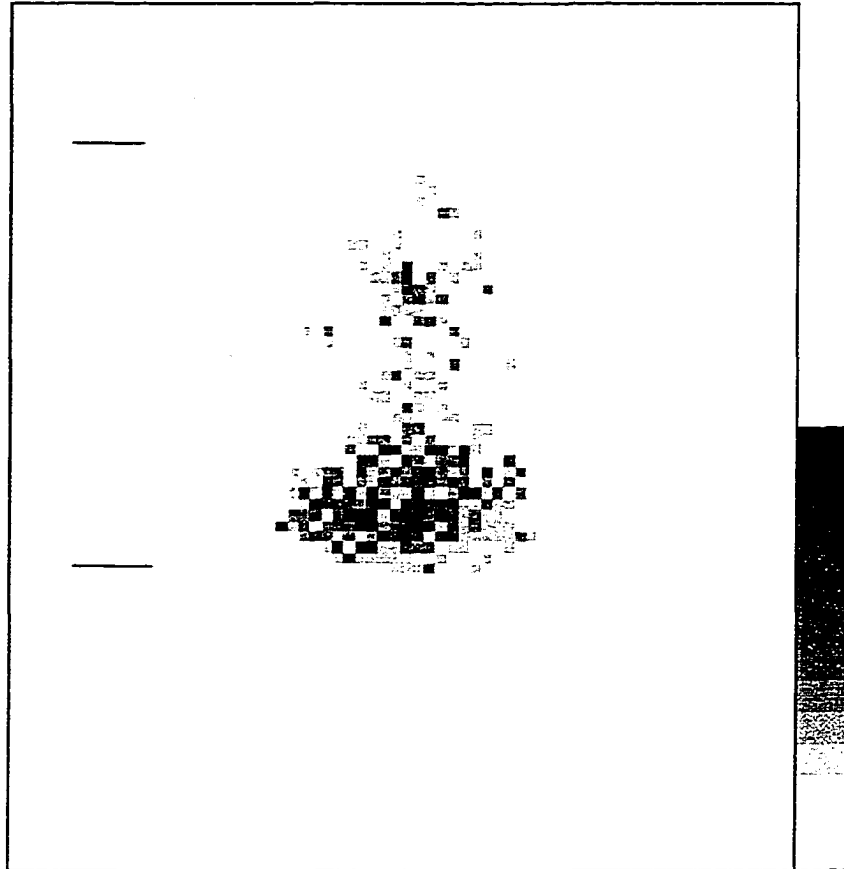


Figure 3.15: Illustration with data from Figure 3.14 on top of a photograph of a different mouse to indicate the approximate location of the uptake of melatonin. The field of view of the detector is indicated by the two horizontal lines. The range of pixel values in the image and indicated by the gray scale is from 0 to 8 counts.

The results suggest that maximum association ^{125}I -labeled melatonin in the brain occurred very soon after injection and followed by possible saturation of the melatonin receptors. The subsequent disappearance from the head to other areas is indicated by the gradual accumulation of signal in the abdominal/thorax. In Figure 3.16 the data marked

“image total” indicates the change in counts in the total image at different time intervals. At each time interval (~ 8 minutes) the image was cleared and a new one acquired.

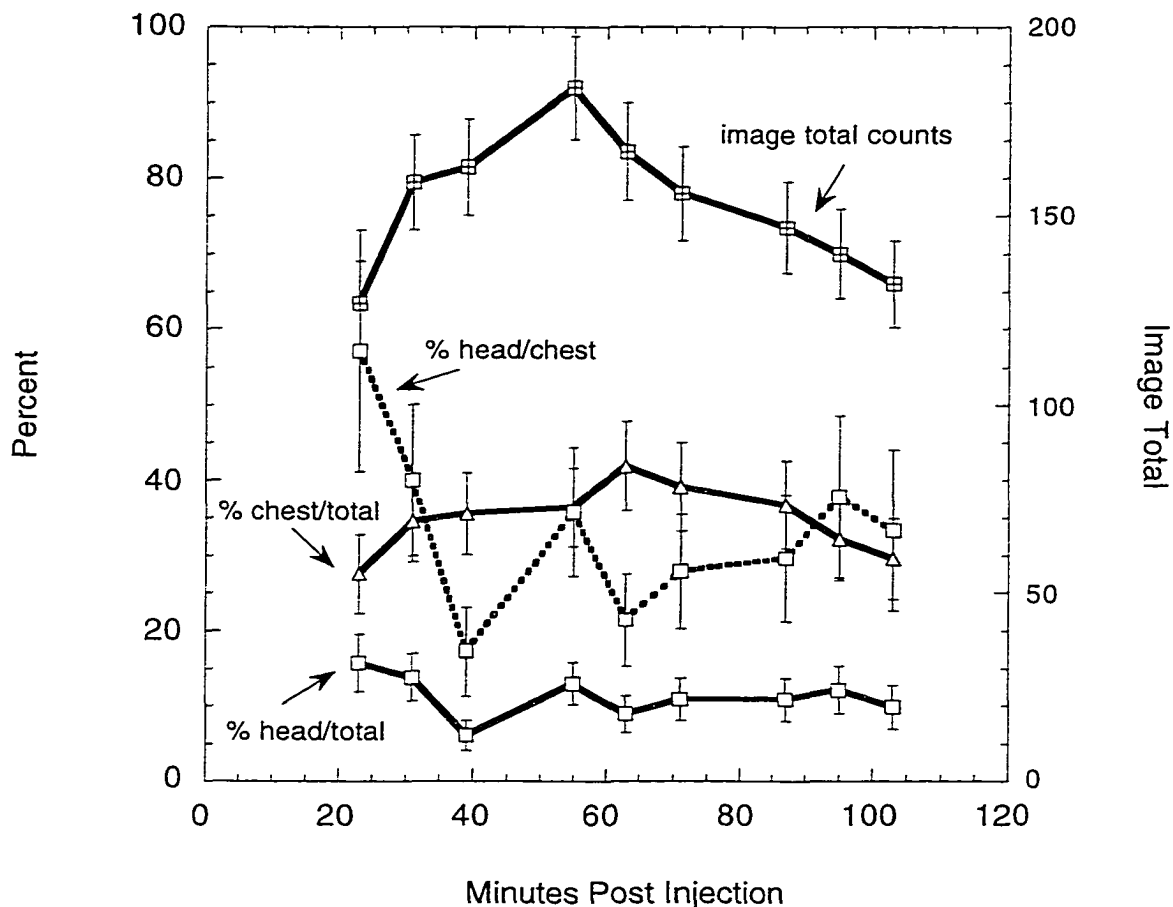


Figure 3.16: Time change of melatonin in the head compared to the chest. Plotted are the ratios of signal in head/chest, head/total and chest/total expressed in percent. The “image total” plot is in total counts. Error bars are plus and minus one sigma (σ) determined by propagating the errors using Poisson statistics ($\sigma^2 = \text{number of counts}$) [99].

After imaging was complete the mouse was sacrificed and the brain was fixed, sectioned, and placed in contact with autoradiographic film. After 52 days the autoradiograms were developed and examined. Several 8 micron sections in the region of the brain (tissues of the median eminence as well as diffusely present within the ventricles) showed significant uptake of the melatonin (data not shown) confirming that there are binding sites for melatonin in the brain and that the detector system did measure accumulation in the brain.

3.4.3 Discussion of the First Prototype Results

The initial results of imaging ^{125}I with the prototype detector demonstrated the detector system's ability to successfully image ^{125}I . It was determined that it was possible to use position sensitive photomultiplier tubes to image the low energy gamma and x-ray emissions of ^{125}I . Shown also was that the coincident detection of the gamma-ray and x-ray emission of the decay ^{125}I could be a useful option to image low uptakes of ^{125}I . In addition, it was clear that this type of detector system could be improved with higher resolution, larger and more sensitive detectors, optimized geometry, and custom designed collimators. The Hamamatsu R2486 position sensitive photomultiplier tube, has a limited active area (~50 mm diameter) such that the entire mouse could not be imaged at once. Also, this position sensitive photomultiplier exhibits a non-uniform response across its active area which leads to image distortion at the edges, further limiting its useful field of view. The next phase of the project involved the building of a new detector system which used the five inch diameter Hamamatsu R3292 position sensitive photomultiplier tube and a 110 mm in diameter CsI(Na) scintillating crystal array.

3.5 Gamma-Ray Imaging System Based a on CsI(Na)

Crystal Array

The goal of the second phase of the project was to improve the spatial resolution in order to obtain a position resolution less than 3 mm FWHM and to utilize a larger active area position sensitive photomultiplier tube so that a whole mouse could be imaged at once. This phase of development of the detector system involved three tasks. The first task was to investigate the performance of the 125 mm diameter Hamamatsu position sensitive photomultiplier tube (R3292) in imaging the gamma-ray and x-ray emissions of ^{125}I when

coupled to a CsI(Na) scintillating crystal array. The second task was to evaluate the imaging capabilities of the array and configure the computer controlled data acquisition system to perform real-time image processing based on mapping the individual response of each crystal element into a processed image. The coincidence detection of the gamma-rays and x-rays of ^{125}I to generate low background images of ^{125}I was also upgraded to accommodate a larger imaging area. The third task was to test the performance of the data acquisition system and computer controlled mapping system in a real setting given the greater demands placed on the system to perform additional processing. A repeat of the ^{125}I labeled melatonin study was performed to compare to the previous imaging test performed with the YAP based detector.

3.5.1 R3292 Position Sensitive Photomultiplier Tube Based Detector

To improve spatial resolution with position sensitive photomultiplier tubes, a higher intrinsic resolution from the photon detector was needed. Therefore, larger scintillation light signals would need to be realized from the interaction of the gamma-ray and x-ray photons from ^{125}I . After studying various commercially available scintillator crystals the crystal scintillator CsI(Na) was chosen. CsI(Na) has approximately 60% better light yield than YAP and is about half the price. This is particularly important in the imaging of 35 keV photons from the decay of ^{125}I . This crystal is also able to be cut into an array comprised of small crystal elements to construct a “pixel” array-based detector.

3.5.1.1 Scintillating Crystal Arrays

The array-based detector was chosen to improve the spatial resolution and to facilitate the removal of the image distortion common with the Hamamatsu position sensitive photomultiplier tubes. Barone et al. [39] have reported improved spatial

resolution with imaging detectors comprised of scintillators attached to position sensitive photomultiplier tubes through the use of arrays of scintillating crystal elements instead of a planar scintillator. The authors report that the scintillating crystal pixels act to direct the scintillation light onto the photocathode with much less light spread than would occur with a planar scintillator. This has the effect of confining the secondary electron cloud to a much tighter distribution which results in improved spatial resolution. The authors report imaging 140 keV gamma-ray sources with a spatial resolution of 0.7 mm FWHM using YAP scintillating crystal arrays which had element dimensions of 0.6 mm x 0.6 mm x 7.0 mm.

In order to increase detection sensitivity in the coincidence detection mode the detection area of both the imaging and the coincident detector was increased. In addition, collimators were designed to be optimized for ^{125}I imaging with a CsI(Na) crystal array. The low energy radiation of ^{125}I presents the opportunity to use materials, other than lead, for the collimators.

In developing a CsI(Na) based detector, first a system was tested that used an array 110 mm in diameter where each crystal element is 2.0 mm x 2.0 mm in area and 3 mm thick. The array was directly coupled to the five inch diameter Hamamatsu R3292 position sensitive photomultiplier tube. The CsI(Na) array was custom built by Hilger, Ltd. [100]. The thickness of 3.0 mm was chosen to allow for the efficient collection and transmission of the scintillator light to the photocathode. Most of the 35 keV photons of the decay of ^{125}I get stopped within the first 1 mm of CsI(Na).

Truman et al. [101], have demonstrated that arrays of a similar the crystal scintillator CsI(Tl) can be efficiently readout with the Hamamatsu position sensitive photomultiplier tubes. As mentioned earlier, the array based detector allows removal of the image distortion and facilitates correction of the non-uniformity of response common to the Hamamatsu position sensitive photomultiplier tubes.

3.5.1.2 Hamamatsu R3292 Position Sensitive Photomultiplier Tube

The Hamamatsu R3292 125 mm diameter position sensitive photomultiplier tube has 28 x 28 crossed anode wires. Again, as was done in the case using the model R2486 position sensitive photomultiplier tube, the number of individual channels read out was reduced by connecting anode wires in groups of two thus reducing the number of channels to instrument by a factor of two (see Figure 3.17)

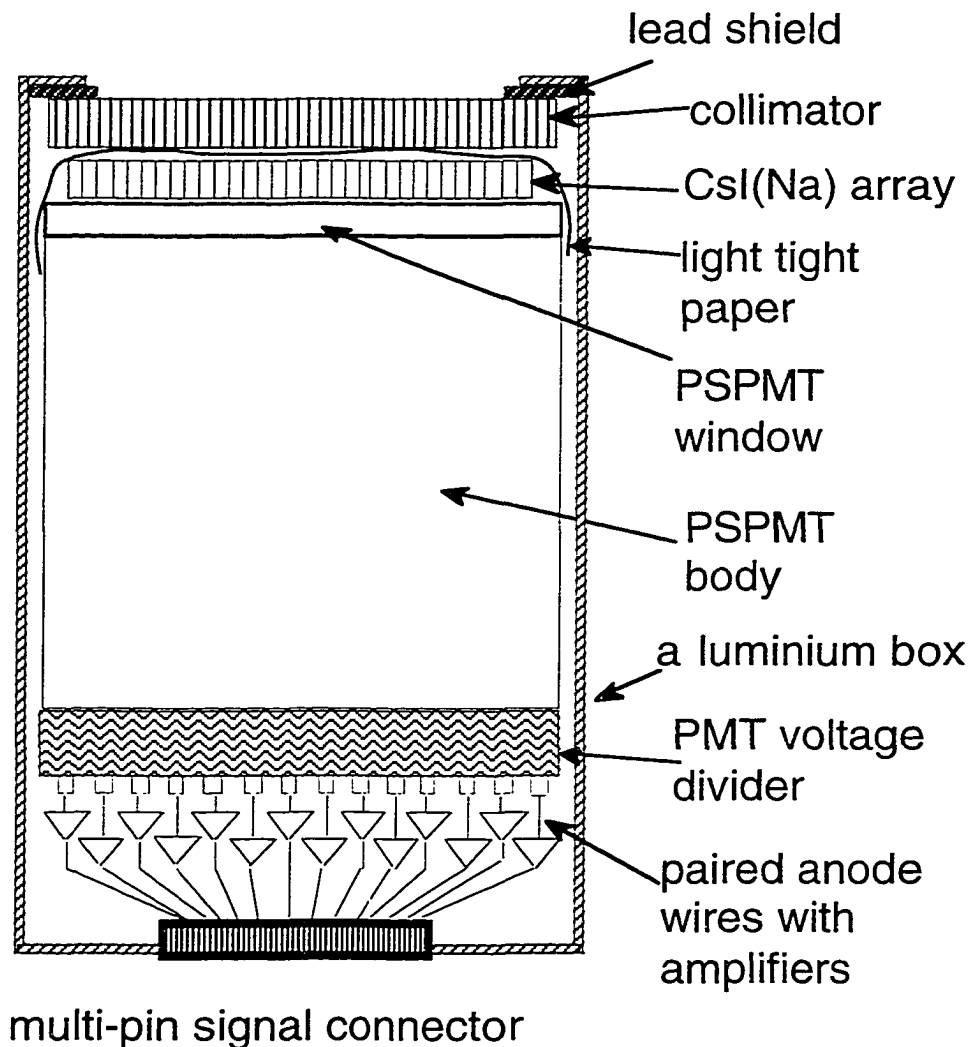


Figure 3.17: Cross sectional view of the 125 mm diameter R3292 position sensitive photomultiplier tube coupled to the CsI(Na) crystal array.

The original 28x+28y anode wire readout was reduced to 14x+14y wire groups. All anode sector signals were amplified by a factor of ten in low noise LeCroy TRA 1000 amplifiers and delayed by 50 nanoseconds before entering 28 individual ADC channels.

A conventional 125 mm diameter photomultiplier with a NaI(Tl) crystal made by Scionix Holland B.V. [102] was used as the coincident detector. The NaI(Tl) crystal is 121 mm in diameter, 3 mm thick with a 1 mm quartz window and a 0.3 mm aluminum entrance window. As was the case with the YAP based detector, this detector was equipped with a 1 cm thick high resolution parallel hole lead collimator. The collimator has 1.27 mm diameter apertures in an hexagonal pattern and the septa thickness is 0.15 mm.

3.5.2 CsI(Na) Scintillating Crystal Array Performance and Mapping

The individual 2 mm x 2 mm CsI(Na) crystal elements are resolved using the same truncated center of gravity technique discussed earlier. The real-time data processing developed and implemented using the Kmax data acquisition system treats the output of each crystal region individually to correct for crystal-to-crystal scintillation output variations as well as the local position sensitive photomultiplier tube gain variations. The procedure involved the generation of calibration look-up tables which were obtained by obtaining flood images. The look-up tables were then used by the data acquisition control software to perform the mapping.

3.5.2.1 CsI(Na) Scintillating Crystal Array Performance

A flood image was produced by using a ^{125}I point source placed about 10 cm above the CsI(Na) crystal array (without a collimator installed) to flood the entire crystal array. Figure 3.18 illustrates an example of a flood image and a projection of the center row of crystals. The individual crystal-pixels show variations in light output because of the

position dependent variation in sensitivity of the position sensitive photomultiplier. In addition, one can see the image distortion resulting from the non-uniformity of response of the position sensitive photomultiplier tube. This is particularly evident near the outer edge of the active area.

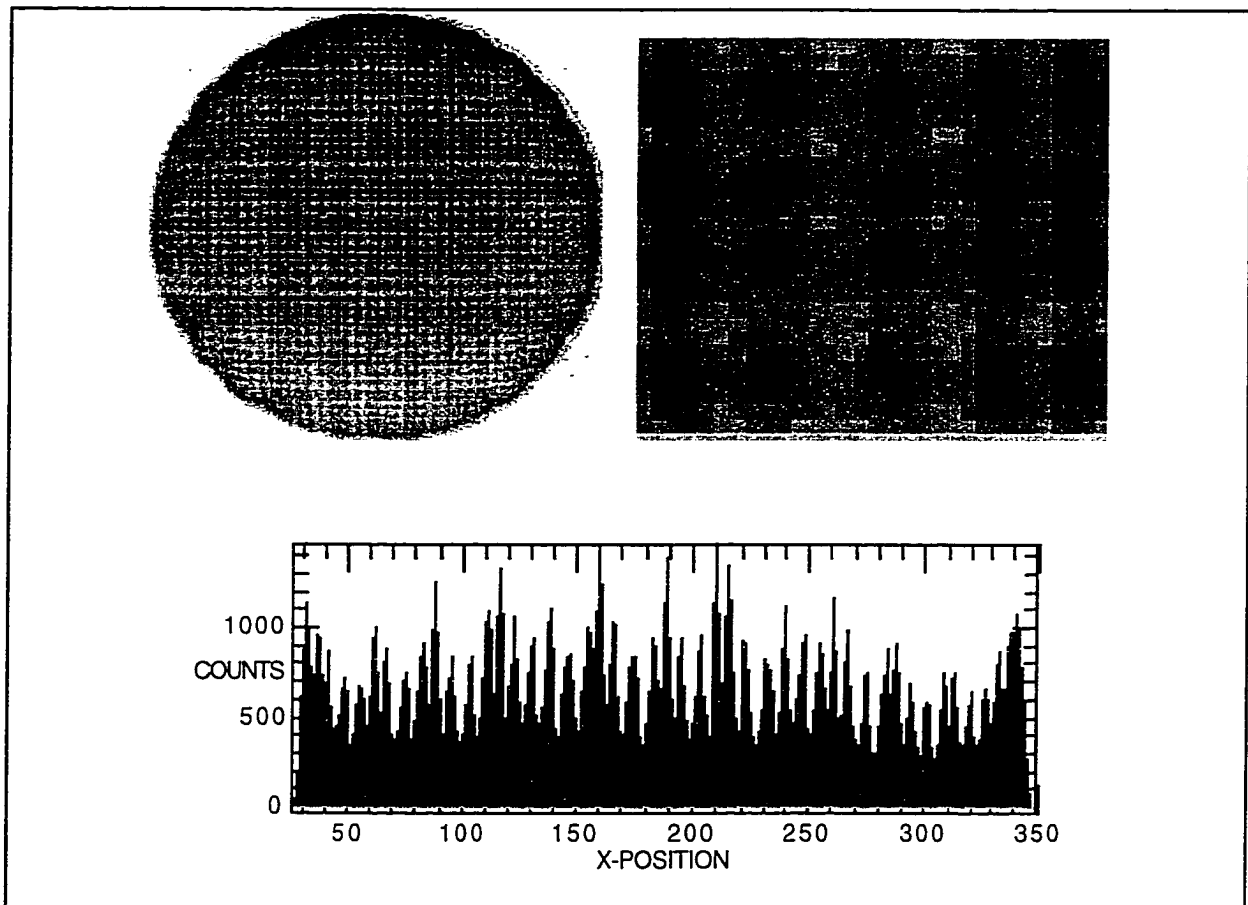


Figure 3.18. The full raw flood image of the crystal array is shown in the top left portion of this figure. An enlargement of the central region of the image is in the top right. The histogram in the lower half of the figure is a projection of a single row of crystals. The data was taken in a coincidence mode. Over 95% of the crystals are well resolved.

Individual crystals are easily resolved as can be seen in the ^{125}I image shown in the right half of Figure 3.18. The coincident detector was placed in contact with the ^{125}I source. The lower part of Figure 3.18 shows a projection through one row of crystals

illustrating the isolated image of each of the 2 mm x 2 mm individual crystals. The pulse height spectrum for this image is shown in Figure 3.19. This histogram is generated by summing the individual anode outputs from both axes.

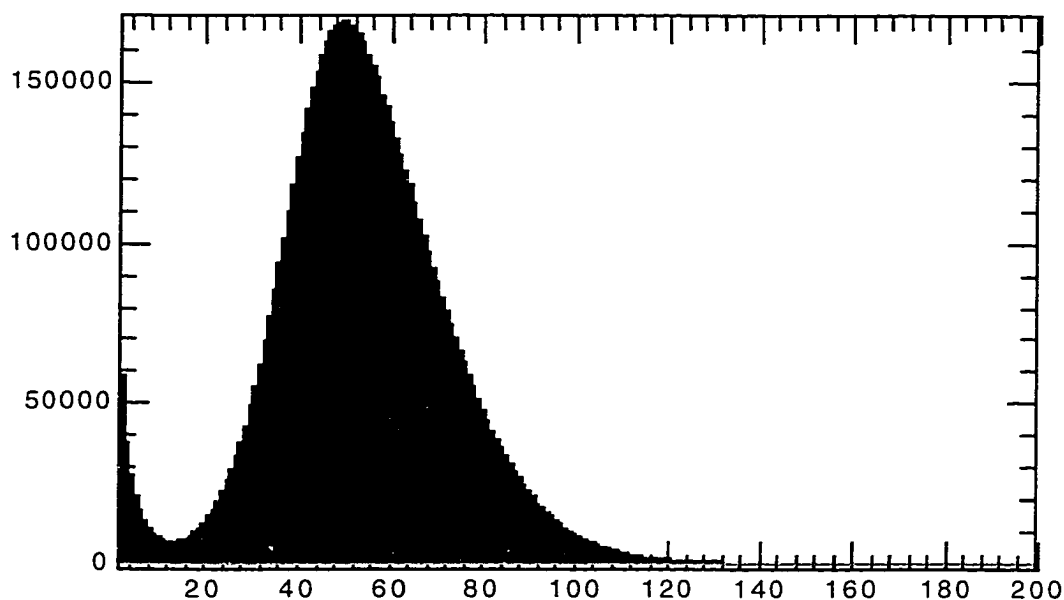


Figure 3.19: Pulse height spectrum (arbitrary units) for the image taken in coincidence mode.

3.5.2.2 Crystal Array Mapping

Raw images obtained with the position sensitive photomultiplier tube exhibit distorted crystal positions because of spatial non-uniformity of response in the position sensitive photomultiplier tube. Distortion correction is achieved by mapping the data identified to belong to a particular crystal into that crystal's appropriate pixel in the corrected image. This is possible since the relative position of each crystal is known and the crystal locations can be identified in the raw image. Figure 3.20 indicates the points that have been determined to mark individual crystal region corners in the raw image. By

using a flood image, as in Figure 3.18, four dots, one at each corner are placed at each corner of the region denoting the location of each crystal element.

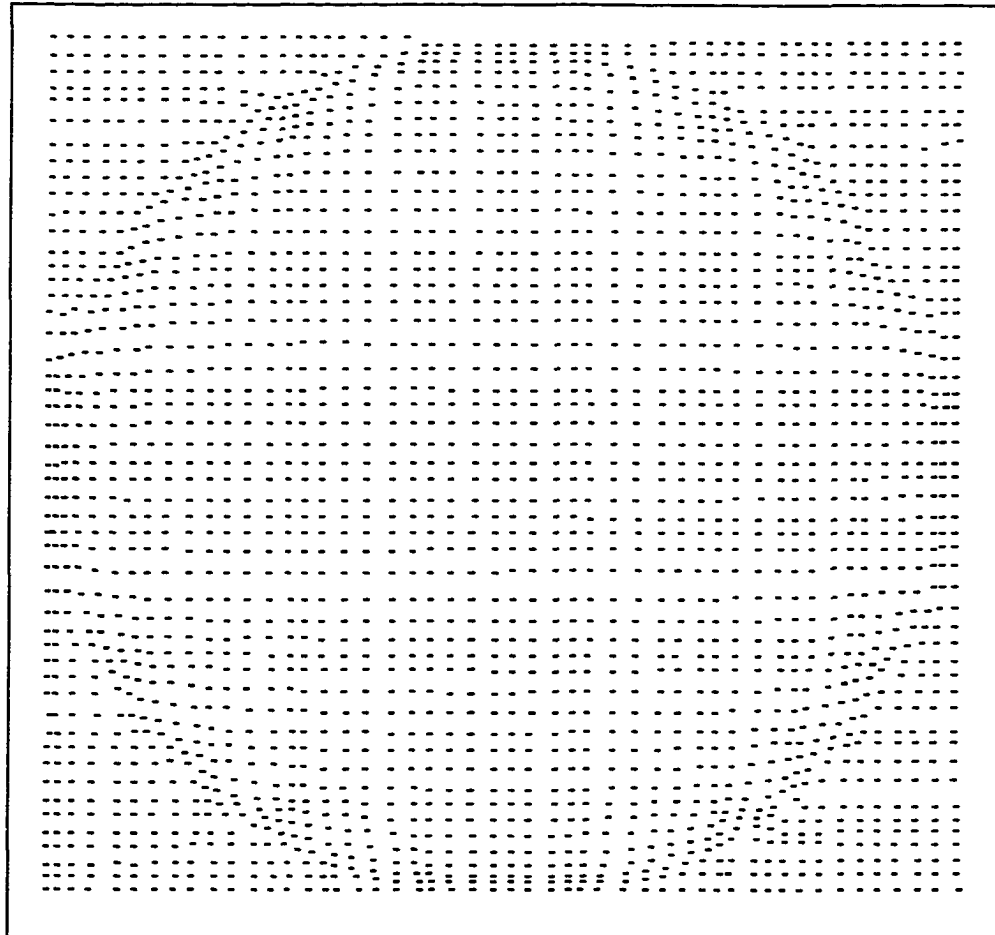


Figure 3.20: Map of crystal regions. Each crystal region is marked by four dots, one at each corner. “False” filler crystals were also marked at the four corners to simplify the real time look-up table computer algorithm.

These dots are then read by a computer program to generate a look-up table that defines the regions identified for each crystal element. It is this look-up table which is used by the real time data acquisition program to perform the crystal mapping on an event by event basis. Since the crystal array is a circle formed from an array of square crystal elements, “false” filler crystals were marked at the four corners to simplify the real time look-up table computer algorithm.

3.5.3 Detector Performance Imaging ^{125}I Labeled Melatonin in a Live Mouse

The performance of real-time computer controlled crystal mapping system was next tested under actual animal imaging conditions. With the lead collimator placed in front of the CsI(Na) array planar images were obtained of the distribution of ^{125}I in the body of the mouse. The imaging ability of the detector was tested by attempting to image ^{125}I -labeled melatonin that was concentrated in various sites in a live mouse.

A dose of approximately 12 μCi (0.1 ml) of ^{125}I -labeled melatonin obtained from Amersham Pharmacia Biotech Inc. [98] was injected into a tail vein of a 23 gm male *Peromyscus maniculatus* mouse anesthetized with 0.35 ml of 4% chloral hydrate. Imaging was started 40 minutes after injection of the ^{125}I -labeled melatonin. Examples of a raw and a corrected image are shown in Figure 3.21 and Figure 3.22 respectively, which were acquired in singles mode with the usual background signal observed.

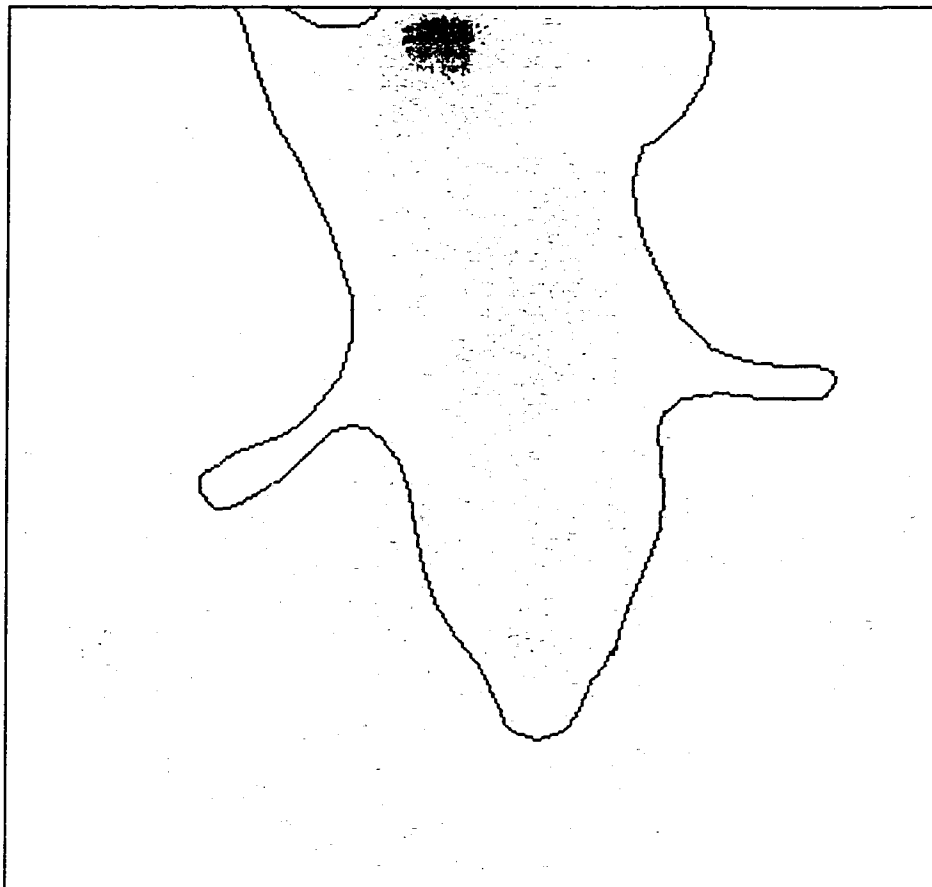


Figure 3.21: Raw image obtained using the CsI(Na) array. In this image it is possible to see individual crystals of the array. The crystals are particularly apparent in the area of the hot spot at the top of the image which corresponds to the mouse's bladder. The mouse was positioned with its head pointing downward as indicated by an outline of the mouse drawn over the image.

The imaging information contained in Figure 3.21 is sorted and mapped on a crystal by crystal basis for the appropriate location and individual energy window. The results of this real-time processing for position and energy are shown in Figure 3.22. An energy window of 20% placed around the peak of the energy response was used on each crystal element to form the image.

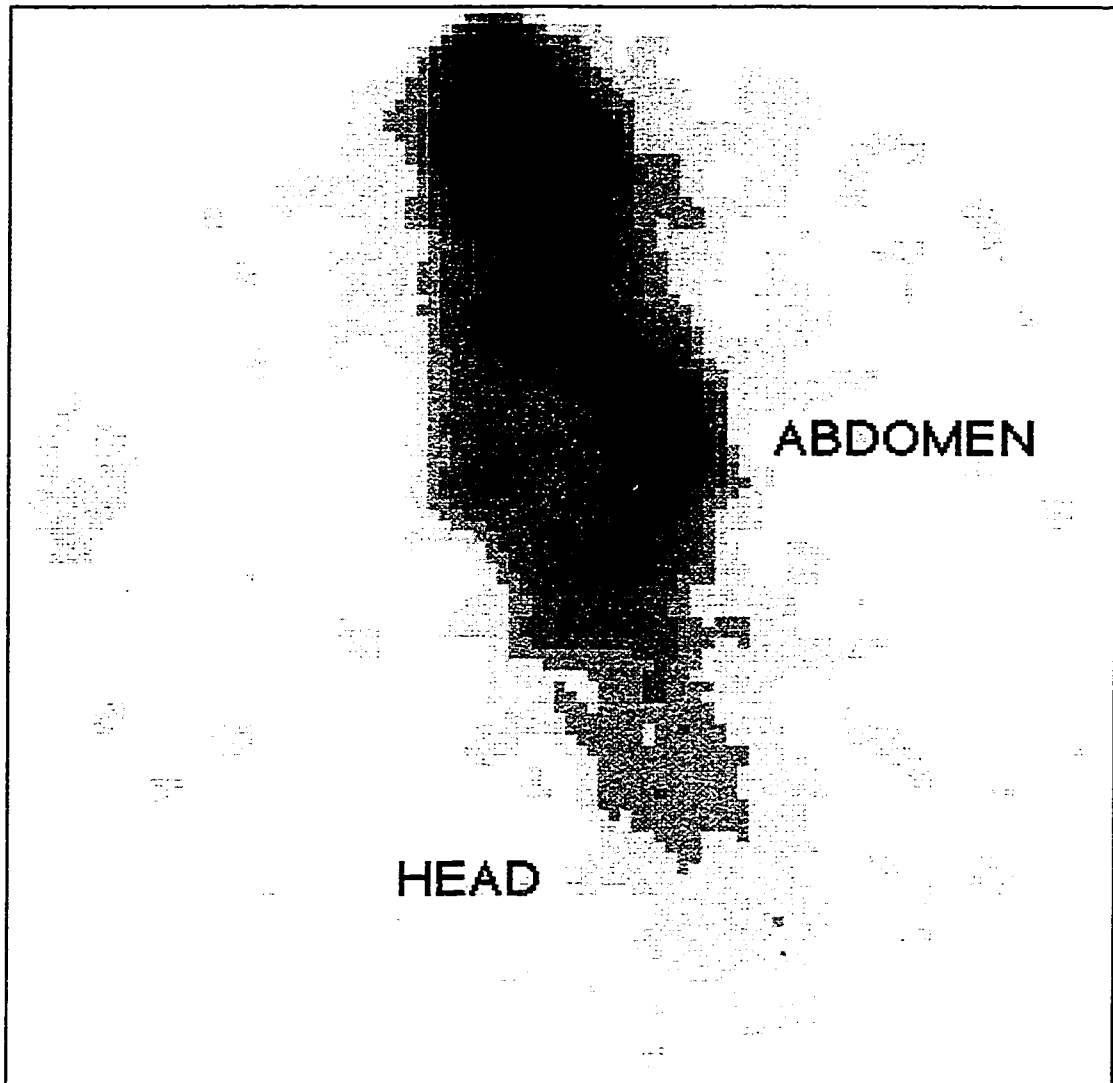


Figure 3.22: This is the corrected image obtained using the data and orientation as shown in Figure 3.21 and applying the crystal boundary information shown in Figure 3.17. The gray scale has been compressed to show that small accumulation is showing up in the head region

The image shows the melatonin distribution in the mouse. Total image acquisition time was 20 minutes. The results obtained were similar to those obtained with the YAP detector, however this time nearly the entire animal was imaged. The computer controlled mapping of the response from the individual crystal to a corrected image performed adequately in real-time under realistic imaging conditions.

3.5.4 Discussion of the CsI(Na) Array Based Results

The initial results in imaging ^{125}I with the CsI(Na) based array detector demonstrated that a CsI(Na) array performs well when coupled to the Hamamatsu 3292 position sensitive photomultiplier tube. It was clear that this type of detector system could be improved further with the use of a CsI(Na) array with smaller sized elements and a custom designed collimator. With Hamamatsu R3292 position sensitive photomultiplier tube the entire mouse could be imaged at once. This position sensitive photomultiplier exhibits a non-uniform response across its active area which leads to image distortion at the edges. This however is corrected by remapping the response from each individual crystal to generate an undistorted image.

The system resolution with this array and the lead collimator was ~ 4.0 mm FWHM for a source distance of 1.5 cm. The next phase of the project involved the building of a new detector system which again used the five inch diameter Hamamatsu R3292 position sensitive photomultiplier tube and a 110 mm in diameter CsI(Na) scintillating crystal array but this time with 1 mm x 1 mm sized elements and a specially designed high resolution parallel hole collimator.

3.6 Gamma-Ray Imaging System Based on an Array with 1.0 mm x 1.0 mm Elements

The goal of the third phase of the detector development project was to improve further the spatial resolution in order to obtain a position resolution approaching 1 mm FWHM and to test all aspects of the detector system (coincidence imaging, spatial resolution, and sensitivity) prior to using the system in an actual animal study. This phase of the project involved three tasks. The first task was to investigate the performance of the 125 mm diameter Hamamatsu R3292 position sensitive photomultiplier tube in imaging the

photon emissions of ^{125}I when coupled to a CsI(Na) scintillating crystal array which had 1 mm x 1 mm size elements. The second task was to design, have built, and test a new high resolution parallel hole collimator. The collimator was constructed out of copper laminates using a photochemical etching process. The third task was to test the performance of the entire detector system with the high resolution copper collimator using various phantom radioactive sources. It was during these tests that the realized imaging capabilities of the system was quantified. The spatial resolution and system sensitivity were determined. The final task was to compare lead collimator and with the copper collimator in a realistic animal imaging situation. The system was tested by imaging the distribution ^{125}I that had been injected into a mouse via a tail vein.

3.6.1 CsI(Na) Array with 1.0 mm x 1.0 mm Elements

To achieve still higher position resolution an array formed from crystal elements 1 mm x 1 mm in size was implemented. Using the prototype described in section 3.5 of this dissertation, the individual CsI(Na) crystals of the crystal array composed of elements 2 mm x 2 mm x 3 mm in size were resolved when flooded with radiation from ^{125}I . When the 1 mm x 1 mm size crystal elements of the new array were flooded with radiation from ^{125}I it was not possible to resolve the individual crystal elements of the array. In order to resolve the individual crystals, the generation of more intense scintillation light was required to generate more photoelectrons in the position sensitive photomultiplier tube.

3.6.1.1 Raw Flood Image Using 662 keV Gamma-rays

It was possible to resolve each crystal by obtaining a flood image using the 662 keV photons from ^{137}Cs . This is because, as discussed before, the position resolution of the Hamamatsu R3292 position sensitive photomultiplier tube improves as the number of photoelectrons increases. The higher energy photons give rise to more intense scintillation

light which, in turn, results in more photoelectrons in the photomultiplier tube. From the ^{137}Cs raw flood image it was possible to generate a look-up table such that individual crystals were identified by mapping their location from the raw flood image. This is shown in Figure 3.23 and in Figure 3.24.

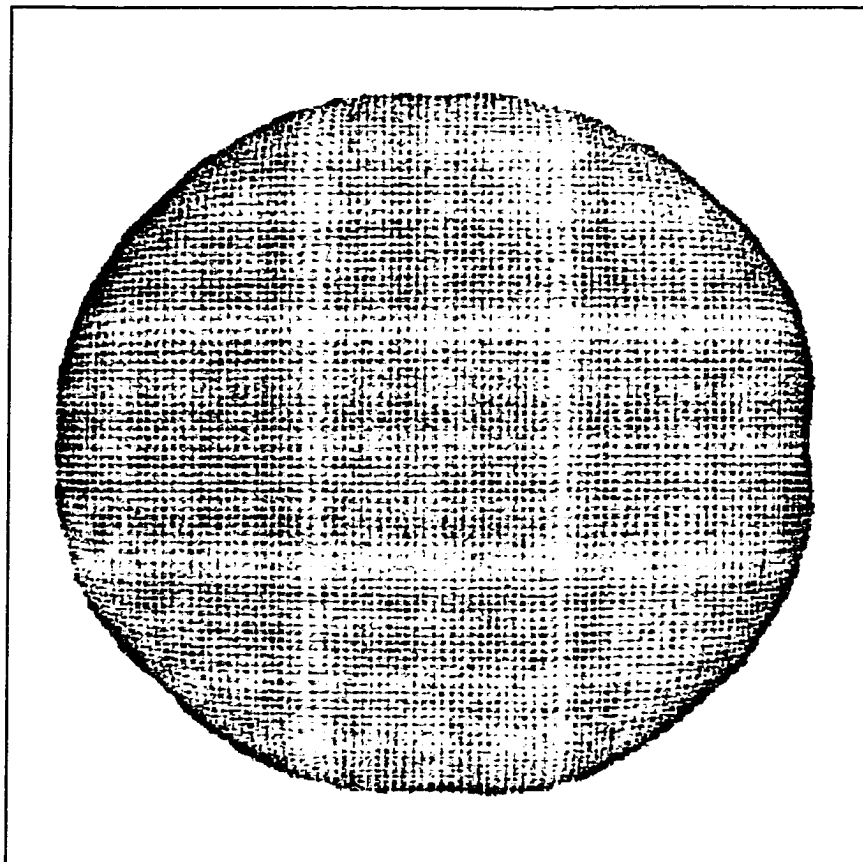


Figure 3.23: The full flood raw image of the 1 mm crystal array is shown. This was accomplished by using a ^{137}Cs point source placed about 10 cm above the CsI(Na) crystal array. Over 95% of the crystals are resolved.

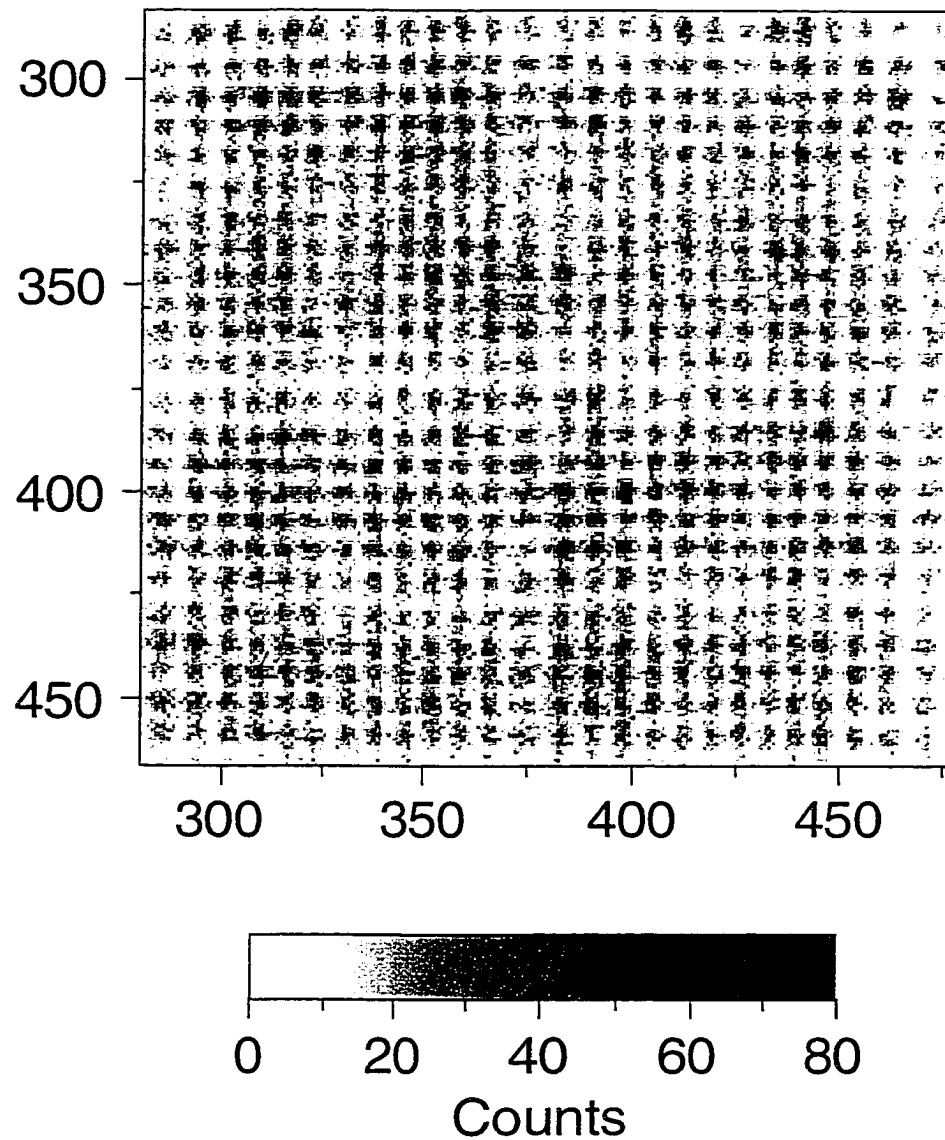


Figure 3.24: Enlargement of a $3 \times 3 \text{ cm}^2$ area of the full flood raw image of the 1 mm crystal array shown in Figure 3.23. Individual crystals are easily resolved.

3.6.1.2 Array Mapping

The same real-time crystal mapping technique as implemented with the first array was accomplished by using the above raw flood image obtained with 662 keV gamma-rays. The real-time data processing system developed and implemented, again using the

Kmax data acquisition system, treats the output of each crystal region individually to correct for crystal-to-crystal scintillation output variations as well as the local photomultiplier tube gain variations. For each event, the sum of the anode signals is used to generate a pulse height energy spectrum. Figure 3.25 is a sample of energy spectra obtained for five neighboring crystals from the CsI(Na) array using the mapping look-up table to define the position of each crystal element.

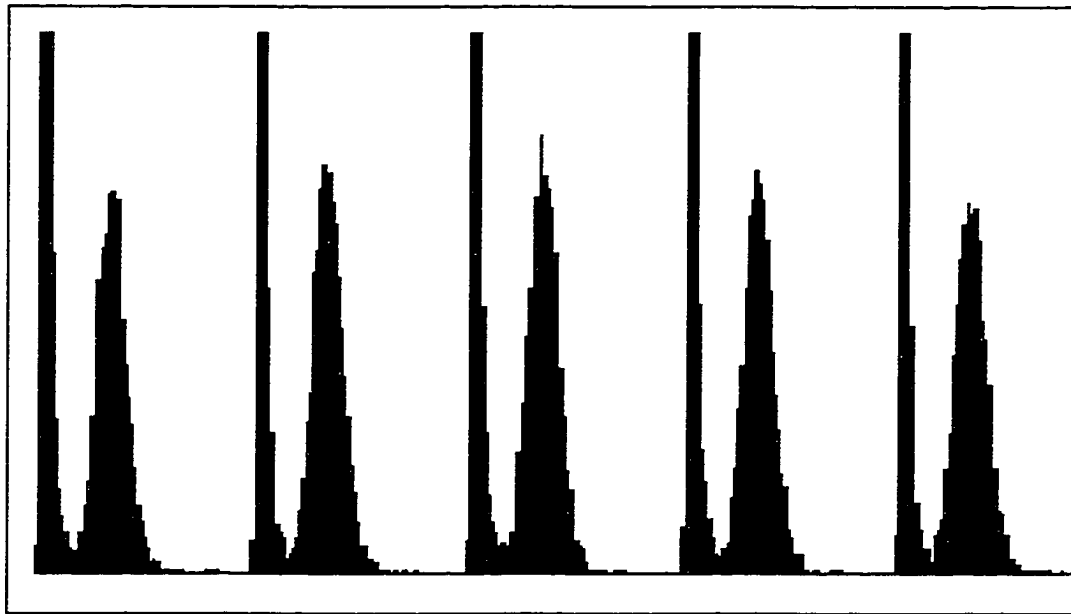


Figure 3.25: Iodine 125 pulse height (energy) spectra for five adjacent crystals generated from the sum of the anode signals using the coincidence mode of detection.

Figure 3.26 depicts a two dimensional representation of the individual gain variations determined at each crystal location. The data processing system is designed to allow each crystal element to have an acceptance window centered about its individual peak by way of another look-up table.

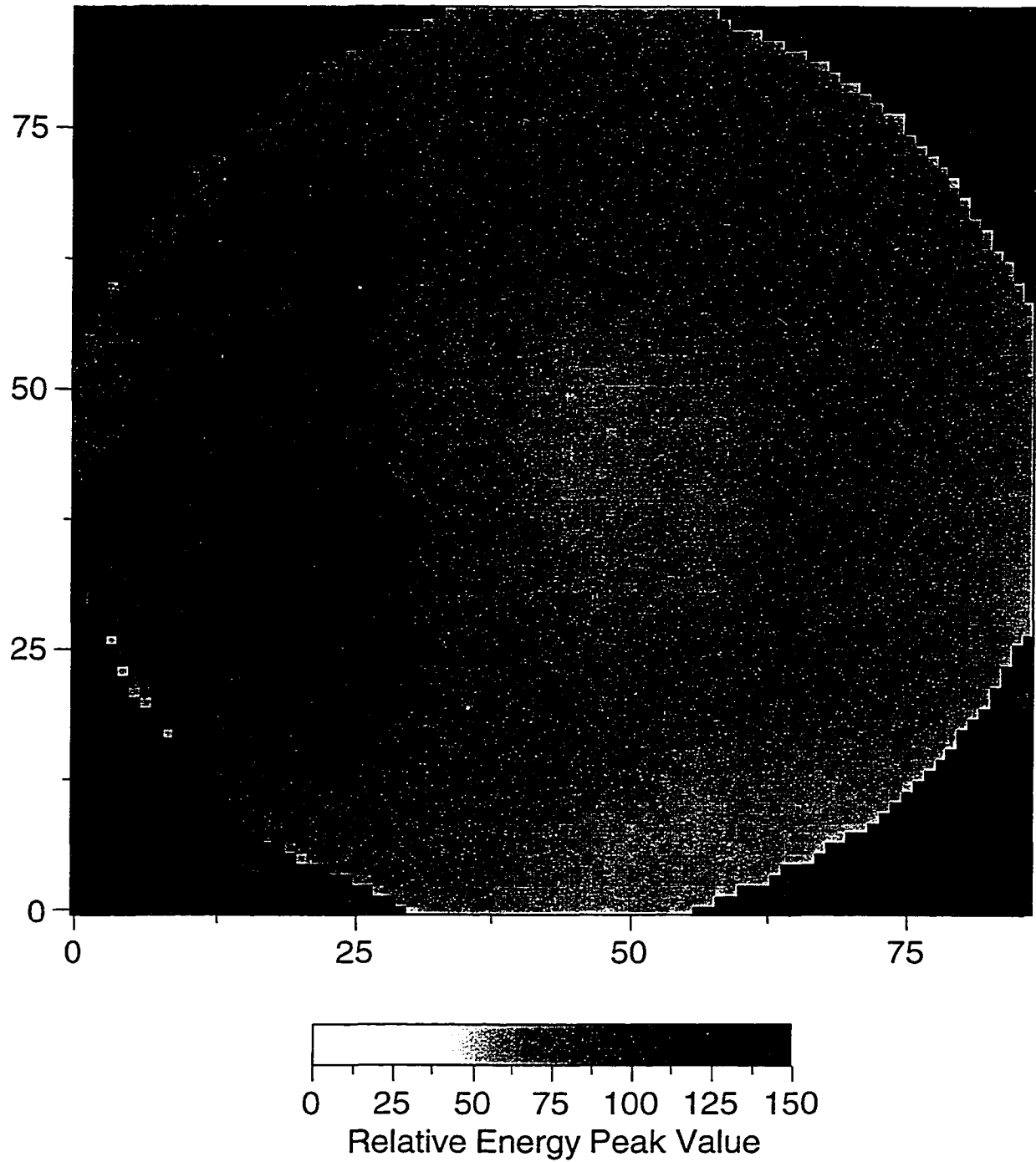


Figure 3.26: Two dimensional representation of pulse height (energy) spectra peak value for ^{125}I for all of the crystals generated from the sum of the anode signals.

3.6.2 High Resolution Copper Collimator

The highest spatial resolution that the lead collimator allowed was ~ 3.5 mm FWHM for a source distance of 1.5 cm. The sensitivity of the detector system with the lead collimator was determined to be 240 cpm/ μCi . The goal of this part of the project was to achieve a spatial position resolution that was less than 2 mm FWHM. A lower Z material could be chosen to construct a high resolution collimator with because of the relatively low energy gamma-rays emitted by ^{125}I . This allowed for the construction of a high resolution collimator out of material that could be photochemically etched.

3.6.2.1 Collimator Construction

A high resolution parallel hole collimator was designed and constructed that was optimized for ^{125}I imaging with a CsI(Na) crystal array with crystal elements 1 mm x 1 mm. The low energy radiation of ^{125}I makes it possible to use materials other than lead to construct collimators. A copper collimator was designed by using relationships described in equations 2.5 through 2.8 of Chapter Two of this dissertation and guided by Keller [15]. The result was a 0.5 cm thick parallel hole copper-beryllium collimator was designed to achieve the best geometric acceptance for this application.

The desired collimator parameters were used by the company Thermo Electron [103] to construct the collimator for this project. This special collimator is constructed out of a stack of 40 layers of copper-beryllium ($\sim 1.9\%$ Be) laminates glued together for a total thickness of 0.5 cm. A proprietary process using photochemical techniques was used by the company to construct square openings of 0.2 mm x 0.2 mm in area separated by 0.05 mm thick septa (see Figure 3.27).

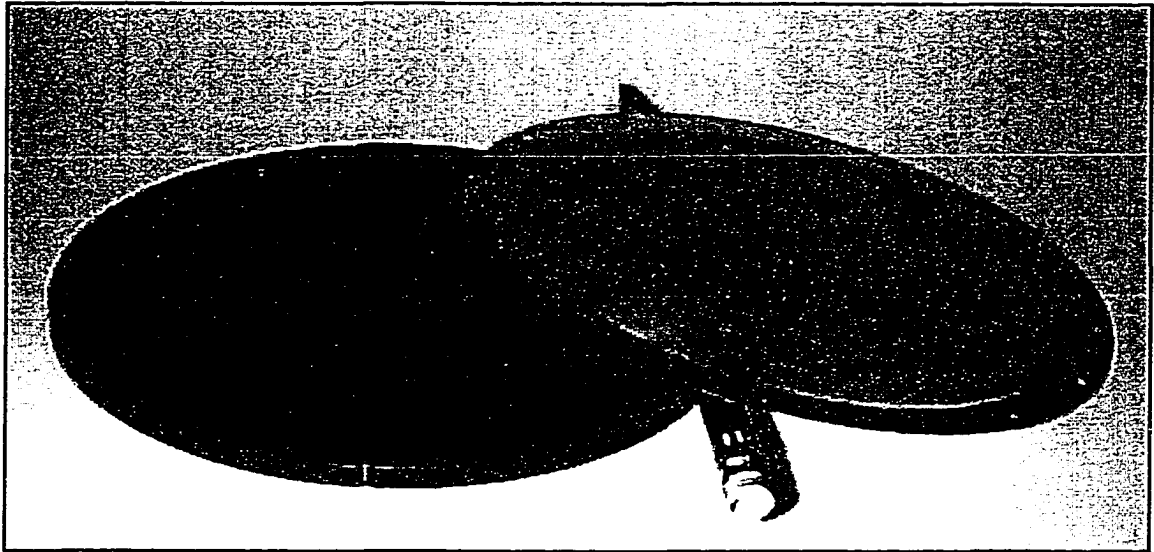


Figure 3.27: A precision stack lamination copper-beryllium collimator with a 0.5 cm total thickness built out of 40 layers similar to the one at the right. Custom built by Thermo Electron of Woburn, MA.

3.6.2.2 Collimator Performance

For a source-to-collimator distance of 1.5 cm the calculated system resolution is 1.5 mm FWHM and the geometric acceptance is $\sim 0.008\%$ with the dead space between the crystals taken into account. From this geometric efficiency an estimate of the actual counts per minute per μCi of activity can be obtained. For example, assume a 1 μCi , 3.7×10^4 disintegrations/sec (dps), with the source of radiation placed in front of the parallel hole collimator and covering an area which is completely within the active field of view of the position sensitive photomultiplier tube. As mentioned before, for ^{125}I , every disintegration results in on average 1.4 gamma-rays or x-rays. Less than one half of the gamma and x-rays emitted travel in the direction towards the collimator. Of those that do, only 0.008% pass through the collimator. The actual activity available for detection is therefore estimated by the following:

$$1.4 \frac{\text{photons}}{\text{disintegration}} \times 3.7 \times 10^4 \frac{\text{disintegrations}}{\text{sec}} \times 8.0 \times 10^{-5} \times 0.5 = 2.0 \frac{\text{photons}}{\text{sec}}$$

Therefore, there are at best 2 photons/sec (or 120 cpm/ μCi) that interact with the scintillator. The sensitivity of the detector system in singles mode for a source placed in the center of the detector was measured to be 68 cpm/ μCi . The measured value is 43% less than the upper estimate of what one might expect from the detector with the copper collimator. This difference may be because in the actual copper collimator the corners of square openings when viewed under magnification are actually rounded slightly resulting in smaller apertures hence a slightly lower sensitivity.

3.6.3 Phantom Imaging Detector Performance Tests

The performance of the detector system with the high resolution copper collimator in place was tested using various phantom sources. In all of the tests a 20% energy acceptance window was implemented which was centered on the energy peak values that had been determined for each crystal element of the array. In most of the tests phantoms with greater than 20 μCi activity of ^{125}I were with an aqueous solution of NaI in 10^{-5} M NaOH.

3.6.3.1 Singles Mode Phantom Studies

A cross hair phantom was made by using two different lengths of polyethylene tubing in which both tubes were filled with approximately ~ 65 μCi of ^{125}I . The longer tube (PE60, Clay Adams, Inc.) had an inner diameter of 0.030" and the second (PE160) had an inner diameter of 0.045". The length of the radioactive region in the larger diameter tube was 3.5 cm and 8 cm in the smaller diameter tubing. The image obtained of this phantom is shown in Figure 3.28.

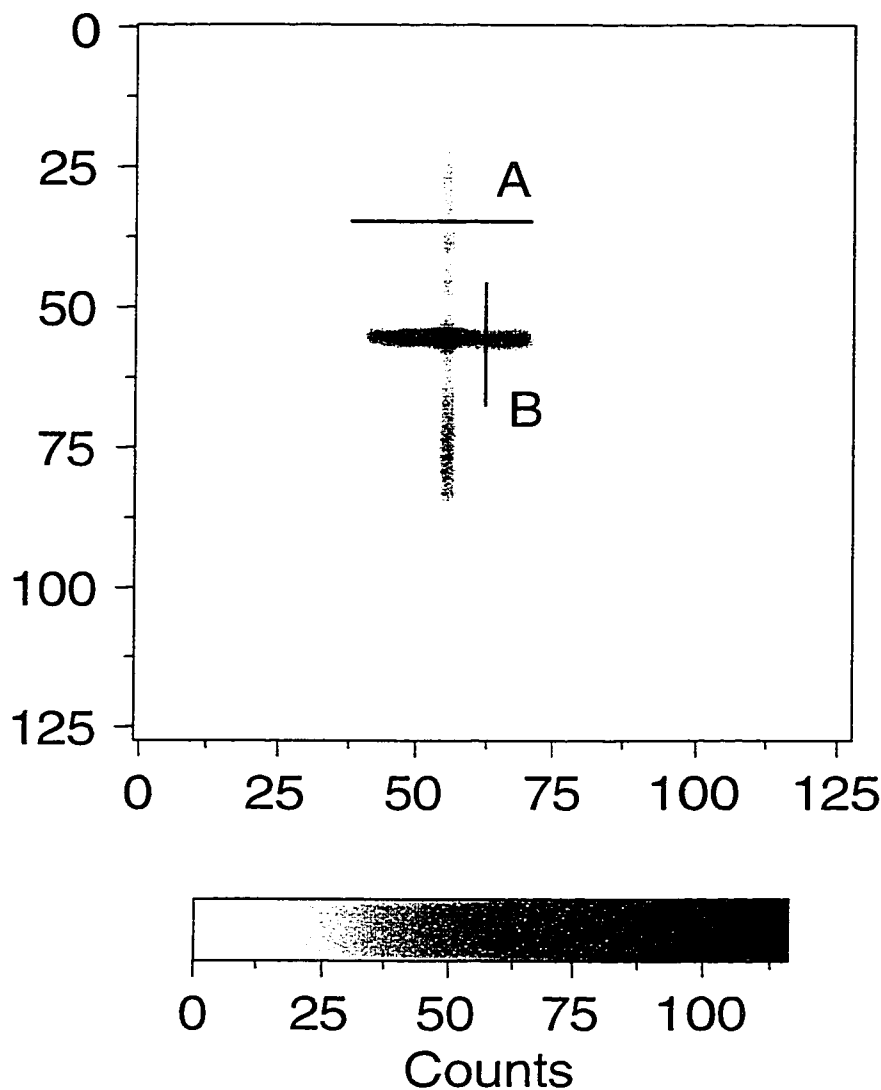


Figure 3.28: Image of a cross pattern made by imaging two plastic tubes filled with ~ 65 μCi of ^{125}I that were placed over each other. The tubes were placed 2 mm in front of the collimator. The active lengths are 8 cm (vertical) and 3.5 cm (horizontal). The FWHM at profiles along A and B is 1.76 mm and 2.46 mm respectively.

The resolution in profile A of the 0.030" diameter tube was 1.76 mm FWHM and for profile B of the 0.045" diameter tube the resolution was 2.46 mm FWHM. The calculated system resolution at a source distance of 2 mm is 1.25 mm FWHM which would result in a width of 1.47 mm FWHM for the 0.030" (0.768 mm) diameter line source. The measured width of 1.76 mm FWHM is in near agreement with the expected result. For the 0.045" (1.152 mm) diameter line source the measured width is 2.46 mm FWHM. In this

case the line source is illuminating two rows of crystals therefore one would expect a line image width of 2.69 mm FWHM which is also in near agreement with the image result.

Another phantom was constructed to test the high resolving power of the detector system. A loop was made out of 0.030" plastic tubing filled with approximately $\sim 65 \mu\text{Ci}$ of ^{125}I . The separation (center-to-center) of the loop ends that form the right hand opening of the loop was 2.5 mm (see Figure 3.29).

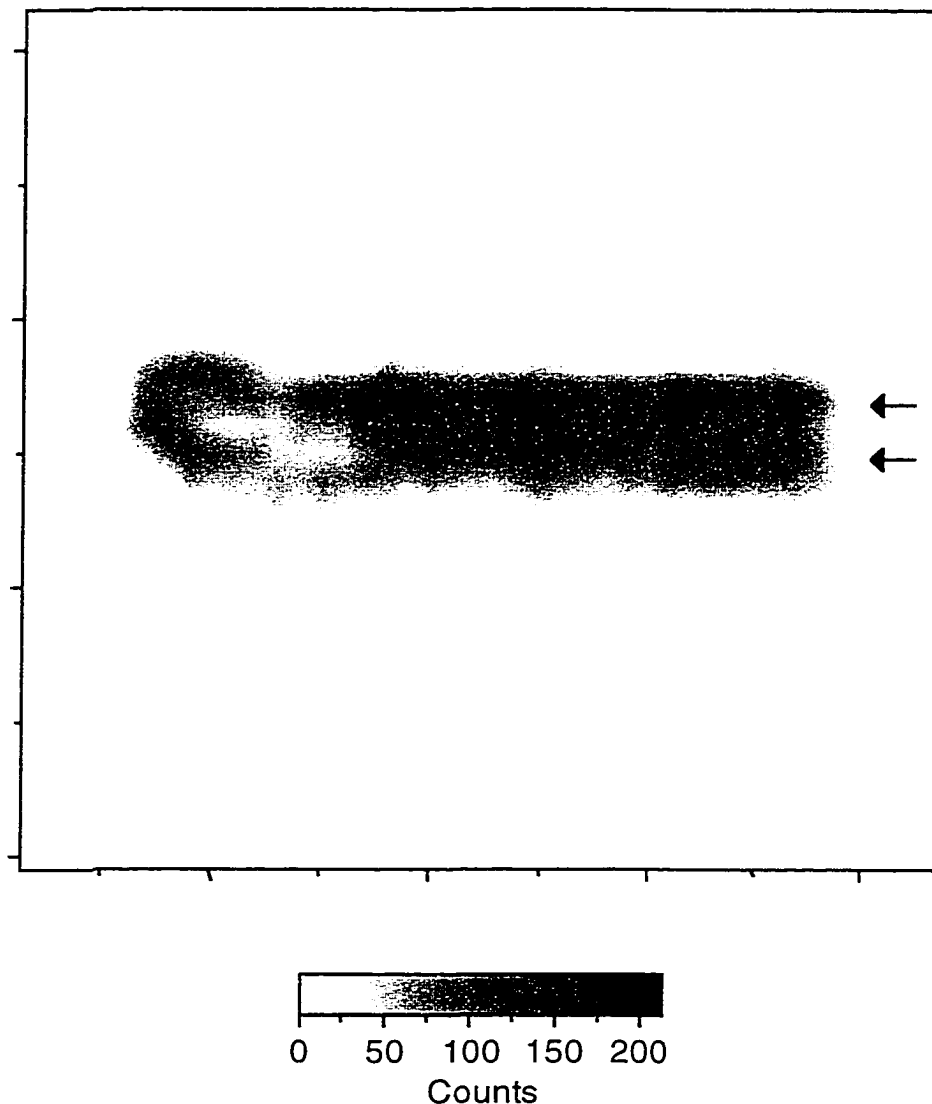


Figure 3.29: Image obtained of a loop constructed out of 0.030" plastic tube filled with $\sim 65 \mu\text{Ci}$ of ^{125}I . The separation (center-to-center) of the tube ends forming the right hand opening of the of the loop was 2.5 mm. An acquisition time of 15 minutes was used to obtain this image.

It is just possible to visualize the two ends. This is the expected limit of resolution as the crystal elements are 1 mm x 1 mm in size separated by 0.2 mm of dead space. Therefore the minimum resolvable separation of two line sources 0.77 mm (0.030") in width is 2.4 mm. This is true assuming an ideal orientation with the crystal matrix where one line source is directly over one row of crystals and the other line source is two rows over. The loop was placed in contact with the face of the collimator. The discontinuities observed in the image are because of trapped air bubbles in the tube.

A grid phantom was constructed using a 0.75" (19.2 mm) thick, 1.5" (38.4 mm) diameter plastic disk with a grid pattern of 0.065" (1.66 mm) thick slots cut 0.5" (12.8 mm) deep separated by 0.25" (6.4 mm). The disk was inserted slot side down into a plastic cylinder which had a bottom wall thickness of 0.25". The phantom with the grid disk inserted was filled with ~20 μCi of ^{125}I to a depth of 0.5". The cylinder bottom was placed 1 mm above the collimator. An image of this phantom is shown in Figure 3.30. It was difficult to obtain uniform loading of the phantom which is responsible for the apparent enhancement of the radiation signal seen in some regions of the image.

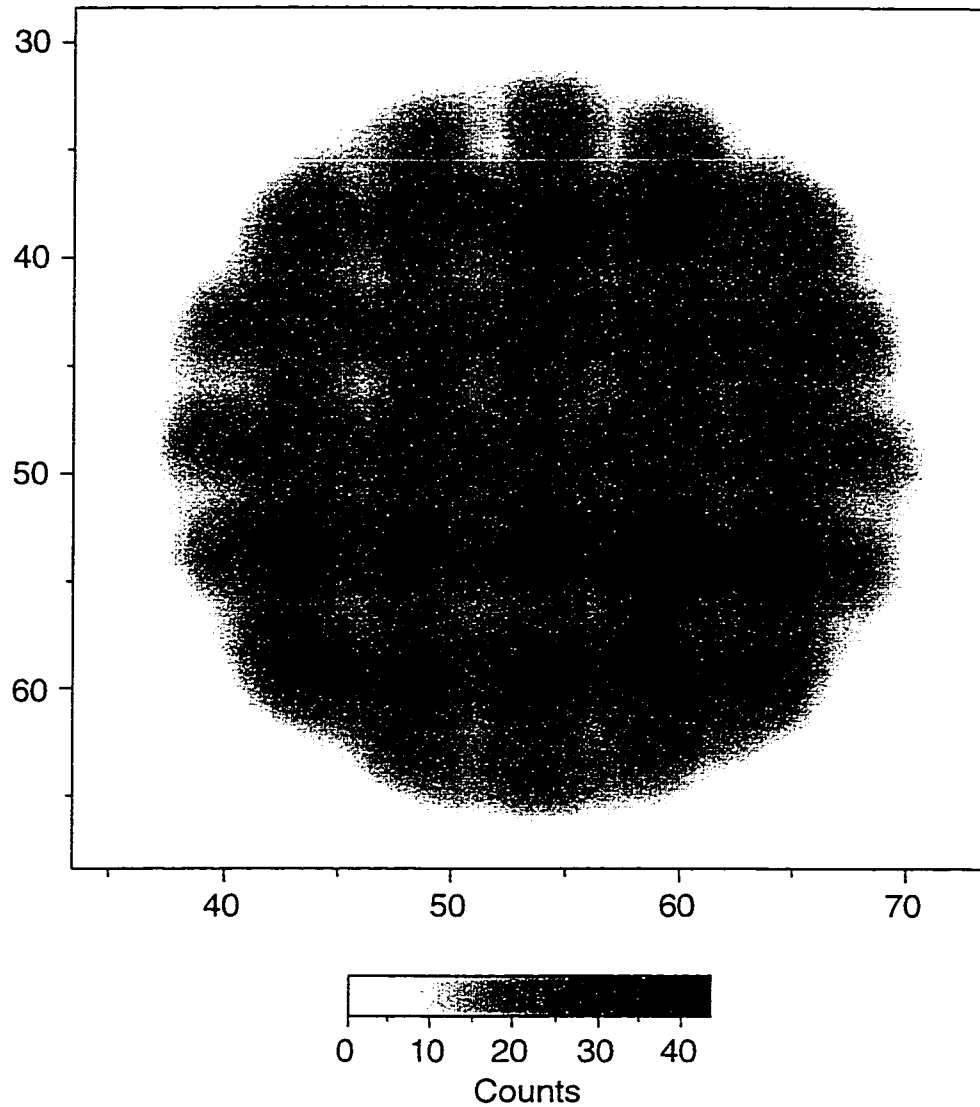


Figure 3.30: Image of a ^{125}I filled grid phantom.

3.6.3.2 Coincidence Mode Phantom Studies

A test was performed using the detector in the coincidence mode of operation. As stated above the coincidence mode was found to be most useful when imaging low amounts of radioactivity. The random coincidence rate with the two detectors placed 2 cm apart was less than 1 cpm for a 20% energy window. Figure 3.31 shows two images obtained with a three minute acquisition time of a 2 μCi ^{125}I source taken in singles and coincident modes.

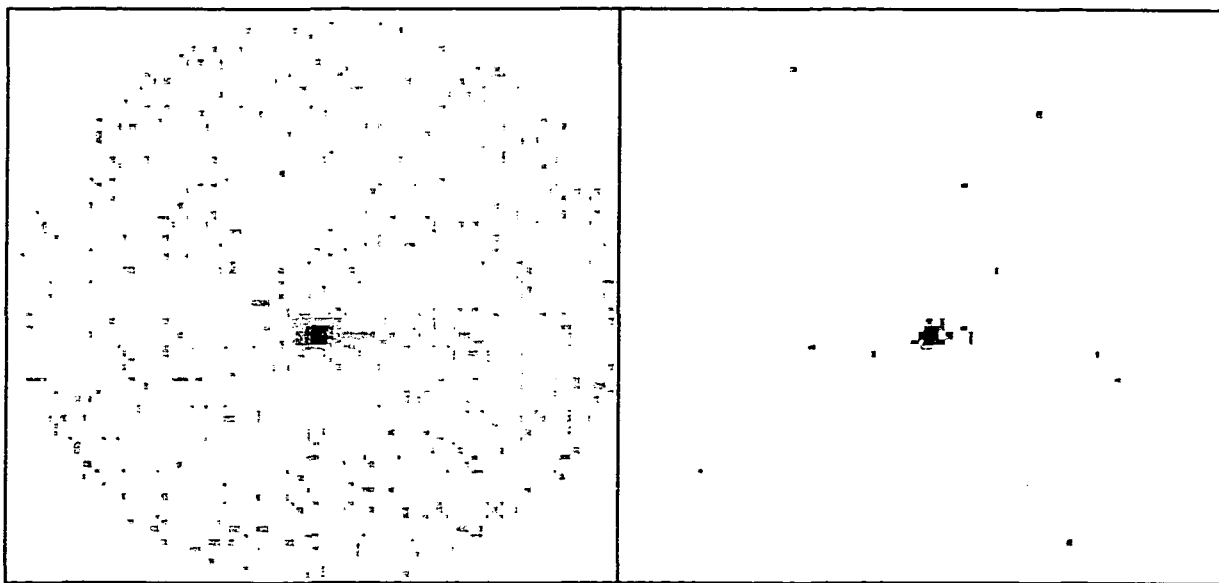


Figure 3.31: Two corrected images obtained with a three minute acquisition time of a 2 μCi ^{125}I source taken in singles (left) and coincident (right) mode. The imaging and coincident detectors were placed 2.0 cm apart and the source was placed halfway between them.

The phantom was placed halfway between the two detectors. The phantom was placed halfway between the two detectors. The ratio of signal over image total for a region of interest covering the source was 0.45 (373/822) for the singles case and 0.77 (44/57) for the coincidence case. The system sensitivity in coincidence mode in the test described here was 30 cpm/ μCi which, as expected, is slightly less than half of sensitivity of the system during singles mode.

3.7 Imaging Iodine Uptake in a Mouse

The detector system can be operated with either the low resolution lead collimator or the high resolution copper collimator in place. The low resolution lead collimator would be used in applications when high sensitivity is required such as in a dynamic imaging study.

In singles mode, the low resolution lead collimator when compared to the copper collimator requires 8 times shorter acquisition times to get the same image statistics.

A mouse was imaged after receiving a tail vein injection of ^{125}I in order to compare the results of imaging the biodistribution of ^{125}I with the low spatial resolution lead collimator and the high spatial resolution copper collimator. This was done to provide a baseline to the nature of the uptake of the label using two different collimators. The mouse was a 17.5 gm male *Peromyscus maniculatus*, which was injected through a tail vein with a 5 μCi dose of ^{125}I (Dupont NEN Inc. [1], NEZ033A:carrier free; SA = 17.4 $\mu\text{Ci}/\mu\text{g}$; pH 8-10; in 20 μl 0.9 NaCl) after being anesthetized with 4% chloral hydrate administered by an intraperitoneal injection. At approximately two hours after the injection of ^{125}I , the mouse was sacrificed by an anesthetic overdose and was imaged. The mouse was imaged in singles mode both with the high resolution copper collimator and the low resolution lead collimator that was described earlier. The resulting images are shown in Figure 3.32.

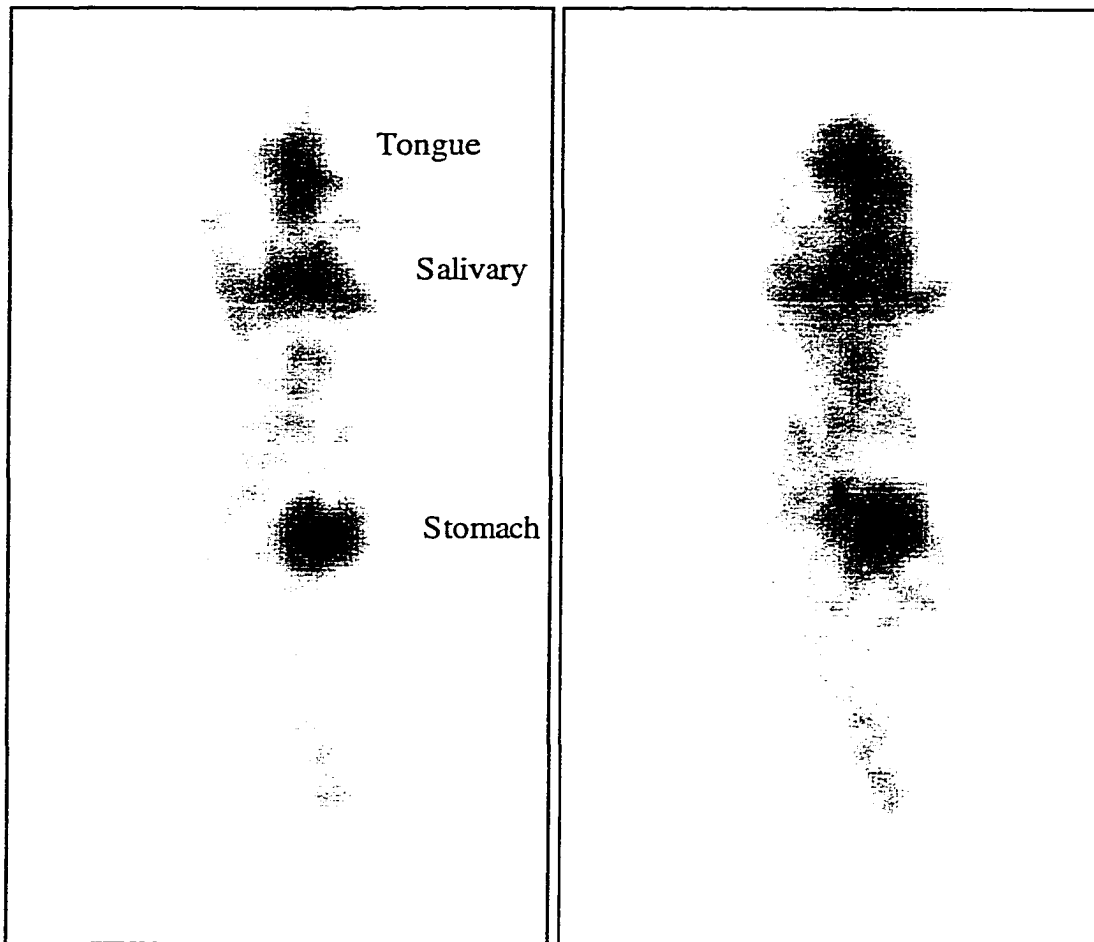


Figure 3.32: Images obtained of iodine distribution in 17.5 gm male *Peromyscus maniculatus* mouse two hours after injection of $5\ \mu\text{Ci}\ ^{125}\text{I}$. The image on the left was obtained using the high resolution copper collimator while the right image was obtained with the standard lead collimator in place. The left image represents a total acquisition time of the 45 minutes while the image on the right required 5.6 minutes.

A typical biodistribution of ^{125}I was observed [104]. The images show that the detector system when fitted with the high resolution copper collimator provides finer detail of the structure of the uptake than that obtained with the lead collimator. This is particularly apparent in the area of the mouth where the tongue region shows high accumulation of iodine. The tongue region shows a more defined image in the copper collimator. The iodine accumulation in salivary glands and stomach also appear more defined as well. The actual distribution of iodine to these structures was confirmed on autopsy with liquid

scintillation counting of isolated organs (data not shown). Both images have the same number of image counts, 45 minutes of image acquisition were required to obtain the image with the high resolution copper collimator while the image with the lead collimator only required 5.6 minutes.

The system described above is now in use in the Biology Department at the College of William and Mary and has most recently been used evaluate the detector system relative to a study conducted by a group at Johns Hopkins University [105] in which a non-imaging gamma-ray detector was used to measure the uptake in the mouse brain of a compound (RTI-55) labeled with ^{125}I . The next chapter presents the preliminary results of this comparison.

Chapter 4

Imaging Receptor Binding in the Mouse Brain

The detector system described in section 3.6 was used on a mouse to image the *in vivo* uptake of the ^{125}I -labeled tracer methyl 3 β -(4-iodophenyl) tropane-2 β -carboxic acid methyl ester, also known as RTI-55(β -CIT) [106]. Described in this chapter are the initial results of applying the detector system developed in this project with the results of a mouse brain study reported by Mochizuki et al. [105] at Johns Hopkins University. Mochizuki et al. have reported using a non-imaging gamma-ray detector to measure only the mouse brain uptake of the ^{125}I -labeled RTI-55 as a function of time. This present study substantially extends the earlier study, since prior to the William and Mary detector system, there existed no high spatial resolution imaging detector optimized to image ^{125}I in small animals.

RTI-55 acts as a cocaine analog and binds to unique protein receptor molecules termed “transporters” that are involved in the movement of dopamine and serotonin across cell membranes in the brain [106]. The study of the nature of uptake and metabolism (pharmacokinetics) of RTI-55 is of interest to those studying the mechanism and treatment of human neurological disorders as well as cocaine action [105]. RTI-55 has been shown

to cross the blood brain barrier and label the striatum of the brain, the hypothalamus, and the thalamus[107]. Imaging RTI-55 in primates has been performed using a clinical SPECT system with a ^{123}I -label [108].

4.1. Static Biodistribution of RTI-55

The static biodistribution study was undertaken using a 25 gm, male CD-1 mouse (Charles River, Wilmington, DE, USA). The mouse was anesthetized with an intraperitoneal injection of 4% chloral hydrate. About 15 μCi of ^{125}I labeled RTI-55 (Dupont NEN, Inc., NEX 272) [1] in 50 μl phosphate buffered saline was injected into the tail vein of the mouse. Studies were conducted using the detector system operated in singles mode with the low resolution (therefore higher sensitivity) lead collimator. This configuration was chosen to obtain the maximum number of image counts for short intervals of time. First prone and then 90° side images were obtained of the mouse 30 minutes after the injection of RTI-55. The prone image was obtained first with a total acquisition time of 40 minutes. The resulting image is shown in Figure 4.1.

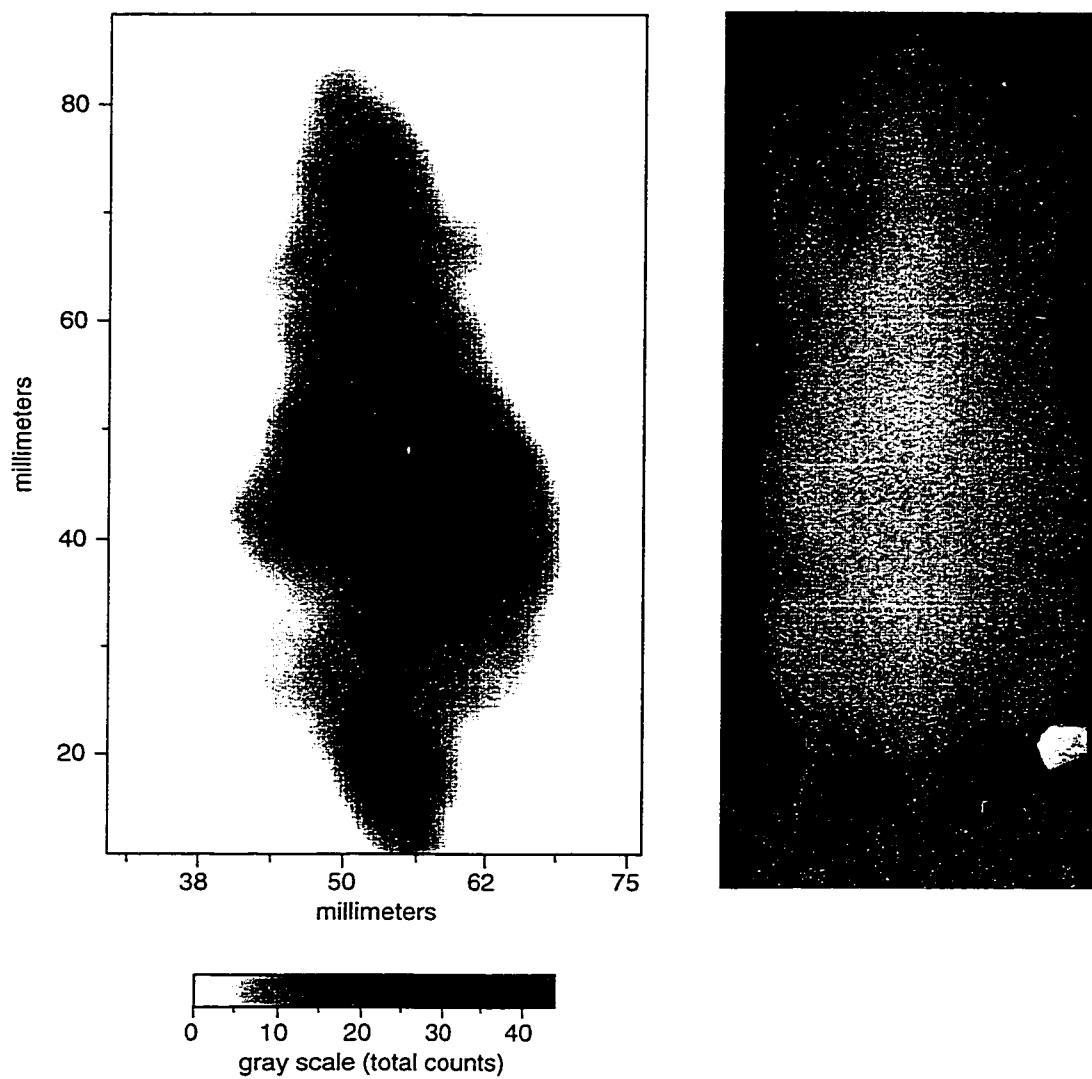


Figure 4.1: Image of the biodistribution of about 15 μCi of ^{125}I labeled RTI-55 that had been injected into the tail vein of a 25 gm male CD-1 mouse. Total acquisition time of the image was 40 minutes which was started 30 minutes after the injection .

The gray scale for the RTI-55 image was compressed to highlight the biodistribution of the RTI-55. After the image was obtained, the detector was re-positioned 90° to image from the side. The resulting image from the new direction is shown in Figure 4.2.

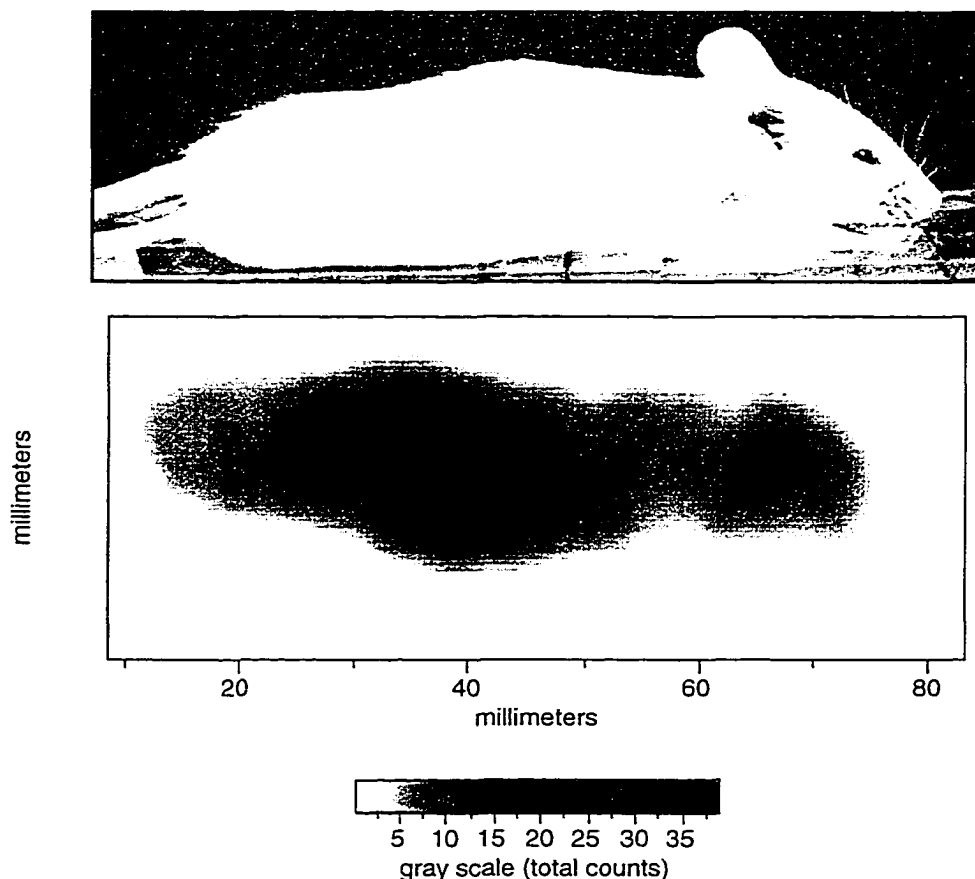


Figure 4.2: Side-view image of the biodistribution of about 15 μCi of ^{125}I labeled RTI-55 in the same mouse as shown in Figure 4.1. Total acquisition time of the image was 45 minutes which was started 80 minutes after tail vein injection.

It is clear from Figure 4.1 that RTI-55 is distributed throughout the core body and head of the mouse within 30 minutes after injection. Figure 4.1 and 4.2 taken together also indicate that the ^{125}I signal in the head is mainly associated with the brain. Following this study a second animal was used for a dynamic study of the time-dependent biodistribution of ^{125}I RTI-55.

4.2. Dynamic Dependence of the Biodistribution RTI-55

Mochizuki et al. [105] used a NaI crystal scintillator attached to a standard end-window photomultiplier tube. They limited the direction of gamma-ray detection by using a lead brick with a single 5.0 mm diameter collimating hole. They positioned the detector to touch the animal and directed it toward the left temporal region and the striatum of the brain. They used this configuration to study the effects of various “blocking” drugs on the rate of uptake of ^{125}I -labeled RTI-55 in the brain. They reported that RTI-55 uptake was blocked by two drugs, paroxetine and 1-[2-bis(4-fluorophenyl)methoxy]ethyl]-4-[3-phenylpropyl]piperazine dihydrochloride (GBR 12909). Their complete study involved 20 mice which included 8 control animals. They observed that a combination of paroxetine and GBR 12909 was the most effective blocker of ^{125}I -labeled RTI-55 uptake in the region of the brain seen by the detector[105].

In the study reported here obtained with the William and Mary ^{125}I imaging system, a 27.5 gm male CD-1 mouse was anesthetized as previously described and about 15 μCi of ^{125}I labeled RTI-55 was injected via a tail vein. The mouse was imaged with the low resolution high sensitivity detector configuration described earlier for a total 180 minutes with dynamic images generated at 11 minute intervals. Figure 4.3 shows the total accumulated distribution after 180 minutes of the ^{125}I along side a photograph of the CD-1 mouse.

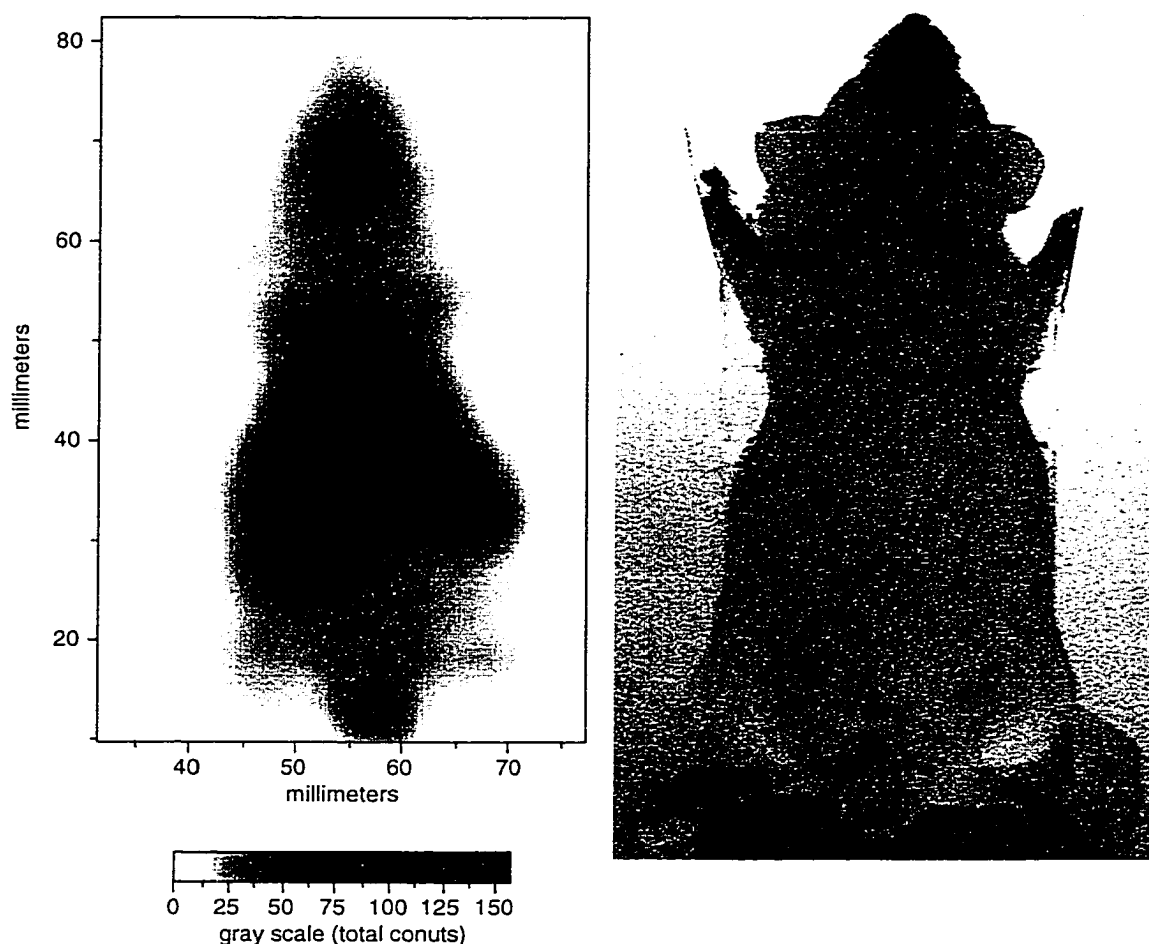


Figure 4.3: Image of the accumulated biodistribution of RTI-55 after 180 minutes following the injection of about 15 μCi of ^{125}I -labeled RTI-55 into the tail vein of a male CD-1 mouse. A photograph of the mouse taken during the experiment is also provided for comparison.

A series of images acquired every 11 minutes with image overlaps of 1 minute is presented in Figure 4.4. The time indicated at the bottom of each image is the elapsed time following the injection of ^{125}I -labeled RTI-55.

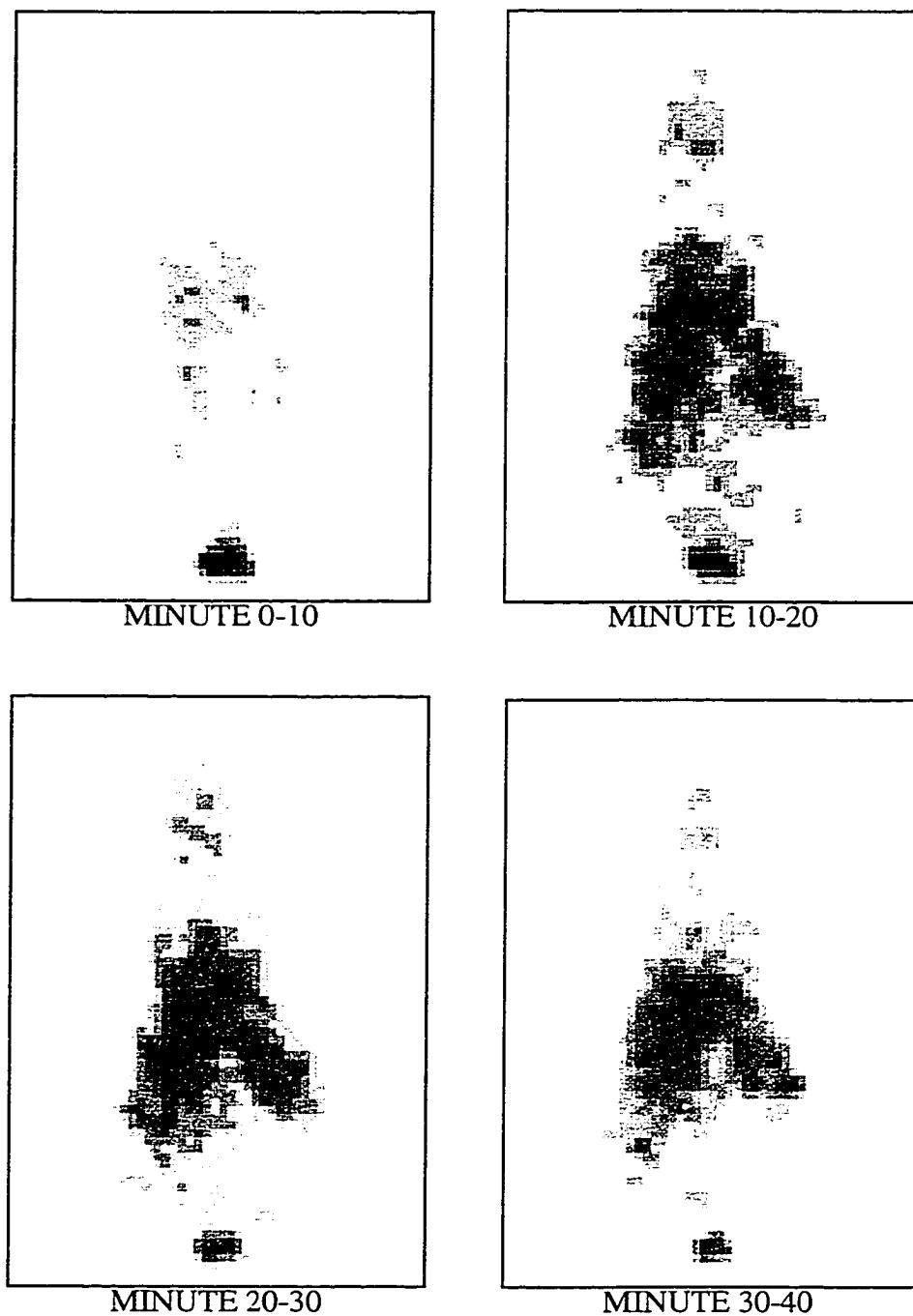


Figure 4.4: A series of images of the distribution of RTI-55 in a mouse acquired for 11 minutes in which each image overlaps in time the previous one by 1 minute. In all of these images the head is at the top. The time provided at the bottom of each image indicates the time span since the injection time that the image was accumulated.

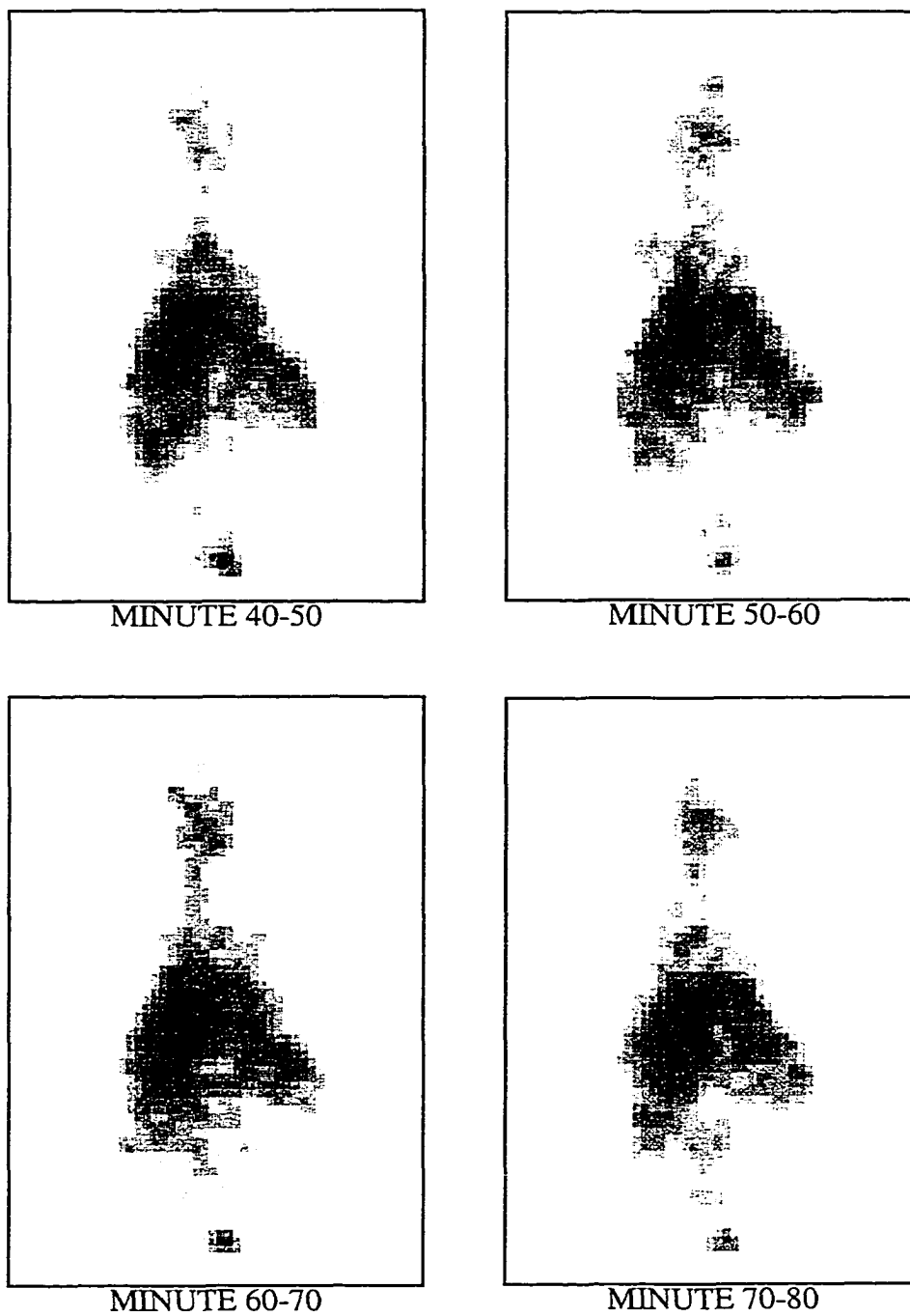
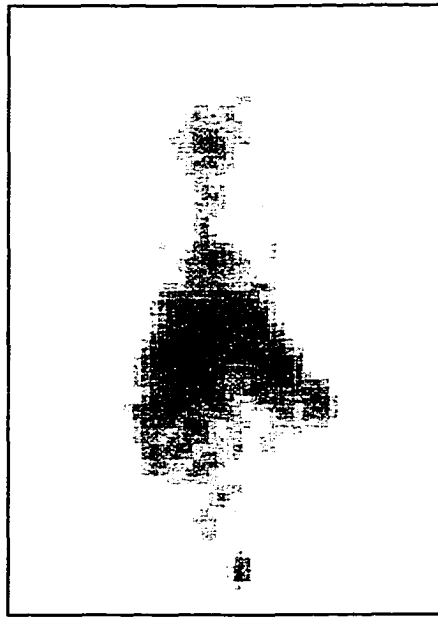
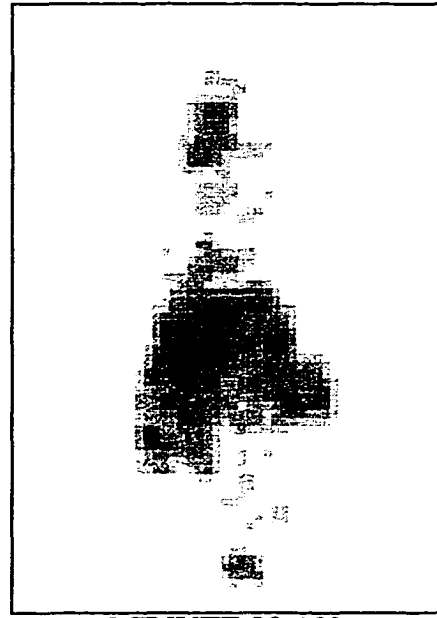


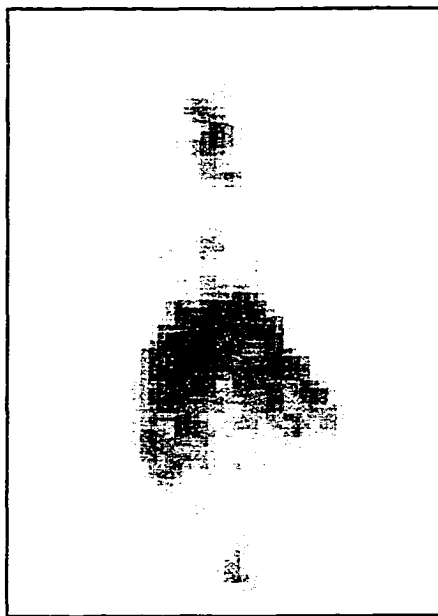
Figure 4.4 continued.



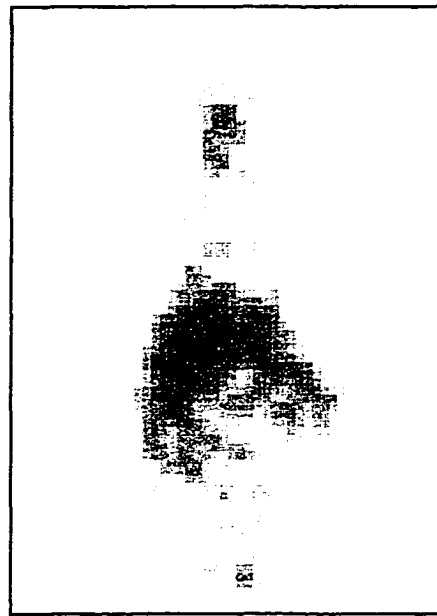
MINUTE 80-90



MINUTE 90-100



MINUTE 100-110



MINUTE 110-120

Figure 4.4 continued.

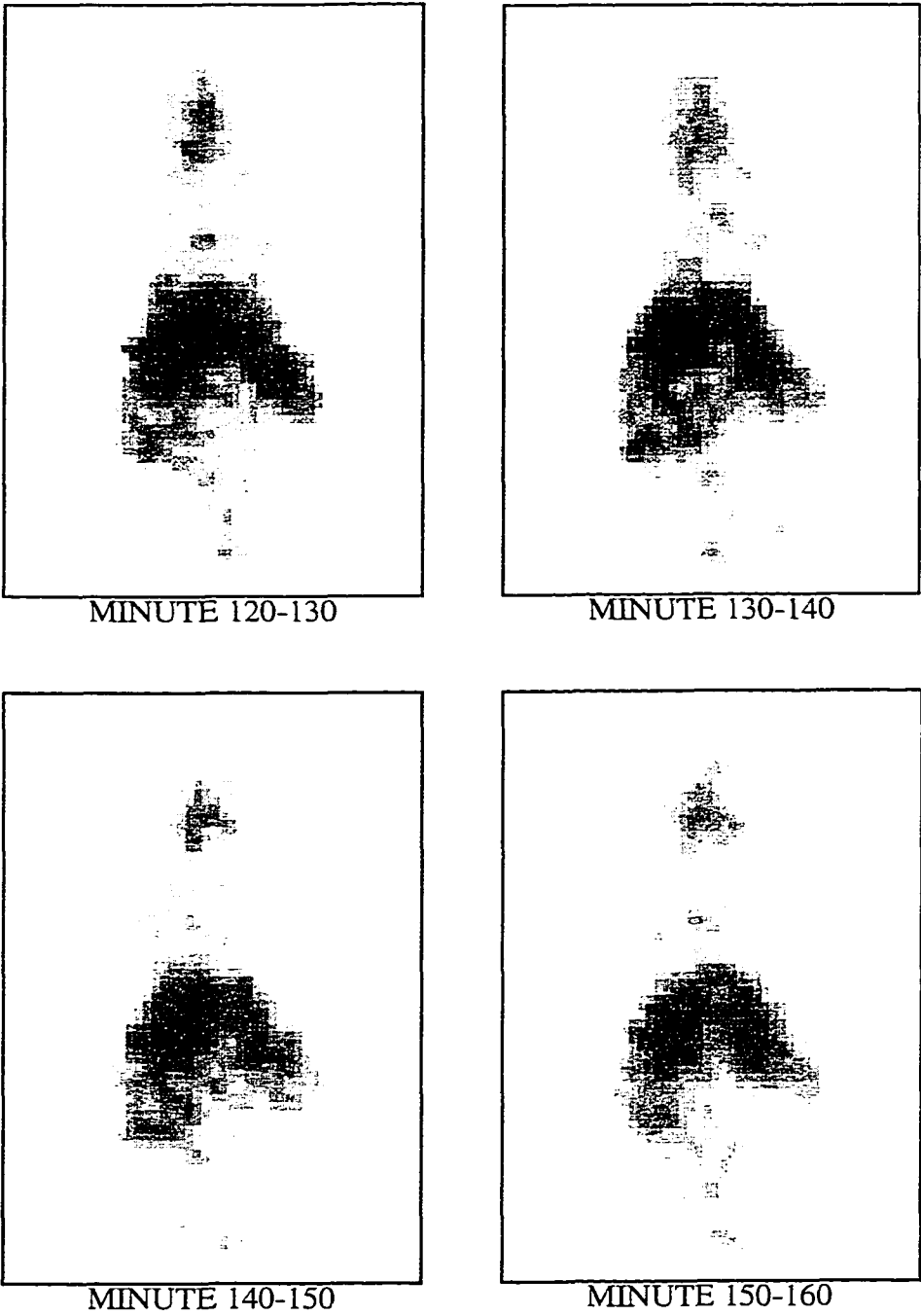


Figure 4.4 continued.

Taken together these images qualitatively demonstrate the rapid uptake of RTI-55 into the head region. Three regions of interest were chosen for further analysis and the total counts in the areas were tabulated and normalized to the uptake at 60 minutes post injection and then plotted. The areas selected were two adjacent regions in the head and one in the liver as illustrated in Figure 4.5.

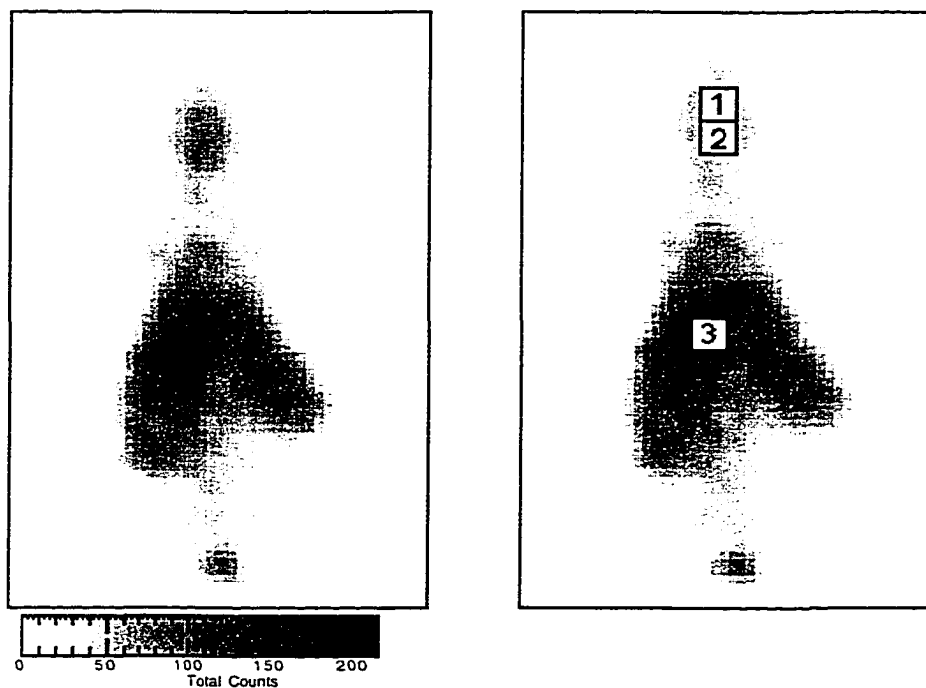


Figure 4.5: Two images of the same data of the distribution of RTI in the CD-1 mouse. The boxes in the right image indicate three regions of interest (ROI-1, ROI-2 and ROI-3) used to tabulate the accumulation rate.

The regions of interest (ROI-1, ROI-2) in the head are located in two adjacent areas in the mid line beginning just behind the level of the eyes and extending toward the tail to the region of the cerebellum. The third region (ROI-3) of interest includes a portion of the liver. All three regions individually represent an area of 5 mm x 5 mm (25 pixels). A series of plots were generated showing the rate of uptake for each of the three regions. All plots are normalized to the counts accumulated for the 11 minute interval occurring 60

minutes after injection of the ^{125}I -labeled RTI-55 which is the same normalization method used by Mochizuki et al.[105] in their report. A plot of the change in time of the total counts in the image with the counts in the region at the top of head is shown in Figure 4.6.

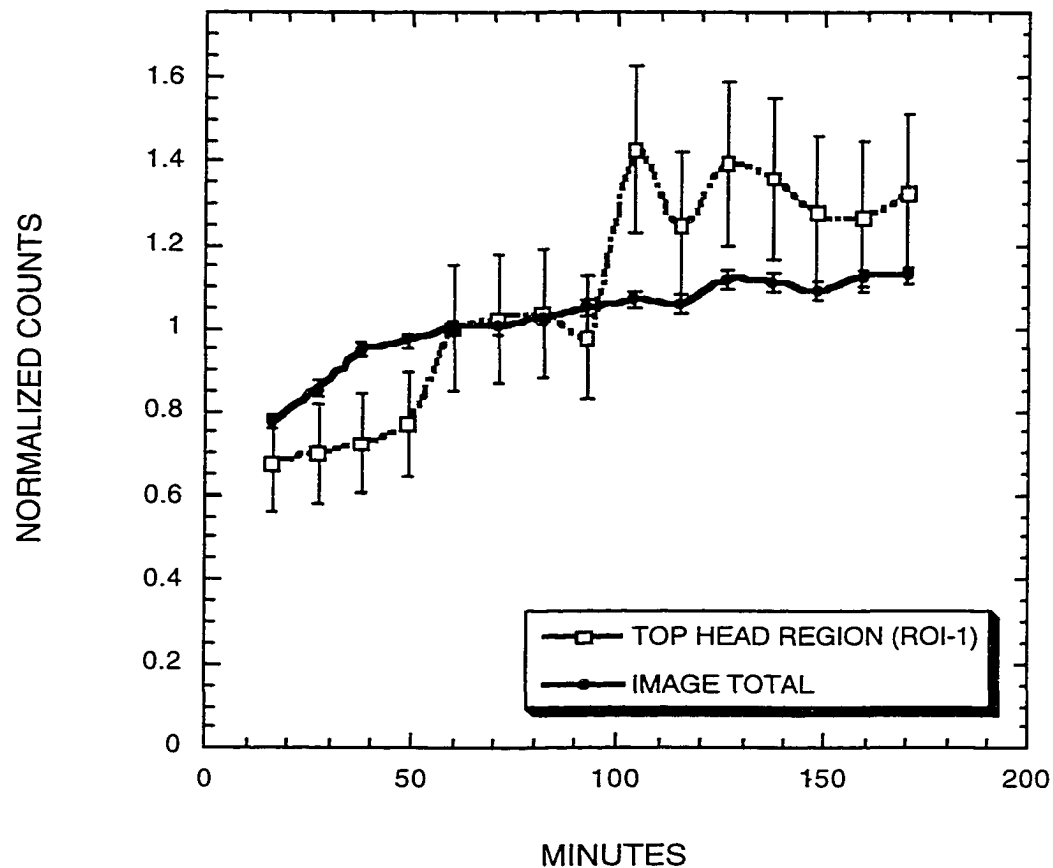


Figure 4.6: Plot of the change over time of the total counts in the image plotted with the counts in the region of interest that is at the top on the head(ROI-1). Error bars are plus and minus one sigma (σ) determined by propagating the errors using Poisson statistics ($\sigma^2 = \text{number of counts}$)[99].

A similar plot was made using the lower head region as the region of interest relative to the change in total counts. This is as shown in Figure 4.7.

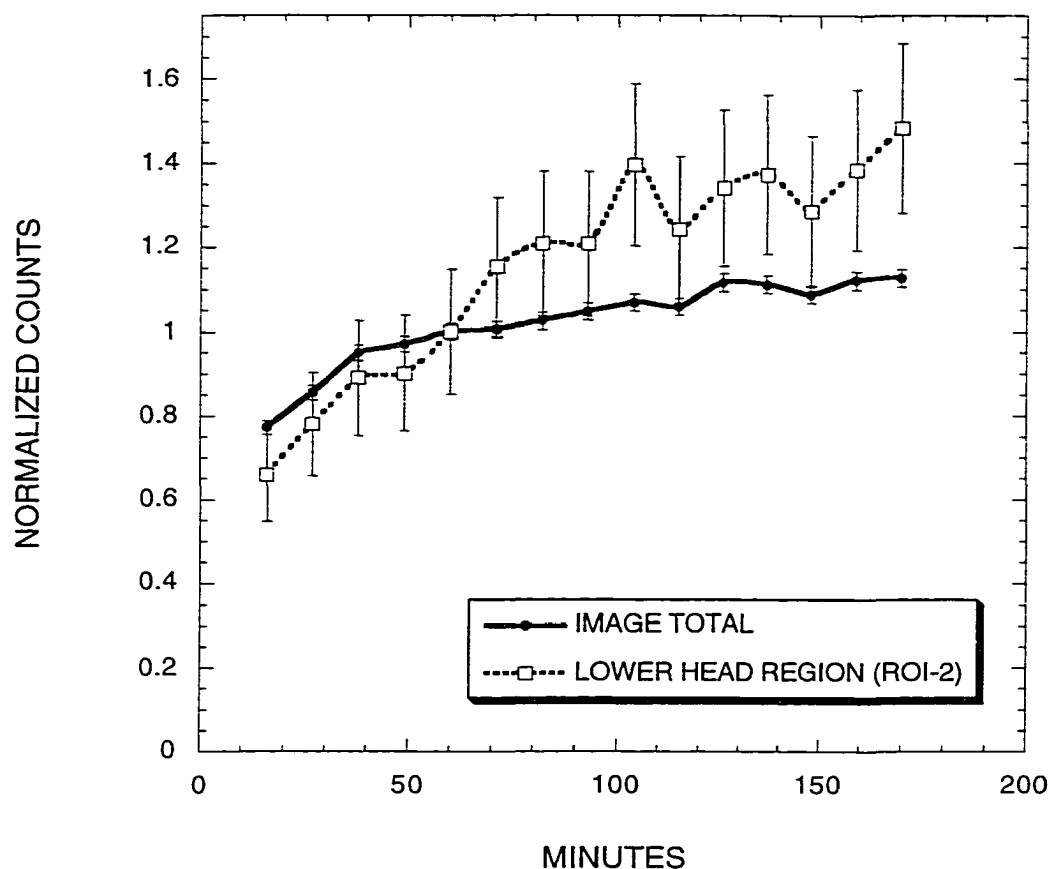


Figure 4.7: Plot of the change over time of the total counts in the image plotted with the counts in the region of interest in the lower part of the head. Error bars were determined in the same manner as in the previous plot.

The pattern of radioactive accumulation in the two regions of the head shows a distinct step pattern wherein there is an increased rate of accumulation of counts in the head in the period of approximately 50 to 100 minutes. This results in a greater accumulation of signal in the head after 100 minutes compared with the distribution in the whole body. A third plot showing the time-dependent accumulation in the liver region is shown in Figure 4.8. Here the step pattern seen in the head is not apparent and the rate of accumulation in

the region of the liver does not appear to be significantly different compared with the total counts.

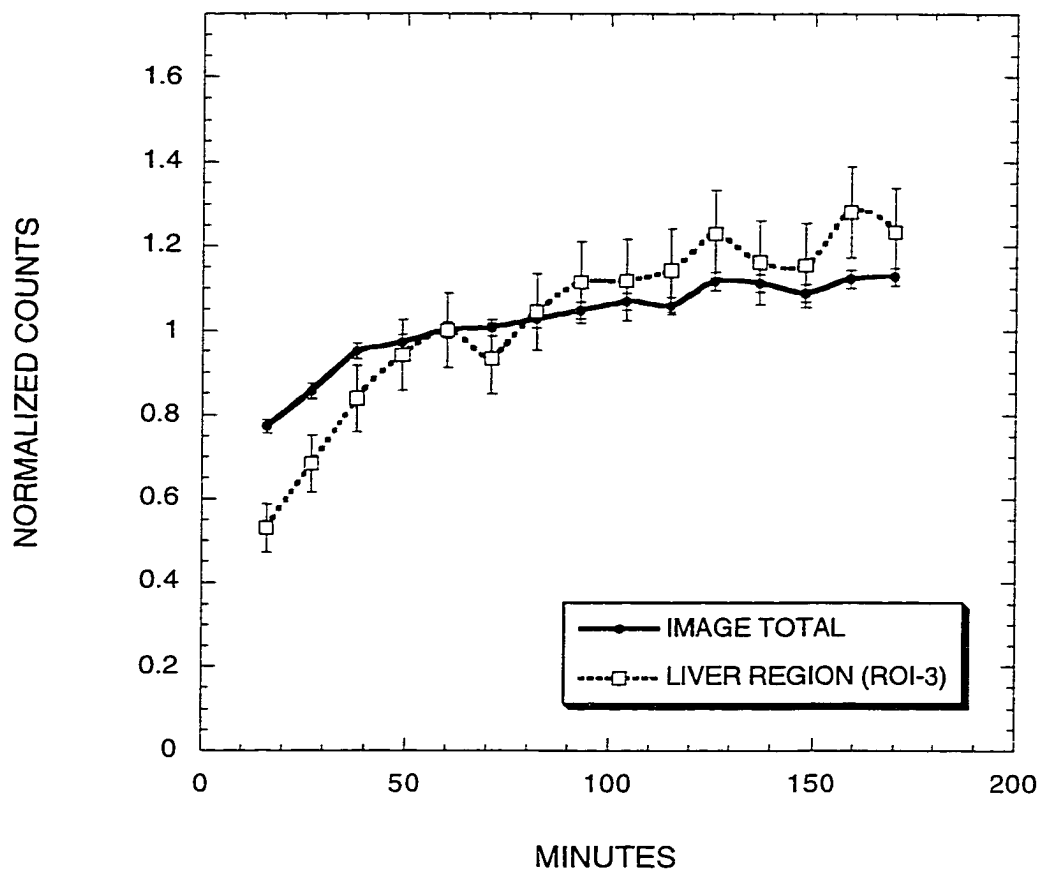


Figure 4.8: Graph of the change over time of the total counts in the image plotted with the counts in the liver region. Error bars were determined in the same manner as in the previous plot.

Figure 4.9 is a graph of the data obtained for the lower head region compared with the plotted normalized data reported by Mochizuki et al. [105] for three mice. One can see that the results from the two studies are similar.

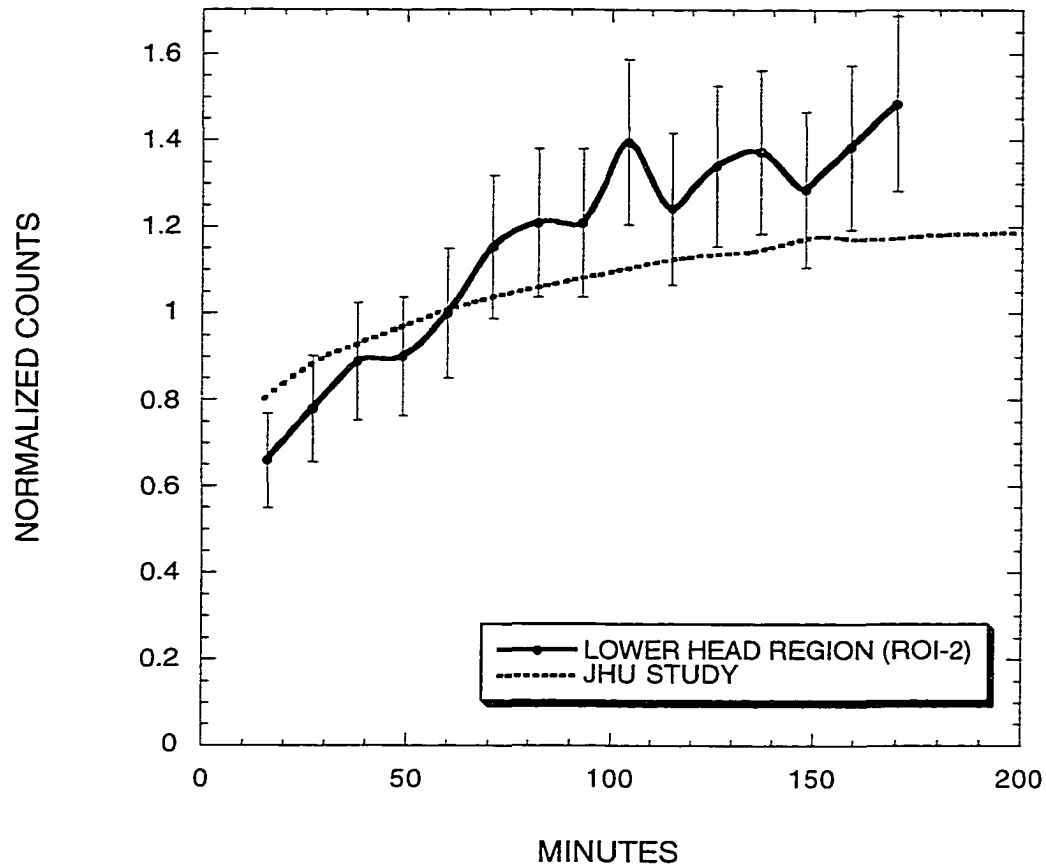


Figure 4.9: Graph of the change over time of the counts in lower head region from the present study plotted with the data reported by the Johns Hopkins University group (JHU) [105]. Error bars were determined in the same manner as in the previous plot.

Figure 4.10 is a plot of the data in all of the preceding graphs. This comparison indicates that there may be important differences in the rate of accumulation of RTI-55 between the two head regions and the liver region compared with the total body.

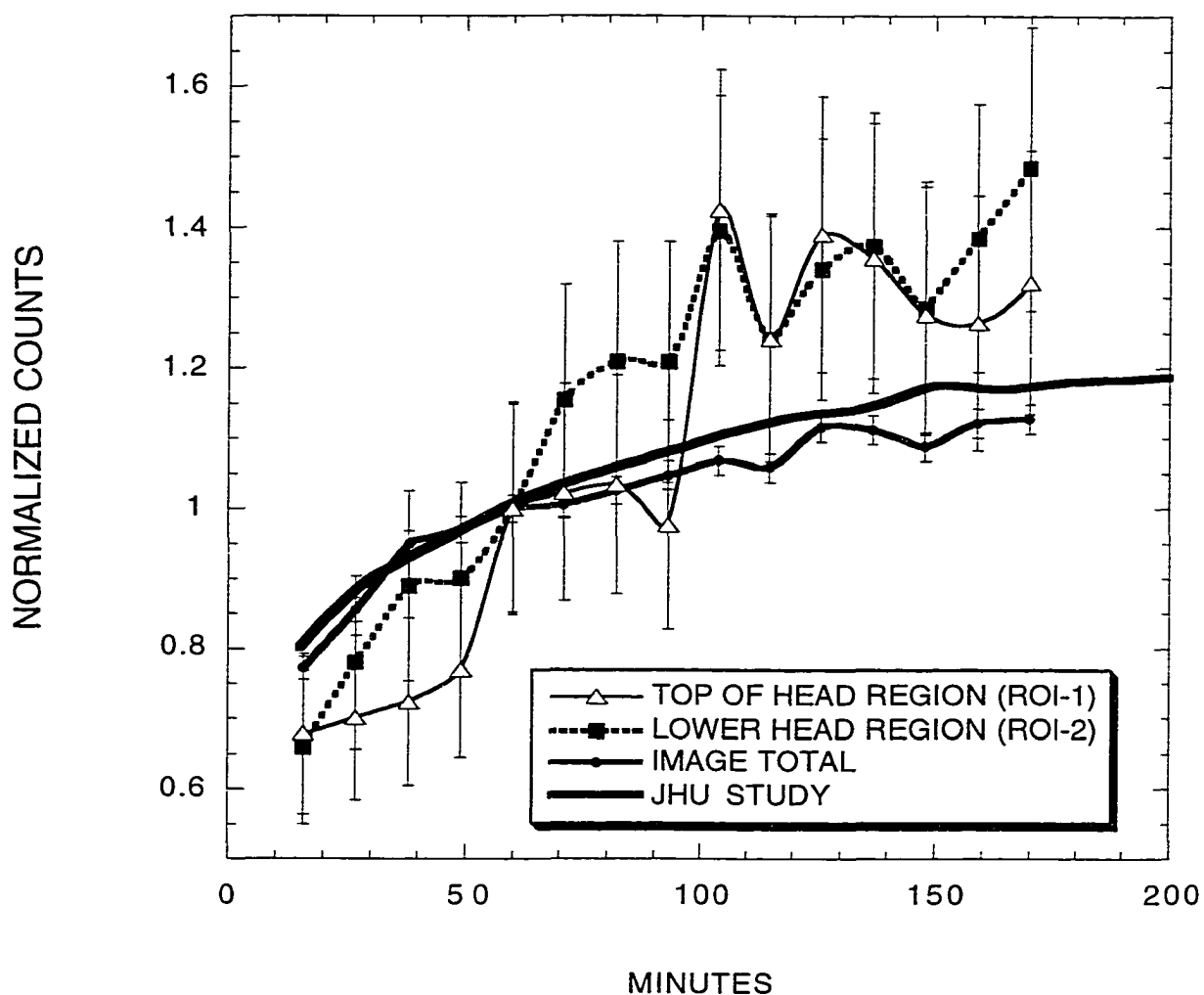


Figure 4.10: Graph of the change over time of the counts of the two head regions and the total image counts plotted with the data reported by the Johns Hopkins University group (JHU). Error bars were determined in the same manner as in the previous plot.

To control for the possibility of the continuously changing availability of RTI-55 as it enters and leaves the field of view of the detector or is removed by metabolic processes (i.e. respiration) the data were also expressed as the ratio of ROI-1 and the total image counts then plotted as a function of time. This is shown in Figure 4.11. The feature seen at about 100 minutes clearly needs further study but it is strongly suggestive of enhanced transport, possibly resulting from the expression and activation of transporters for RTI-55 within the brain.

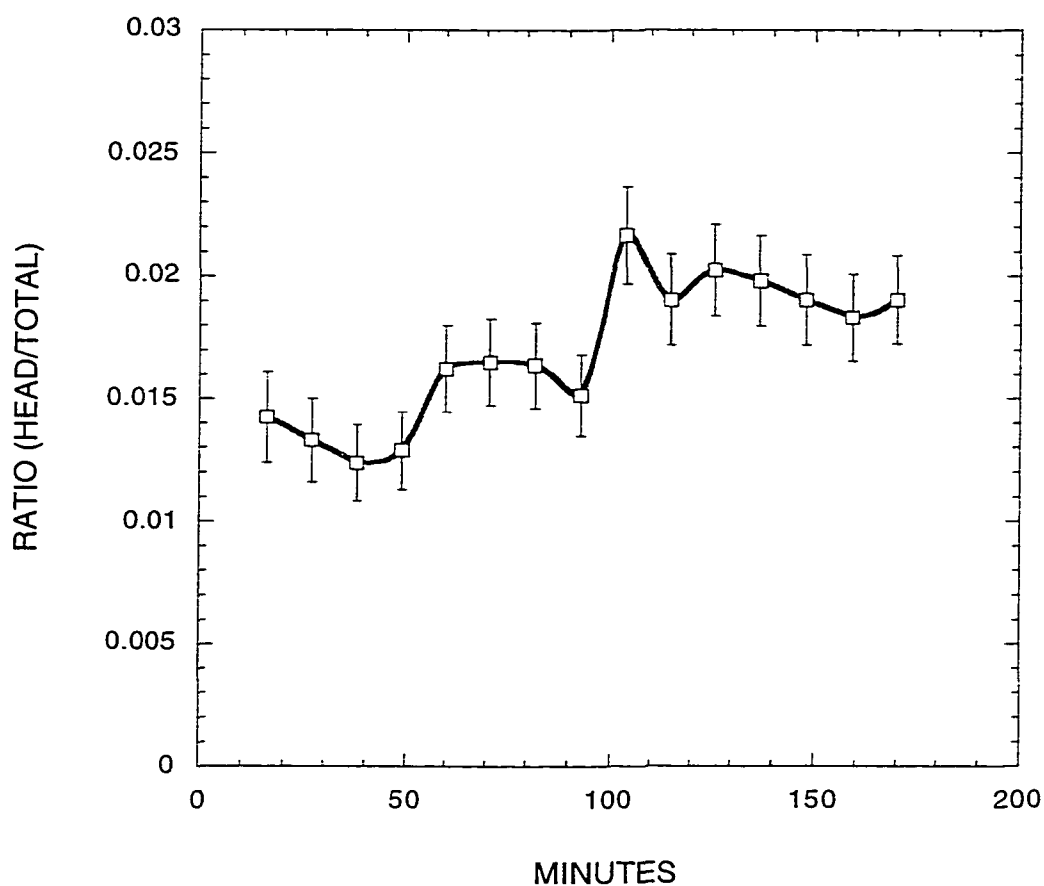


Figure 4.11: Graph of the change over time of the counts in the top head region (ROI-1) divided by the total image counts. Error bars were determined in the same manner as in the previous plot.

4.3 Apparent Brain Accumulation of RTI-55

With the William and Mary detector it was possible to look at multiple regions of uptake and to observe the time course overall nature of the biodistribution. After 2 hours and 45 minutes post injection of RTI-55, the detector was re-positioned to obtain a side-view of the mouse. This image is shown in Figure 4.12 superimposed onto a photograph

of the mouse. The lower image in Figure 4.12 is the accumulated data from the dynamic study and also is shown in Figure 4.4.



Figure 4.12: Images overlaid onto photographs of the experimental mouse. The side-view image was obtained beginning at 2 hours 45 minutes post injection of the RTI-55 and the image data was collected for 25 minutes. The bottom image is the aggregated data from Figure 4.4 and was acquired over a period of 2 hours 40 minutes and started 5 minutes post injection.

These figures illustrate the extensive uptake of RTI-55 in the region of the brain. At the end of the study the mouse was sacrificed and the brain was serially cryosectioned,

mounted on microslides, desiccated, and placed in contact with autoradiographic film. The autoradiographic analysis is currently in process and these results will be published as part of this study.

4.4 Discussion of RTI-55 Results

The William and Mary detector system clearly shows the dynamic nature of the uptake of ^{125}I -labeled RTI-55 in the mouse brain. The results are in general agreement with those reported by others [105]. In the Johns Hopkins [105] study the researchers also measured the effect of RTI-55 binding when other compounds that bind to serotonin and dopamine receptors in mouse brain were also injected. The results obtained here with the William and Mary system but not possible with the Johns Hopkins system indicate that there may be important differences in the rate of RTI-55 accumulation in different regions of the head relative to the liver and the total body. The pattern seen in one brain region but less apparent in another could be more a statistical effect. However, there is the possibility that what is being imaged is a differential ligand saturation phenomena or varying amounts of transport availability. Results indicate the rate of accumulation in the region of the liver may not be different compared with the total counts suggesting the expected brain specific effect of RTI-55. A simultaneous comparative study of several regions of the mouse brain and body will be conducted using a variety of agents known to block RTI-55 transporters and receptors. These studies should contribute significantly to the literature on pharmacokinetics of these compounds.

Chapter 5

Discussion and Future Directions

5.1 Molecular Biology Assays

The CsI(Na) array based position sensitive photomultiplier tube imaging detector system provided high resolution planar images of the biodistribution of ^{125}I in living small animals. We intend to pursue three directions in the future: ^{125}I -labeled ligand studies in mice, ^{125}I -labeled anti-sense RNA research, and incorporation of tomographic capabilities to the existing detector system.

The system is optimized to allow investigation of both the relative distribution of ^{125}I -labeled ligands as well as the change in the distribution over considerable time durations. This detector configuration is also capable of imaging ^{125}I -labeled antisense RNA probes hybridized to unique mRNA that is specific to the expression of particular genes. Hence, the detector system makes it entirely feasible to dynamically image actual gene expression within a discrete region of a small animal subject.

RNA molecules are readily broken down *in vivo* by natural enzymes within the cells. It is therefore necessary to determine how to develop ways to modify RNA molecules designed to act as antisense probes in order to facilitate their retention in living organism. Agrawal et al.[109] have reported progress in this regard using RNA molecules they refer to as mixed backbone oligonucleotides. These modified molecules have phosphorothioate segments at the 3' and 5' ends and a modified oligodeoxynucleotide or oligoribonucleotide segment located in the central portion of the molecule. Work is now in

progress using PET techniques to image very short-lived isotopes used to label RNA. However, such an approach requires research facilities to have their own isotope producing facilities which severely constrains such research to very few centers with accelerator facilities. The ability to image ^{125}I -labeled ligands, including stabilized antisense RNA probes as they are developed, extends to a far greater number of investigators the ability to conduct dynamic *in vivo* gene expression research.

We are currently investigating the optimal parameters for brain imaging of ^{125}I -labeled RTI-55 in order to make our technology available for pharmacodynamic studies of this cocaine analog. In addition to optimizing close administration protocols for RTI-55 we are also exploring the use of other ^{125}I -labeled ligands to investigate this sort of receptor binding interaction. We are planning tests to develop protocols for delivering ^{125}I -labeled oligodeoxynucleotides past the blood brain barrier in an attempt to image gene expression in the brains of live mice using antisense RNA techniques. We will investigate the use of ^{125}I labeled antisense RNA probes to attempt *in vivo* gene expression imaging of genes whose expression patterns are well known in the mouse. Once this is mastered, attempts to image gene expression in the brain will be attempted, first with tail vein injections and then with injections into the cerebral fluid (intracerebroventricularly) of the mouse brain.

We are also making design improvements in the detector system with the addition of an automated rotating gantry, improved sensitivity collimators, and additional imaging and coincident detectors. Presently, a gantry is being tested which allows the manual placement of the detector system at any angle surrounding the mouse under study (Figure 5.1).

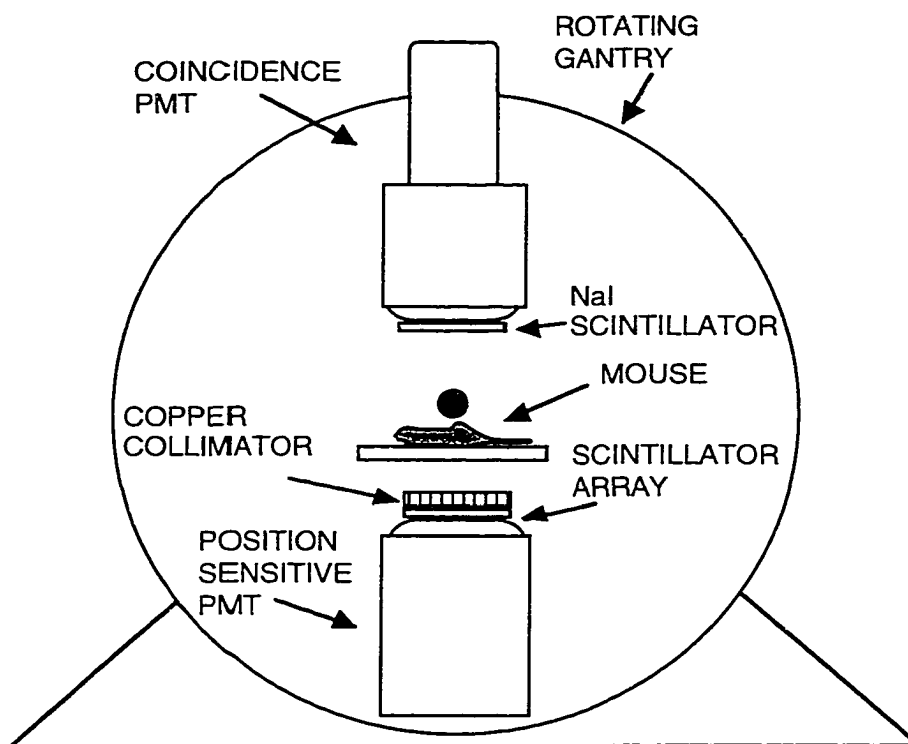


Figure 5.1: A schematic of the gantry to be used to obtain SPECT images

Figure 5.2 is a photograph of the detectors attached to the gantry which will be fitted with a rotation motor. When this computer controlled gantry is complete it will be possible to develop and test tomography reconstruction software based on SPECT and optimized for ^{125}I imaging in small animals.

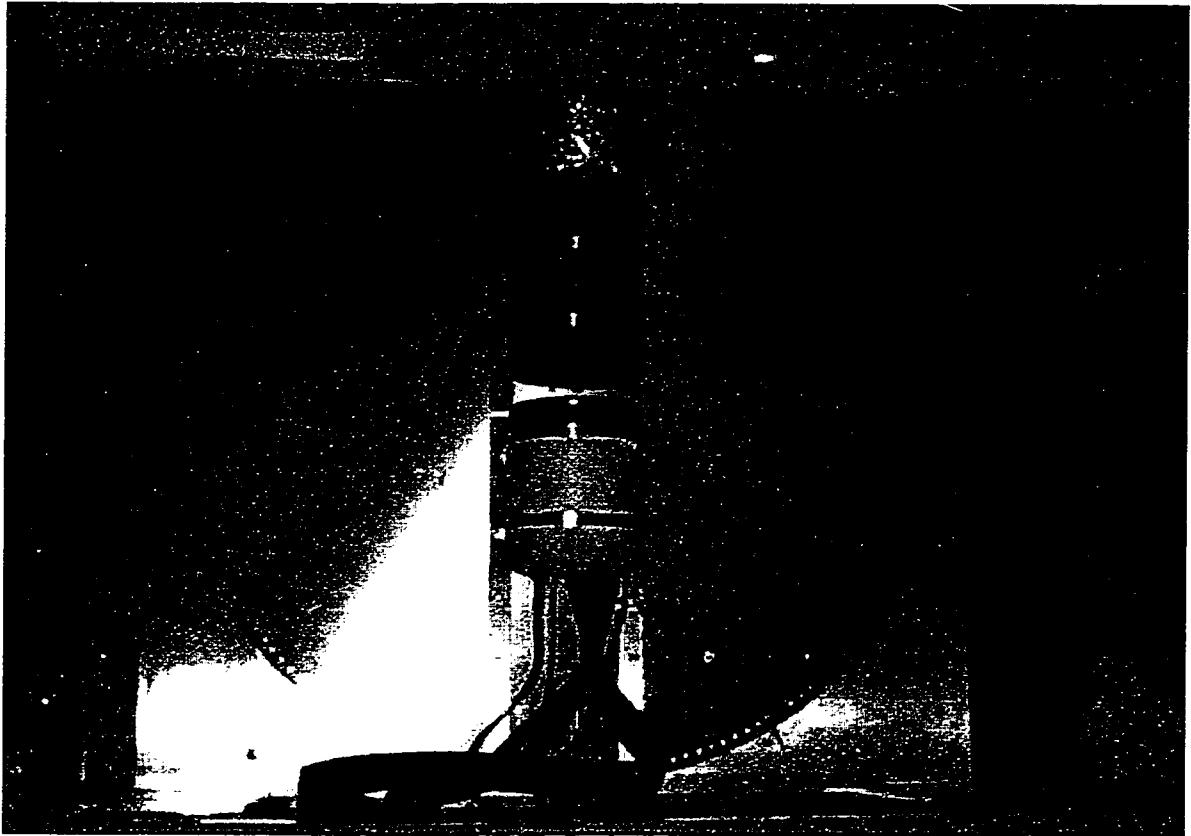


Figure 5.2: A photograph of the detectors mounted in the gantry to be used to obtain SPECT images.

A major drawback of the high resolution copper collimator developed for this detector system is its reduced sensitivity. A high resolution collimator constructed from laminates of etched tungsten will improve the sensitivity of the present detector system. Because of the higher absorption coefficient of tungsten compared to copper (at 35 keV; 292.5 cm^{-1} versus 63.4 cm^{-1} respectively) thinner walled openings can be constructed in the collimator which would result in a 25% improvement in the sensitivity for ^{125}I .

The addition of more imaging detectors will permit the simultaneous acquisition of images from multiple directions which would allow the generation of SPECT reconstruction images in a reasonably short amount of time. Finally, with more coincident

detector surface area surrounding the subject, the efficiency of the coincidence mode of operation will be greatly improved.

5.2 Conclusion

This study successfully applied a position sensitive photomultiplier tube with a CsI(Na) array made from 1 mm x 1 mm size elements and a custom built high resolution collimator constructed from copper-beryllium to image the biodistribution of ^{125}I labeled probes in live small animal subjects. This detector system is now installed on a rotating gantry and is in use for ongoing animal studies in a biological laboratory. This is the first detector system for *in vivo* small animal imaging of ^{125}I that utilizes a 125 mm diameter position sensitive photomultiplier tube coupled to a scintillating crystal array composed of 1 mm x 1 mm size pixel elements and able to achieve less than 2 mm spatial resolution FWHM. Researchers at the University of Virginia [110], Johns Hopkins University [111], and Weizmann Institute [112] have requested access to the technology developed in this project for various *in vivo* molecular imaging applications at their institutions.

Appendix A.

Molecular Biology Background

The goal of the project described in this thesis is to provide an imaging tool for live small animal research that uses molecules such as peptides and oligonucleotides which can be easily obtained or labeled with ^{125}I . The purpose of this appendix is to provide background material regarding molecular biology techniques that are relevant to the detector system described in this dissertation. More complete treatments of much of the molecular biology theory and techniques contained in this appendix can be found in the books by Watson et al. [113] and Lewin [114] from which much of this appendix was drawn.

A.1 Molecular Biology Theory: The “Central Dogma”

The “Central Dogma” describes the basic tenet of gene expression which is that genetic information contained in the double stranded DNA molecules in the chromosomes of cells is transcribed into another type of nucleic acid called ribonucleic acid (RNA). The genes of an organism contain the information necessary for the reproduction of the organism and for the development, growth and maintenance of all the cells that make up the organism.

A.1.1 DNA

The instructions necessary for directing the cell to construct particular proteins are contained in deoxyribonucleic acid (DNA), which is a long double helix formed from two anti-parallel polymers. The molecule is made of three parts: a five carbon deoxyribose sugar (a ribose sugar with a hydrogen atom missing from its 2' carbon of its five carbon ring), a phosphate group (PO_4) and one of four organic nitrogen containing bases: adenine (A), thymine (T), guanine (G) and cytosine (C) that are the base units which compose DNA sequences. The two ends of a single strand DNA molecule are characterized by referring to the end which is adjacent to the 5' carbon of the five-carbon sugar ring versus the opposite end 3' carbon. Along the DNA coding strand three contiguous nucleic acid bases (codons) code for an amino acid. A given amino acid can be specified by one to six different codons. A double stranded DNA molecule (the double helix) is made by the binding of adenines to thymines and cytosines to guanines.

A.1.2 RNA

DNA is transcribed into mRNA which are single strand molecular polymers. RNA (ribonucleic acid) is similar to DNA except that the nucleic acid uracil (U) replaces the thymine (T) which is found in DNA. RNA is a nucleic acid made of three parts: a five carbon sugar, a phosphate group (PO_4) and an organic nitrogen containing base. The enzyme, RNA polymerase, transcribes the DNA sequence by synthesizing an RNA template based on the DNA coding strand. This is illustrated in Figure A.1.

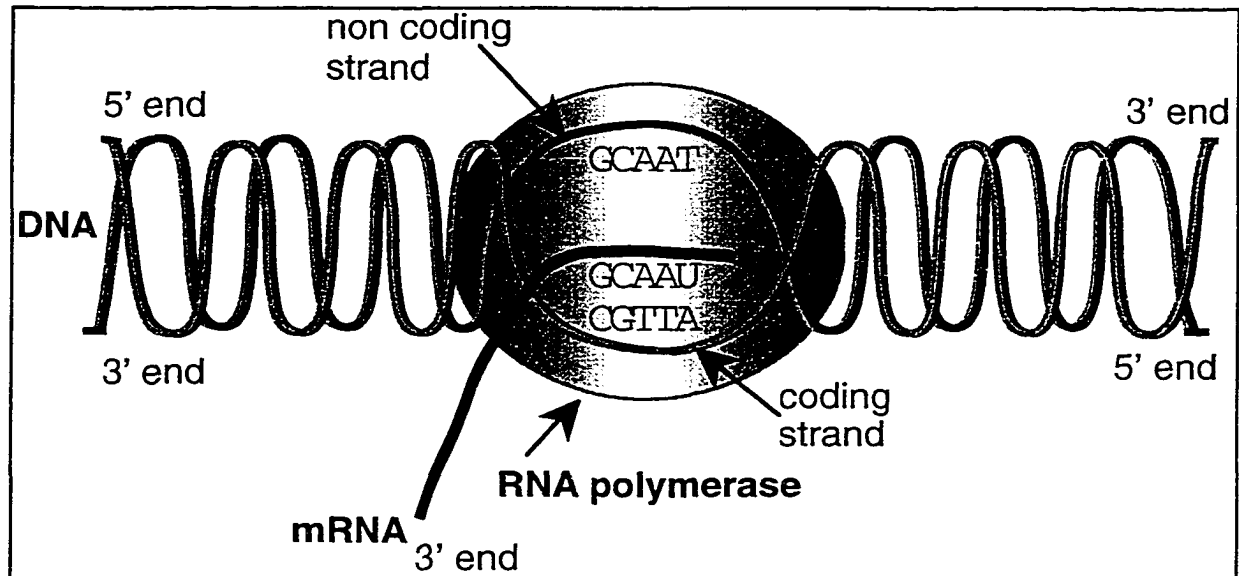


Figure A.1: The process of transcription from DNA to mRNA by the enzyme RNA polymerase.

RNA is found in three forms in a cell: ribosomal RNA, transfer RNA (tRNA) and messenger RNA (mRNA). Messenger RNA is translated into a protein by a biochemical process carried out by ribosomes. Ribosomes are large RNA complexes which “read” the sequence of bases in the mRNA, three bases at a time. This three base “word” is called a codon. The gene’s protein information contained in the sequence of codons in the mRNA is translated into a protein using transfer RNA (tRNA) as the molecular vehicle to concatenate the appropriate amino acids coded by a codon being read from the mRNA by the ribosome. This is shown in Figure A.2. The spent tRNA later gets “re-charged” with its particular amino acid. The mechanisms regulating gene expression are the focus of many on going molecular biology research endeavors.

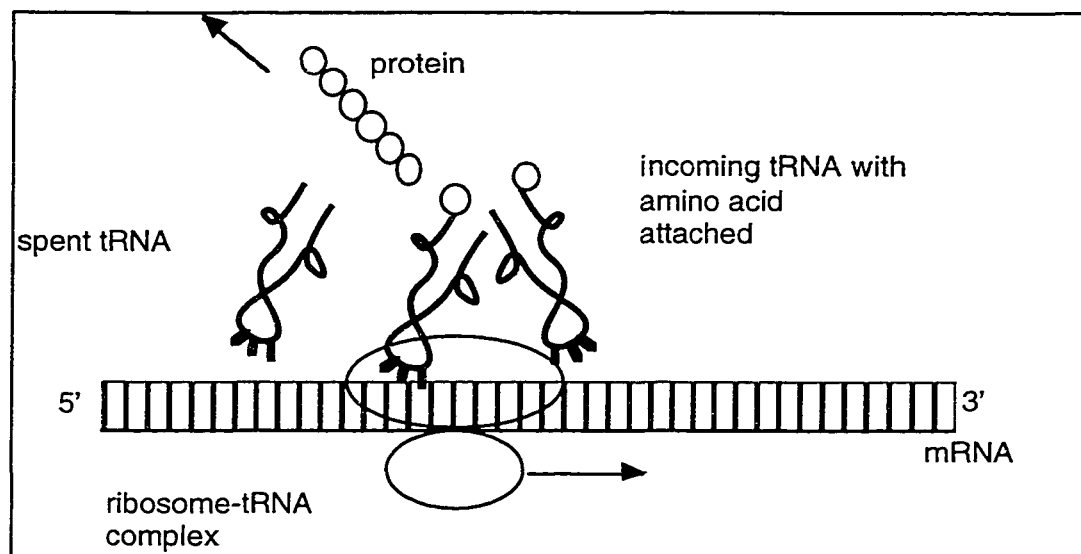


Figure A.2. Translation of mRNA into a polypeptide chain by ribosomes.

A.1.3 Protein Formation

The information contained in the base sequences of a mRNA molecule is translated into a protein by linking together various combinations of twenty possible amino acids. This process is different between prokaryotic cells (bacterial cells) and eukaryotic cells (animal cells). In eukaryotic cells the transcription of the gene from DNA to a pre-mRNA occurs in the nucleus of the cell. The pre-mRNA undergoes modification such that non-coding regions (introns) are removed, leaving only coding regions (exons) that are then spliced together to form a mature mRNA transcript. At the boundaries between introns and exons in pre-mRNA are specific base sequences which are recognized as splice points for specific enzymes in the nucleus called endonucleases. This mRNA molecule is transported out of the nucleus through a transmembrane port. Once in the cytoplasm, the mRNA is then translated into a chained sequence of amino acids that, when completed, is the resultant protein molecule. These proteins have myriad biochemical and structural roles including, for example, serving as enzymes, ligands, or transmembrane receptors. See Figure A.3 for a diagram summarizing the steps outlined above.

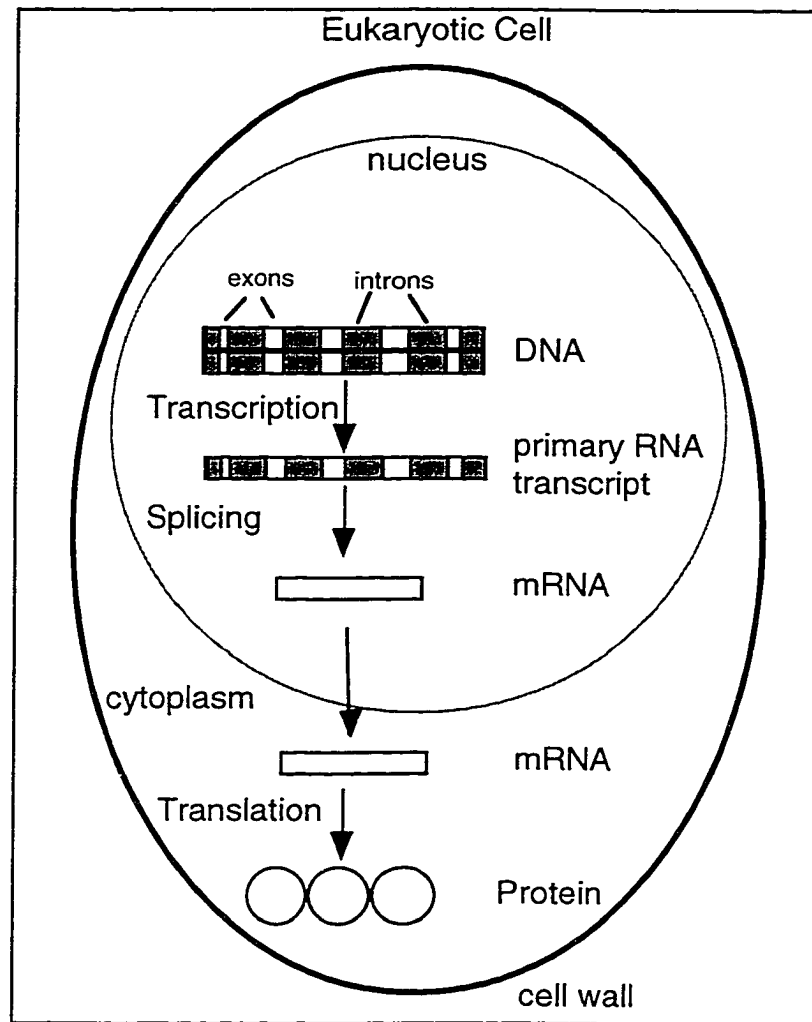


Figure A.3: The sequence of transcription from DNA to mRNA then to a polypeptide chain (protein) via translation for eukaryotic cells.

A major class of proteins known as enzymes act as biological catalysts and are used within the cell to facilitate specific chemical reactions that are needed by the cell. Another type of protein is called a receptor. Receptor molecules are proteins that function as molecular information transducers positioned within the cell plasma membranes or interior. Transmembrane proteins have a portion lying within the cytoplasm, with one portion protruding outside the cell in a manner that permits signaling ligand molecules outside the

cell to bind to it. A whole sequence of biological actions called a “signaling cascade” can result from a specific molecule (the ligand) binding to an appropriate receptor.

A.1.4 Post Translational Modification

After a protein is assembled by ribosome through linking together combinations of twenty possible amino acids various post translational modification of one or more of the original amino acids can occur. These modifications change the properties of certain amino acids in the protein which can affect the protein’s function. Some common modifications consist of the addition of small molecular groups to a specific amino acid already part of the protein.

Phosphorylation is one such modification process in which a phosphate group is added to the hydroxyl group of one of the amino acids (i.e. serine). The phosphate group which has a net negative charge, changes the electrostatic properties of the protein after the addition. Other possible post-translational modifications are acetylation and methylation. Modifications that involve the covalent addition or removal of groups to and from proteins require specific enzymes. For instance, kinases are enzymes that covalently add groups to the amino acids tyrosine, serine and threonine, while phosphatases remove them. Protein kinases play an important role in post translational modification of different proteins that participate in various intercellular and intracellular signaling (i.e. receptors). Proteins can also be modified such that a carbohydrate side-chain is added to an amino acid forming a glycoprotein.

A.2 Molecular Biology Techniques

Following are descriptions of available molecular biology techniques with relevance to *in vivo* animal studies. One of the basic investigative goals of molecular biology research is the understanding of the roles individual genes have in the all stages of life of an organism. To achieve this goal, researchers need to identify and isolate individual genes of interest and to study the role their products have on other biological systems in that organism. Of great interest are the chemical signaling roles of various molecules called ligands which will bind to specific cell membrane bound protein molecules called receptors which can generate a cascade of biochemical reactions. Methods to detect specific sequences of genes and to detect the presence of specific proteins have been developed and provide an essential tool for molecular biology research.

A.2.1 Making a Recombinant Molecule

The discovery of various special enzymes called restriction enzymes that cut DNA molecules at sites of specific sequence of bases make it possible to recombine, and therefore study and analyze genes. This technology referred to as recombinant DNA makes it possible to modify existing genes in a live organism thus making it possible to determine function.

A.2.1.1 Restriction Enzymes and Ligases

Restriction enzymes cleave lengths of DNA molecules at locations of a specific sequence of bases on the molecule known as restriction sites. For instance the restriction enzyme Eco RI will only cut at the sequence of bases GAATTC, see Figure A.4.

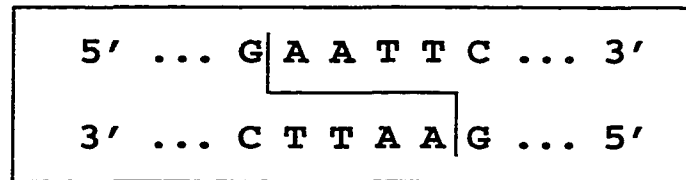


Figure A.4: Restriction site in a DNA molecule for the restriction enzyme Eco RI.

Over 150 restriction enzymes that cut specific sequences of DNA have been isolated from several hundred strains of bacteria. Restriction enzymes are named after the bacteria from which they were isolated (for instance *Escherichia coli* for Eco RI). By using different restriction enzymes it is possible to fragment isolated DNA chains and separate the fragments through a technique termed agarose gel electrophoresis. Electrophoresis separates by size a collection of DNA fragments (DNA has a net negative charge) by moving DNA fragments which have denatured (split into two single strands) through the matrix of an agarose gel by using an applied electric field. The larger fragments will move slower, hence translating a shorter distance than the smaller fragments.

Other enzymes called DNA ligases are used to ligate or combine DNA chains together. Thus it is possible to isolate a gene of interest by having knowledge of its sequence and by choosing various restriction enzymes to extract it from a long DNA molecule. With restriction enzymes and DNA ligases it is possible to insert and recombine a fragment of DNA into a specific location in a host DNA molecule.

A.2.1.2 Vectors

Specially designed molecules that are used to insert genes into a host organism are called vectors. Vectors are often used to transfer the foreign gene into a bacteria cell which then replicates thus making several hundred to several thousand copies of the gene of interest. This is done to generate a sufficient number of copies to facilitate analysis.

Bacterial plasmids and bacteriophages (viruses that multiply in bacteria) are two possible vectors.

Bacterial plasmids are small, self replicating, circular pieces of extrachromosomal DNA that are used by bacteria to carry antibiotic-resistance genes. Bacteriophages, also called phages, are bacterial viruses that undergo rapid replication inside host bacteria. Specifically modified plasmids and phages are commercially available, allowing researchers to insert genes of interest by using various restriction enzymes to cut open the plasmid or phage DNA to allow insertion of the desired sequence. A typical plasmid vector carries an antibiotic-resistance gene that can be used to screen for bacteria that only have the plasmid the researcher has introduced (transfected) into a sample of bacteria. In addition, the plasmid has a restriction-site within the *lacZ'* gene. *LacZ'* encodes the β -galactosidase protein which catalyzes a blue color reaction in contact with a compound called X-gal. The compound X-gal is added to the nutrient medium (agar) used in culture plates used to grow the transfected bacteria containing the plasmid. This determines if the foreign gene insert is present. If the foreign gene was inserted into the plasmid, then the β -galactosidase gene is interrupted and not expressed and only the foreign gene is expressed. Therefore, the bacteria do not turn blue.

The phage vector is a linear region of virus DNA that has restriction sites for the several restriction enzymes (i.e. Eco RI) . In this way the researcher can insert the gene of interest to make multiple copies by infecting a host bacteria that has been previously grown on an agar culture plate. Figure A.5 is an illustration of a plasmid and phage vector.

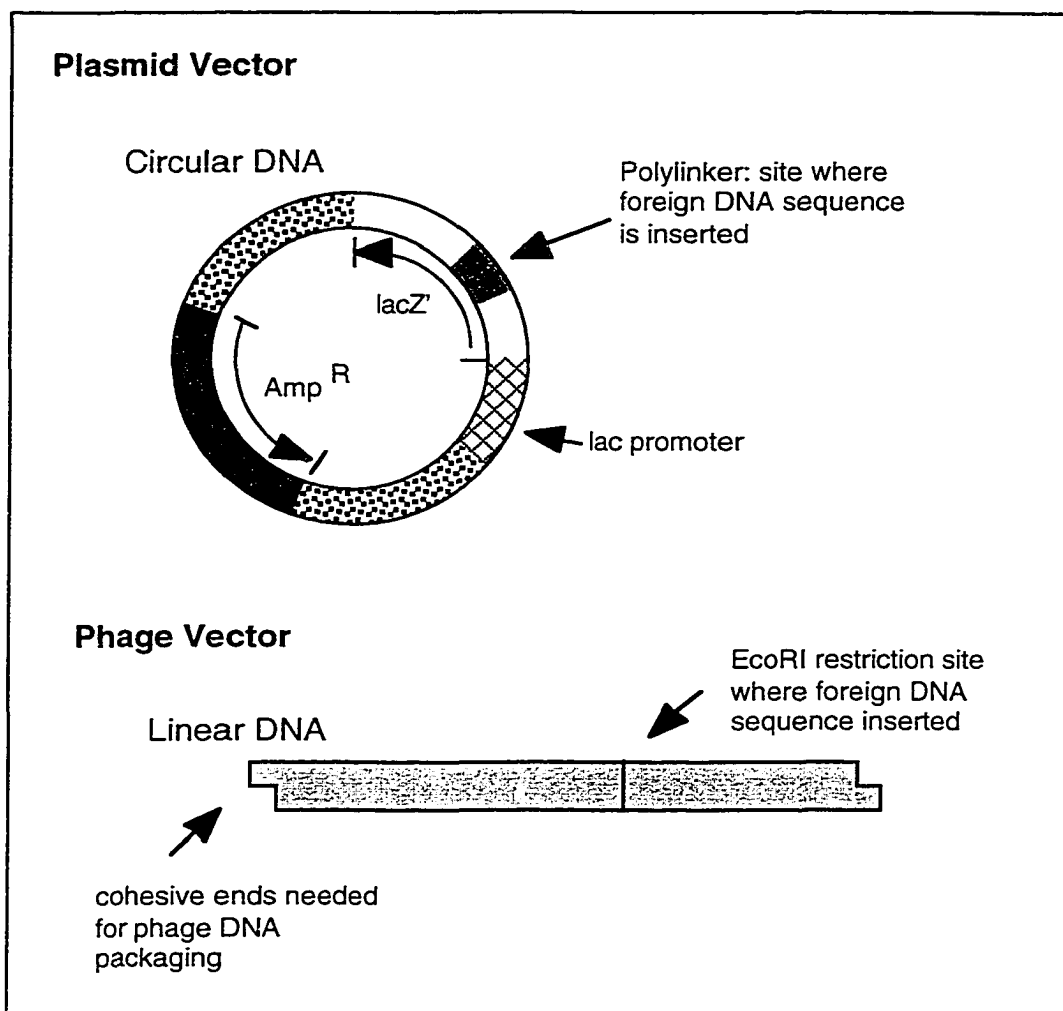


Figure A.5: Example of two vectors. The plasmid vector illustrates how the gene lac Z' was inserted into the plasmid along with a region (polylinker) containing many sites into which a foreign DNA sequence can be spliced. The phage vector illustrates a linear region of a virus genome that has a restriction site for the Eco RI restriction enzyme.

A.2.2 cDNA Libraries and Genomic Libraries

There are two strategies used to isolate or clone a gene to allow it to be studied. The first uses the polymerase chain reaction (PCR) screening technique to amplify, isolate, and clone genes of interest from a small amount of the target organism's DNA. In PCR, one uses short flanking DNA sequences known as primers that are similar to or related to

the DNA sequence of the gene being sought. For instance, a researcher could choose to use specific primer sequences to isolate sequences of endogenous retroviruses.

The second method is library screening. There are two types of libraries that can be screened: genomic libraries and complementary DNA (cDNA) libraries. A genomic library theoretically contains all the genes in the DNA in the chromosomes (the genome) of an organism. It is therefore possible for genomic libraries to contain all of the DNA sequences that make up the genome of the organism. Complementary DNA is a DNA copy of an mRNA molecule. A cDNA library is obtained by using an enzyme called reverse transcriptase to reverse transcribe all mRNA extracted from a given tissue. The library will contain only expressed genes.

There are two ways to screen libraries. The first is referred to as homology screening which uses a probe with complementary sequences (homologous) to a gene being sought. The second method, called selected or dissected screening is used if the researcher is searching for the expression of genes similar to a known gene but at selected particular times of an embryo's development or in specific dissected tissue samples. In this case, libraries constructed from a selected stage of development or from a specific dissected tissue of the organism is obtained and screening with a probe made of fragments of sequences of a known gene.

A.2.3 Analyzing Transcription

There are several techniques available for analyzing and visualizing a specific transcribed RNA fragment out of many contaminating molecules in order to study the manner of transcription of a gene. These techniques are used to determine how a particular gene is being transcribed under various circumstances. For instance, various techniques are available if one is trying to determine at what stage of embryonic development a particular gene of interest is being expressed or how certain molecules known as

transcription factors are involved in the regulation of transcription of a particular gene. Such methods as Northern blotting, Rnase Protection Assays (RPA), *in situ* hybridization, and promoter activity studies are used to analyze gene transcription.

A.2.3.1 Northern Blotting

The Northern blotting technique is used to analyze a sample of mRNA that has been extracted from a cell line or tissue. First, mRNA is isolated from the cells through extraction methods and are loaded into narrow slots (~0.5 cm) which define lanes for mRNA on an agarose gel to be separated by size using electrophoresis resulting in lanes 0.5 cm wide and possibly extending the length of the gel which are smears of mRNA. An additional lane size markers can also be loaded on the electrophoresis gel to provide an indication of the size of the mRNA molecules. After electrophoresis separates the mRNA by size a replica of the pattern is made by placing nylon filter paper on the gel and using paper towels to wick a buffer solution through the gel which acts to transfer the mRNA fragments from the gel to the overlaying filter paper. These mRNA fragments then bind to the filter paper. In this way the mRNA fragments are transferred to the filter paper. The filter paper is then allowed to hybridize with a radioactively labeled probe (usually ^{32}P) that is complementary to the mRNA under study. The filter paper is then washed with a buffer to remove unbound probe.

Autoradiographic film is then placed on the filter paper for a period of time (hours to weeks) and after developing the film, the presence and size of the desired RNA is found, if it exists at all. The relative density of the image of the hybridized probe also gives an estimate of the amount of that RNA fragment that was present. This technique could be used on samples of RNA extracts from cells of a embryo at three different stages of development to test for the transcription of a particular gene of interest.

A.2.3.2 RNase Protection Assays

In the situation where a more accurate determination of the amount of a particular sequence of mRNA present in a sample of extracted mRNA is desired the RNase protection assay (RPA) technique is used. With this technique a chemical synthesis method is used to generate a sequence of antisense RNA that is complementary to a fragment of the target mRNA. During the chemical synthesis of the antisense sequence a radioactive label is incorporated into the probe. The antisense RNA probe is combined with a sample of isolated mRNA and permitted enough time to hybridize to complement mRNA. Since the antisense RNA probe is a fragment the duplex formed by the mRNA-antisense RNA hybrid, there will be overhanging single stands of mRNA. At this point an enzyme is added (RNase) which digests any single RNA strands, and the mixture precipitated to remove any unhybridized RNA. The precipitate is loaded onto a electrophoresis gel which has a denaturing agent incorporated into it which separates the double strand duplexes into single strands to permit the electrophoresis to function properly so as to visualize the “protected” band. The gel is then exposed to autoradiographic film and the fragment mRNA will be seen if hybridization took place. Since the nonspecific probe is digested away a very accurate determination of the quantity of the RNA present is possible.

A.2.3.3 In Situ Hybridization

In situ hybridization assays also use labeled probes to determine the presence of a target mRNA indicating the transcription of a gene. With *in situ* hybridization the probe is allowed to hybridize to the target mRNA in the actual tissue sample or even whole organism (i.e. an embryo). For instance, a complete *Xenopus* embryo (a species of frog) is chemically treated to fix it, and prepare it for a mRNA probe. The embryo is treated and washed several times to remove all the protein matrix and other tissue to make it receptive to a mRNA probe. Typically a color marker is used such that when the probe hybridizes to

its complement it turns blue thus staining the region of the embryo which is expressing the mRNA being studied. This technique is called whole mount *in situ* hybridization.

A similar technique called section-mount, *in situ* hybridization is used with larger subjects such as mice and rats in assays involving paper thin slices of tissue samples of the organism that has been sacrificed. The visualization of the binding of the probe is achieved either with visible staining for the case using visible dyes or with UV light for the case of the fluorescent dyes. For detection using autoradiographic film, probes are labeled with radioactive isotopes of phosphorus (^{32}P), carbon (^{12}C), sulfur (^{35}S), hydrogen (^3H), or iodine (^{125}I). With these techniques it is possible to visualize in the subject the locations of the expression of the gene of interest. The shortcoming with these techniques is that the subject needs to be sacrificed and long film exposure times are often required in order to detect a weak signal. The detector system described in this dissertation could conceivably make it possible to do *in situ* hybridization with a live animal in real-time.

A.2.3.3 Analysis of Promoter Activity

There are specific sequence motifs upstream (in the 5' direction) and downstream (in the 3' direction) of the actual start site of transcription that are responsible for the regulation of gene expression. An important sequence of bases is termed the promoter which is a specific combination of bases that serve as sites where RNA polymerase binds in order to commence transcription. The promoter is a region in DNA that acts as a protein binding site which controls transcription of the gene to RNA by the enzyme RNA polymerase. If, because of mutation, the promoter is missing, this gene will not be expressed. Even minor mutations in the promoter can influence the expression of the gene.

In addition to the promoter, there are other sequences of bases which have been found to enhance the transcription of the gene into RNA; these sequence are termed

enhancers which can also reside downstream. Figure A.6 is a diagram illustrating the basic structure of a eukaryotic protein gene.

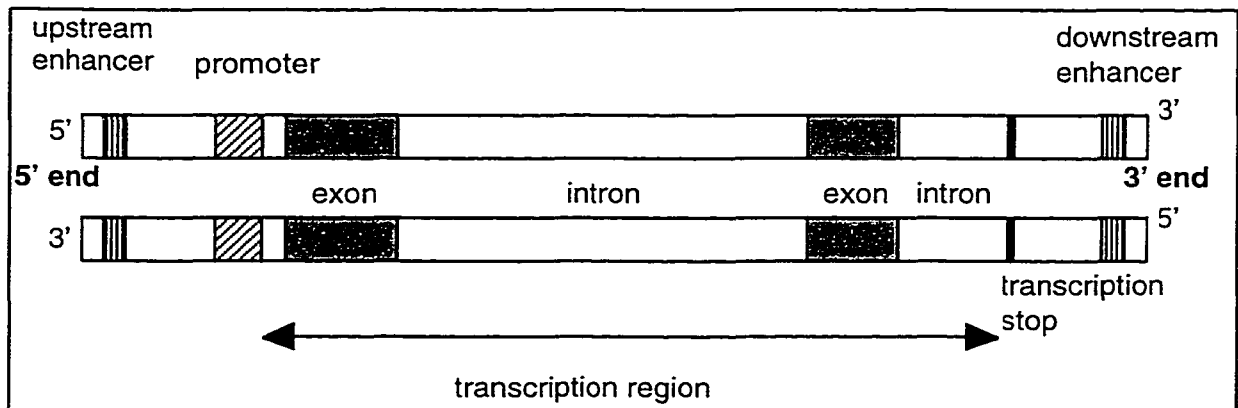


Figure A.6: Basic structure of a eukaryotic gene which codes for a protein. The start of the transcription of the gene into pre-mRNA follows the promoter region. Further upstream and down stream of the gene are enhancer regions which also are involved in gene expression regulation

It is possible to induce small mutations in the series of sequence of DNA that are part of or near the promoter. This is done to determine which sequences are the ones necessary for promoter activity and thus leading to transcription of that gene. Once the promoter is well understood this same promoter can be used with a special gene called a reporter gene (discussed later) to study the function of a gene particularly *in vivo*.

A.2.4 Analyzing Proteins

Western blotting, immunocytochemistry, and ligand binding assays are three techniques that are used to analyze proteins. Western blotting is used to analyze proteins *in vitro* in a manner similar to Northern blotting analysis of mRNA. Immunocytochemistry and ligand binding refer to protein visualization techniques that can be used *in vitro* as well as *in vivo*.

A.2.4.1 Western Blotting

Western blotting uses color labeled antibodies to visualize a target protein (antigen) within a collection of other extracted cellular proteins. The technique is similar to Northern blotting except that the proteins are loaded onto a different type of gel (SDS-polyacrylamide). This is a useful technique to check for the presence of proteins that are expressed by a gene that is being studied. Monoclonal antibodies are used to bind to one type of antigen while polyclonal antibodies will bind to a class of antigens.

A.2.4.2 Immunocytochemistry

The immunocytochemistry technique uses color or radioactively labeled antibodies that are used to visualize a target protein (antigen) *in vitro* or in a live animal. A subject can be injected with the color labeled antibody and then sacrificed and section mounted in thin slices onto slides. For the cases where radioactive labels are used the slides are placed in contact with autoradiographic film. The film and slide are kept in contact for as short as a few hours but are often kept in contact for as long as several weeks. This technique has been using medical imaging devices for human and large animal studies. This technique will benefit from the detector system described in this dissertation since many commercially available antibodies are labeled with ^{125}I .

A.2.4.3 Ligand Binding

Ligand binding assays use radioactively labeled ligands to bind to specific protein molecules termed receptors. Similar to immunocytochemistry, a subject is injected with the radioactively labeled ligand, sacrificed, and section mounted in thin slices onto slides and placed in contact with autoradiographic film. As mentioned earlier, receptor molecules function as information transducers positioned within the cell plasma membranes or interior. Cell surface proteins which will bind ligands are termed transmembrane proteins

and, as mentioned before, have a portion lying within the cytoplasm and a portion outside the cell in a manner that allows the signaling ligand molecule outside the cell to bind to it. This visualization technique also has been using medical imaging devices for human and large animal studies and recently with small animals. This technique will also be advanced by the detector system described in this dissertation since many commercially available ligands are labeled with ^{125}I .

A.2.5 Analyzing Gene Function

Once a particular gene is isolated through various methods, its various roles in an organism can be studied by introducing an altered version back into the organism and observing their action *in vivo*. Techniques have been developed that allow one to replace an endogenous gene with an altered version. Examples of these techniques are homologous recombination, transgenics and reporter genes.

A.2.5.1 Homologous Recombination

Gene targeting can be achieved by using a vector that has sequences that are nearly the same or homologous to the target sequence. Integration into the actual gene is targeted by cutting the circular plasmid to make it a linear molecule. The two ends will integrate preferentially (recombine) into the chromosomal sequence of the host which is homologous to the free ends of the linearized plasmid. In this way the researcher is actually able to insert a sequence into the DNA of a host cell.

To completely replace or knock out the target gene or its promoter with the sequence contained in the plasmid, a plasmid is made with two free ends that are homologous to sequences flanking the gene to be knocked out. In addition, several copies of a gene with the appropriate enhancer-promoter sequences can be integrated to result in an over expression of the gene of interest, thus multiplying its effect in an organism.

A.2.5.2 Transgenics

Transgenics is the technique used to alter genes of a developing embryo and to introduce foreign genes (transgenes) into embryos of a host organism. It is possible to transform foreign genes in mice by injecting the gene of interest into a pronucleus of a recently fertilized egg. A newly fertilized egg has two pronuclei, one from the ovum and one from the sperm. The injected eggs are transferred to a foster mother and the presence of the transgene can be detected using various methods on DNA extracted from the offspring. If one wants to have the foreign gene inserted into a specific place in the genome then homologous sequences of the locus of interest are made to flank the foreign gene to be inserted using the homologous recombination technique. The function of this gene can be studied as the mouse develops. It is even possible to integrate foreign DNA into germ line cells of a mouse thus passing the gene onto the offspring of the host mouse.

A.2.5.3 Reporter Genes

With homologous recombination methods one can introduce a reporter gene into an organism to indicate the expression of the gene being studied. In this case a gene construct is engineered as in the transgene method. A reporter gene carrying the promoter sequence of the gene of interest is carried in a vector with the exact sequences to a region of the genome into which the reporter gene is to be introduced. The desired result is that the reporter gene will be expressed whenever the promoter of the gene of interest is activated. It is possible to develop a transgenic cell line and even whole organisms which will have the reporter gene passed onto its offspring. To detect the expression of the reporter gene, one then designs a gene probe to either bind (hybridize) to the reporter gene's mRNA or to its protein product by way of a labeled antibody probe. A schematic diagram to illustrate this concept of the reporter gene technique is shown in Figure A.7.

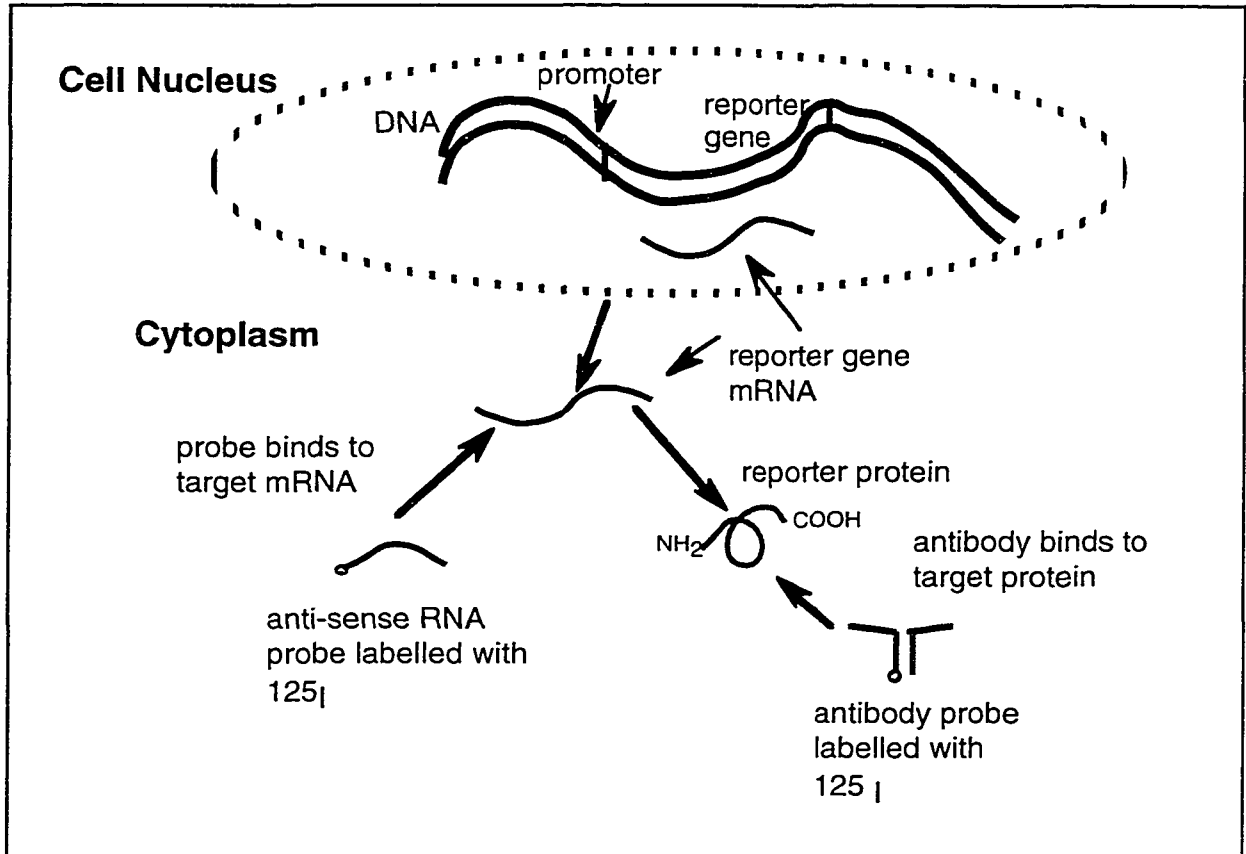


Figure A.7: Schematic of reporter gene technique. A reporter gene with the promoter of the gene of interest has been made part of the genome of the organism. When the gene of interest is expressed so is the reporter gene. The figure illustrates two ways to detect the expression of the reporter gene. One method uses a probe for the mRNA of the report gene the other use immunoassays that use a labeled antibody to the protein coded for by the reporter gene.

In the figure, ^{125}I is the radioactive probe that labels the antibody probe. It is also possible to use an RNA antisense probe labeled with a radioactive isotope to bind to the mRNA of the reporter gene.

A.2.5.4 *In Vivo* Gene Imaging

There are three direct means of imaging gene expression and regulation *in vivo*. Two methods reviewed by Taubes [115] and Gura [116] make use of visible light. The first method uses a reporter gene which codes a protein first isolated from a jellyfish called a green fluorescent protein (GFP). The detection of the expression of this gene is confirmed by viewing the specimen when it is illuminate with UV light. The second method incorporates a reporter gene which codes for luciferase, which is the compound that allows fireflies to glow. When the reporter gene is expressed, light is emitted without the need of a UV light source to cause fluorescence. Both of these methods require that the gene that is being expressed exist near the surface of the animal or is used in transparent animals. Moreover, both of these methods require a large investment in time and experience in breeding a transgenic animal which has the reporter gene and only one gene per transgenic is possible

The third method is the “antisense” technique. This method uses a probe which uses a chain of nucleotides that is the match to a sought-after mRNA molecule transcribed when the gene of interest is being expressed. An antisense molecule to the target RNA molecule is labeled with a gamma-ray or x-ray emitting radioactive isotope. When a detectable amount of labeled antisense RNA molecule binds to enough target RNA the biodistribution of that gene expression can be determined by using a medical type gamma camera.

A.3 Molecular Biology Conclusion

Various molecular biology research techniques have been discussed. The detector system described in body of this dissertation provides a tool which will allow researchers to explore the possibility of imaging gene expression in mice *in vivo*. It is possible to obtain from a commercial source ¹²⁵I labeled antibodies, ligands, and antisense probes.

The detector system developed here fills the need for a high resolution radiation imaging detector that is optimized for ^{125}I detection and mouse imaging.

Appendix B

Radiation Detector Principles

The goal of this thesis was to develop a detector technology which could generate images of the distribution of a radioactive substance in a live animal. To aid biological research involving mice, the detector imaging technology needs to possess a spatial resolution able to resolve structures on the order of two millimeters. To accomplish this goal, radiation detector principles commonly used in particle physics detection were employed. In this appendix, detector physics principles that are pertinent to this project will be described. An excellent text which deals extensively with detector physics is Knoll's *Radiation Detection and Measurement* [17]. For a thorough treatment of radioactive decay, radiochemistry and applications the text *Radiochemistry and Nuclear Methods of Analysis* by Ehman and Vance [117] is an excellent source.

The substances to be detected and imaged are radioactive. The nature of radioactive decay will now be described and the various ways of measuring and describing radioactivity will be discussed. The nature of high energy particle detection by materials called scintillators coupled with very sensitive light detectors will be explained.

B.1 Radioactive Decay

Atomic and nuclear processes resulting from radioactive decay give rise to the emission of charged or uncharged particulate radiation. Radioactivity, discovered by the

French scientist Antoine Henri Becquerel in 1896, is a physical process in which the isotope of an atom is unstable and over time undergoes nuclear rearrangements. These rearrangements result in new isotopes and the emission of charged and uncharged particulate radiation. The charged particulate radiation is either electrons or heavy charged particles. The uncharged radiation is composed of photons (x-rays and gamma-rays) or neutrons. Three properties of radioactive isotopes: activity, type of emitted particles, and the energy of the emissions distinguish radioactive isotopes from each other.

The activity (a) or strength of a radioactive isotope is defined as the rate of decay over time of the number of parent nuclide. The activity (a) of a source is dependent on the amount of radioactive material contained in the sample and can be characterized by the following mathematical relations :

activity is defined as:
$$a = \frac{dN}{dt} = \lambda N$$

where N is the number of radioactive nuclei and λ is the decay constant.

The above integrates to:

$$N = N_0 e^{-\lambda t} .$$

Since $a = \lambda N$, it follows that:

$$a = a_0 e^{-\lambda t} \tag{B.1}$$

where $a_0 = \lambda N_0$.

The activity (a) is often given the units of disintegrations per second (dps). The unit bequerel (Bq) is equal to 1 dps and the unit curie (Ci) is defined as 3.7×10^{10} dps therefore:

$$1 \text{ Bq} = 2.703 \times 10^{-11} \text{ Ci.}$$

The time needed for half the starting number of atoms (or starting activity) to decay is referred to as the radioactive half-life ($t_{1/2}$) which can be expressed in terms of the decay constant:

$$t_{1/2} = 0.693/\lambda. \quad (\text{B.2})$$

The measure of radioactivity per unit mass for a given pure radioactive source is referred to as specific activity and can be described by the following equation:

$$\text{specific activity} = \frac{\lambda N}{NM/A_V} \quad (\text{B.3})$$

where:

M is the molecular weight of the sample, and

A_V is Avogadro's number = 6.2×10^{23} atoms/mole.

The energy of the emissions caused by radioactive decay is given in units of electron volt (eV). One electron volt is defined as the kinetic energy gained by an electron that is accelerated through a potential difference of 1 volt. The SI unit of energy is joule (J), hence one eV is equivalent to 1.60219×10^{-19} J. The energy of a gamma-ray and x-ray photon is directly proportional to the frequency of the radiation and is related by the following:

$$E = h\nu \quad (\text{B.4})$$

where:

h is Plank's constant (6.626×10^{-34} J secs or 4.135×10^{-15} eV secs), and

ν is the frequency of the radiation.

As the emitted particles resulting from the radioactive decay pass through matter, some (or all) of this energy is absorbed by the material. The density of the material and the

type of particle are the main factors that determine the efficiency of the energy absorption. Concepts relating to characterizing the amount of ionizing energy absorbed by a biological system will now be discussed.

B.1.1 Radiation Dose and Exposure

Radiation dose and exposure are important concepts used in radiation detector physics to insure the safe use of radioactive isotopes. Health physics is the field of study interested in the understanding of the biological effects of ionizing radiation and the implementation of safe practices with its use. Various units and quantities have been devised in an attempt to provide consistent methods of characterizing the biological effects of various forms of ionizing radiation. The following is a description of the number of health physics concepts that are pertinent to this project.

For gamma-ray and x-ray exposure, the exposure value (X) is defined in terms of the following equation:

$$X = dQ/dm. \quad (\text{B.5})$$

The charge, dQ , results from the ionization of air molecules by secondary electrons produced by the absorption of gamma-ray or x-ray photons in a volume of air with mass dm . The SI units for this definition of exposure is coulombs per kilogram (C/kg). Historically, this unit has been called the roentgen (R) and is defined as that amount of x-ray and gamma-ray radiation, which in one cubic centimeter (cm^3) of air at standard temperature and pressure (STP), will produce one electrostatic unit (e.s.u) of charge. Therefore, one roentgen (R) is equal to 2.58×10^{-4} C/kg.

The exposure rate is a function of the activity (a) of a radioactive source and the square of the distance (d) from the source:

$$\text{exposure rate} = \Gamma a/d^2. \quad (\text{B.6})$$

In the above equation Γ is the exposure rate constant and has the units of R-cm²/hr-mCi.

This unit tells nothing about the quantity of energy absorbed or the possible biological damage caused by the ionizing radiation. To better quantify the biological affect of a particular form of ionizing radiation (x-rays, gamma-rays, fast electrons etc.) one needs to quantify the absorbed dose. The absorbed dose is the energy absorbed by any type of radiation (charged or uncharged) per unit mass of the absorbing material. The amount of energy absorbed is dependent upon the elemental composition of the absorbing material, and on the energy and type of radiation. The rad is the unit historically used for absorbed dose and is defined as 100 ergs of energy absorbed per gram of material.

One roentgen (R) of gamma-rays delivers a dose in soft tissue of approximately 93 erg/g. The SI equivalent unit for rad is the gray (Gy) and is defined as 1 joule/kilogram, therefore:

$$1 \text{ Gy} = 100 \text{ rad.}$$

The absorbed dose in air corresponding to a gamma-ray exposure of 1 C/kg (or 3.876×10^3 R) is 33.8 joules/kilogram (33.8 Gy).

To evaluate the biological impact of ionizing radiation the concept of dose equivalence (rem) has been introduced. The amount of biological damage by a particular form of ionizing radiation is directly proportional to the amount of energy deposition on the track formed by the passage of the radiation through a biological system. This local amount of deposited energy is defined as the linear energy transfer (LET). A larger level of biological damage results from ionizing radiation with a large LET such is the case with a heavy ion. Electrons have a lower LET value so less damage can result from the electron even though the total energy per unit mass deposited may be equivalent to that of the heavy ion. A unit of dose equivalent is defined as that amount of any type of radiation that, when

absorbed in a living organism, results in the same biological effect as one unit of absorbed dose obtained in the form of radiation with a low LET value.

The dose equivalent (H) is defined by the following:

$$H = DQ \quad (B.7)$$

where:

D is the absorbed dose in rads, and

Q is the quality factor.

The quality factor Q increases with linear energy transfer (L). The Q value is ~1 for electrons, gamma-rays, and x-rays but is ~20 for alpha particles. If D is expressed in unit of rads, then H is defined in the units of rem. The latest SI convention expresses D in units of Grays and the unit of dose equivalent is referred to as a Sievert (Sv) where one Sievert is equal to 100 rem. The following is an example of how one might use the above concepts to describe in general terms the dose received to a person who is working 1 meter from a 10 μCi ^{125}I point source:

An amount of 10 μCi of ^{125}I could be the typical quantity handled for an animal experiment in this project. The exposure rate from a 10 μCi ^{125}I is obtained from the following:

$$\text{exposure rate} = \Gamma a/d^2. \quad (B.7)$$

The exposure rate constant (Γ) for ^{125}I is 0.7 R-cm²/hr-mCi. Therefore, the exposure rate is equal to 7 x 10⁻⁸R/hr. To convert this to an absorbed dose rate, the energy per unit mass of tissue needs to be known for gamma-rays. For a 1R dose of gamma-ray radiation, soft tissue absorbs approximately 93 erg/g. Using this quantity, one obtains an energy deposition rate of 6.51 x 10⁻⁶ erg/g-hr. Since 1 erg/g is equivalent to 10⁻⁴ Gy, the

resulting absorbed dose rate expressed in SI units, is 6.51×10^{-10} Gy/hr, or in the older unit of rad ($1 \text{ rad} = 10^{-2} \text{ Gy}$), the resulting dose rate is 6.51×10^{-8} rad/hr. To obtain the dose equivalent rate (H) one needs to know the form of the radiation. The Q value is one for gamma-rays and x-rays. Therefore, for ^{125}I , Q is equal to 1, so for this case Gy/hr is equivalent to Sv/hr which leads to a dose equivalent rate of 6.51×10^{-10} Sv/hr. This can also be expressed in the older units of rems, since 1 Sv is equal to 100 rem, the dose equivalent rate is 6.51×10^{-8} rem/hr.

The average dose per person for all possible sources (natural, environmental and medical) is about 3-4 mSv/yr. So one can see that for this project the exposure risk from a typical animal study is minimal.

B.2 Decay Processes

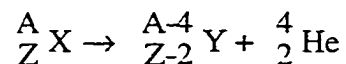
As mentioned, nuclear transitions associated with radioactivity result in a new isotope and the emission of charged and uncharged particulate radiation. A nuclide is characterized by the number of protons and neutrons in its nucleus. One quantity, the atomic mass number (A), is defined as the total number of protons in the atom's nucleus. The other, atomic number (Z), is the sum of the number of protons plus the number of neutrons in the atom's nucleus. The charged particles emitted are electrons (beta particles) and heavy charged ions, while the uncharged emitted radiation is either x-ray photons, gamma-ray photons or neutrons.

Charged ions result from unstable nuclei that either undergo alpha decay in which an alpha particle (a helium nucleus) is emitted or they undergo spontaneous nuclear fission, resulting in the expulsion of charged ions. Fission is a less common decay mode which results in the emission of charged ions and can also result in the emission of neutrons. The various forms of nuclear decay will now be discussed. Described will be three forms of

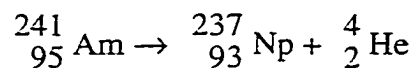
nuclear decay which result in the emission of three classes of particles: alpha particles, electrons, and high energy photons.

B.2.1 Emission of Alpha Particles

In alpha decay, the atomic nucleus emits a particle called an alpha particle which is composed of two protons and two neutrons. After alpha decay, the resulting daughter nuclide has a mass number (A) 4 less than the parent and an atomic number (Z) 2 less than the parent. Sometimes gamma rays are also emitted because of subsequent nuclear transitions by the decay of an unstable daughter nuclide. This type of decay can be written with the following equation:



Americium-241 which is a common calibration source for various radiation detectors decays via alpha decay to Neptunium-237 which itself is unstable and decays via alpha decay. However ${}^{237}\text{Np}$ has a half-life of 2.1×10^6 years compared to 432.7 days for ${}^{241}\text{Am}$. The isotope ${}^{241}\text{Am}$ emits alpha particles of energies 5.486 MeV (85% of the time) and 5.443 MeV (13%) and various other alpha particles. The decay of ${}^{241}\text{Am}$ is shown below.

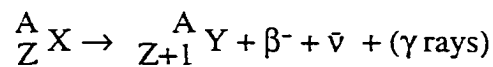


B.2.2 Ejection of Energetic Electrons

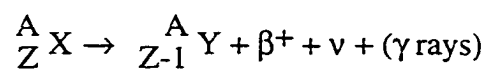
There are three sources of energetic electrons through radioactive decay: beta decay, internal conversion, and Auger electrons. The most common is beta decay.

Beta Decay

Beta decay is the decay mode in which an electron, (a β particle) or a positron is emitted. A positron is a beta particle with a positive charge. The positron ($+\beta$) is also referred to as the anti-particle to an electron. The energy of the emitted electrons resulting from beta decay is characterized by a continuous spectrum up to a maximum energy point called endpoint energy. This endpoint energy varies for different beta emitting isotopes, the endpoint energy for phosphorus 32 (^{32}P) is 0.248 keV and is 167 keV for sulfur 35 (^{35}S). Shown below is the beta decay resulting in the emission of an electron, an anti-neutrino ($\bar{\nu}$) and possible gamma-rays :



The anti-neutrino is the anti-particle of a neutrino. The neutrino is a very light particle which interacts very weakly with matter; its mass has just recently been measured to be non-zero [118]. Beta radiation is emitted with a continuous energy distribution up to the maximum endpoint energy. Because of this, energy-mass conservation laws require that another particle participate in the decay having the role of carrying off the kinetic energy equal to the difference between the maximum endpoint energy and the energy of the emitted beta particle. This particle is a neutrino. In beta decay, it is actually a neutron that decays to a proton, an electron and a anti-neutrino, hence an increase in atomic number but the mass number stays the same. Another example of beta decay is shown below:



In this case a proton decays ($Z-1$) resulting in three particles: a neutron, a positron and a neutrino. Isotopes that decay via beta decay and emit only beta particles with no emission of gamma-rays from daughter products which might be left in an excited nuclear state are known as “pure” beta emitters. In molecular biology, ^{32}P and sulfur ^{35}S are used in various assays to label molecules for detection with autoradiographic film. These isotopes decay via beta decay and are examples of “pure” beta decay; they decay directly from a nuclear excited state to the product ground state with the ejection of a fast electron. Other emitters may also emit gamma-rays because their nuclear transitions do not go directly to the ground state or their daughter products also emit gamma-rays.

When a nucleus undergoes a beta-plus (β^+) decay, a positron is emitted. The positron interacts with a nearby electron and therefore annihilates. This annihilation results in the disappearance of the electron and positron with the formation of two gamma-ray photons. These two gamma-rays always travel in opposite directions in order to conserve momentum. The energy of these two opposite directed gamma-rays is 511 keV.

Conversion Electrons and Auger Electrons

In addition to beta decay, electrons will be emitted from isotopes that generate internal conversion electrons and from those that generate Auger electrons. Internal conversion is a nuclear process that starts with an excited nuclear state which de-excites without the emission of a gamma-ray. The released energy, instead of being carried off by an emitted gamma-ray, is transferred to an orbital electron, that is then ejected. The internal conversion electron has an energy equal to the energy of the nuclear excited state minus the electron binding energy. Thus, the energy spectrum would show distinct energy peaks depending upon which orbital electron underwent internal conversion. The energy of the conversion electrons can be in the keV to MeV range.

If the atomic orbital shells, rather than the nucleus, is in an excited state, this state may also de-excite through the ejection of electrons, called Auger electrons. For example, this can occur when a normally-filled electron shell has become vacant because of an earlier event such as an electron capture. Electron capture is the term for the process in which a shell electron is captured by the atomic nucleus thus resulting in a shell vacancy. In electron capture, an inner-shell electron combines with a proton of the nucleus which then decays into a neutron and a neutrino. This shell vacancy is filled by the cascading down of outer shell electrons which then fill the vacancy. The excess energy of the filling electrons result in the emission of photons called characteristic x-rays. However, instead of emitting a characteristic x-ray, the atom can de-excite by ejecting an electron from the outer shell. These Auger electrons have lower energy than electrons from beta decay or internal conversion. The energy of these electrons is about a few keV.

B.2.3 Ejection of High Energy Photons

For the uncharged radiation, electromagnetic radiation is in the form of x-rays or gamma-rays. Both x-rays and gamma-rays are both high energy photons. The term x-ray is used to describe high energy photons originating from an electron shell transition and having energies from a few hundred eV to several hundred keV. Gamma-rays originate from nuclear transitions of an atom and can have energies as low as a few keV up to several MeV. Emission of characteristic x-rays, resulting from electron shell transitions in an atom, mentioned above, is an alternative process to Auger electrons. Characteristic x-rays can come about by the excitation of the atom through radioactive decays such as is the case for electron capture or it can come about because of excitation from external radiation such as electrons or x-rays which ionize the atoms.

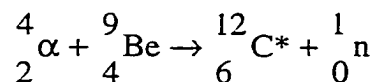
X-rays can also be emitted when fast electrons interact with matter whereby part of their energy is converted into a form of electromagnetic radiation known as bremsstrahlung

(braking) radiation. Bremsstrahlung radiation is the process through which x-rays are generated in x-ray tubes used for medical radiographs (also known as medical x-rays). In bremsstrahlung, a high speed charged particle, such as an electron, scatters in the Coulomb field of an atomic nuclei. As the particle decelerates some of its energy is released in a continuous fashion in the form of x-ray photons. The number of x-ray photons with energies between $h\nu$ and $h(\nu + d\nu)$ produced by an electron with energy E scattering in the Coulomb field of an atomic nucleus with a charge Ze is proportional to $\frac{Z^2}{\nu}$. This is expressed in mathematical form by the following:

$$N(\nu) d\nu \propto Z^2 \frac{d\nu}{\nu} \quad (\text{B.8})$$

where ν is the frequency of the x-ray photon.

Gamma-rays can result from beta decay and through the annihilation of the positron with an electron as mentioned earlier. Gamma-rays can also come about through nuclear reactions such as those used to produce neutrons for nuclear physics research. For instance, the following nuclear reaction results in the product nucleus ^{12}C left in an excited state which then decays giving rise to a 4.44 MeV gamma-ray:



The radioisotope iodine-125 (^{125}I) is an example of a radioisotope which emits an x-ray, a gamma-ray and Auger electrons. ^{125}I is commonly used in molecular biology and medical research and is readily available linked to nucleic acids and antibodies from companies providing probes for gene research. ^{125}I has a half-life of 60.2 days and decays

via electron capture with the emission of a 35 keV gamma-ray with the prompt emission of several 27-32 keV $K\alpha$ and $K\beta$ shell x-rays from the daughter product ^{125}Te [119].

B.3 Radiation Detection

In biomedical research the predominant radiations used are electrons, x-rays, and gamma-rays. The detection of these particles is accomplished either with photographic emulsions, scintillators, or gaseous based detectors. These particles are detected when they give up a portion or all of their energy in the detector material. Next is a discussion of the manner in which electrons and high energy photons (x-rays and gamma-rays) interact with matter. Following that is a description regarding materials called scintillators that are used to detect high energy particles.

B.3.1 Beta Particles

Electrons (beta particles) lose energy in matter through Coulomb interactions and radiative processes. Electrons are elementary particles (they apparently cannot be subdivided) and along with protons and neutrons are the constituents of all matter. Electrons carry a negative electric charge of -1.6026×10^{-19} Coulomb, are responsible for atomic and molecular processes, and are involved in semiconductor and conductor processes. Coulomb interactions involve the fast electron (the beta particle) giving up some of its energy when it has its direction of travel changed by a collision with a shell electron. This collision causes the shell electron to be knocked out of the atom (ionization) or to be raised to a higher energy orbital (excitation). Ionization is more likely to occur for high beta particle energies (fast electrons) and excitation is more likely for lower energy beta particles.

Radiative processes in which beta particles interact with matter can be detected in three cases: bremsstrahlung, Cerenkov radiation, and positron annihilation. In bremsstrahlung, x-ray photons are emitted in a continuous fashion as the beta particle has its direction of travel changed by passing near a shell electron or the nucleus of the atom. Cerenkov radiation, composed of optical photons (blue to UV) in a cone pattern, occurs when the speed of the electron in an optically transparent material, with an index of refraction greater than 1, is faster than the speed of light in that material. If the beta particle is a positron, it can be detected through the detection of the two annihilation 511 keV gamma rays that result from an electron-positron interaction.

B.3.2 Gamma-Rays and X-Rays

Gamma-rays and x-rays have a much higher matter penetrating capability than electrons. X-rays and gamma-rays, though uncharged, can cause the production of ion pairs (ionization) through secondary processes in which they interact with an atom, a shell electron or an atomic nucleus. The term gamma-ray (γ) will be used to include x-rays when describing the interaction processes for both gamma-rays and x-rays.

The absorption of gamma-rays by matter is dependent on the atomic number (Z) and density of the material and the energy of the gamma-ray. This can be described by the following equation:

$$I = I_0 e^{-\mu \rho x} \quad (\text{B.9})$$

where:

I_0 is the starting intensity of gamma-rays,

μ is the mass absorption coefficient (cm^2/g),

ρ is the density of the material (g/cm^3), and

x is the thickness (cm).

The interaction of gamma-rays with matter is described by three processes: photoelectric absorption, Compton scattering, and pair production. The mass absorption coefficient of the above equation is made of three parts as described by the following:

$$\mu = \mu_{pe} + \mu_C + \mu_{pp} \quad (\text{B.10})$$

where:

μ_{pe} is the photoelectric absorption coefficient,

μ_C is the Compton scattering absorption coefficient, and

μ_{pp} is the pair production absorption coefficient.

Photoelectric Absorption

For the case of photoelectric absorption a gamma-ray has all of its energy transferred to a shell electron which is then ejected thereby ionizing the atom. The gamma-ray, completely stopped by the matter, disappears, ejecting a shell electron whose kinetic energy is equal to the energy of the gamma-ray minus the electron binding energy (E_b). The atom rearranges its shell electrons often emitting x-rays. The photoelectric absorption coefficient of a material is proportional to the number of atoms in that material. Below is a diagram illustrating this type of interaction.

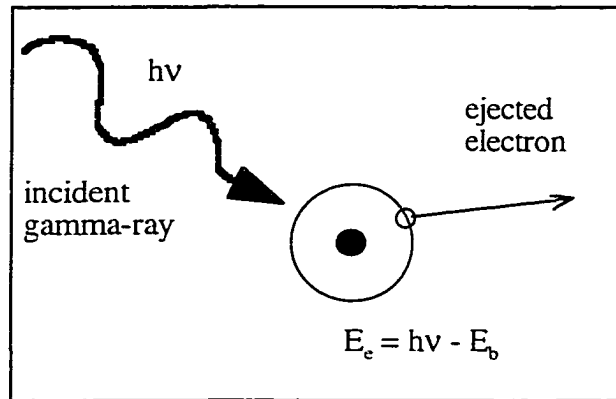


Figure B.1 Illustration of photoelectric absorption of an incident gamma-ray in a material in which a shell electron completely absorbs the gamma-ray energy.

Compton Scattering

In Compton scattering the gamma-ray transfers part of its energy to a weakly bound electron in the material. In effect, the gamma-ray bounces off an electron resulting in the gamma-ray and the recoil electron scattering in different directions. After this interaction, the gamma-ray has less energy and the recoil electron carries off the energy lost by the gamma-ray. The recoil electron subsequently gives up its kinetic energy by interacting with other electrons eventually being captured by an atom. The Compton scattering coefficient of a material is proportional to the number of electrons in that material. The following is an equation describing the energy of the scattered gamma-ray ($h\nu'$) in terms of the original energy ($h\nu$) and the scattering angle (Θ).

$$h\nu' = \frac{h\nu}{1 + (h\nu/m_0c^2)(1 - \cos\Theta)} \quad (\text{B.11})$$

where m_0c^2 is the rest mass energy of the electron (511 keV).

The kinetic energy of the recoil electron is give by:

$$E_e = hv - hv' = hv \left(\frac{(hv/m_0c^2)(1 - \cos\Theta)}{1 + (hv/m_0c^2)(1 - \cos\Theta)} \right) \quad (B.12)$$

Figure B.2 is a diagram of a Compton scattering interaction. In normal detector applications all scattering angles will occur such that a continuum of gamma-ray energies is transferred to the electrons resulting in a detected continuum energy spectrum.

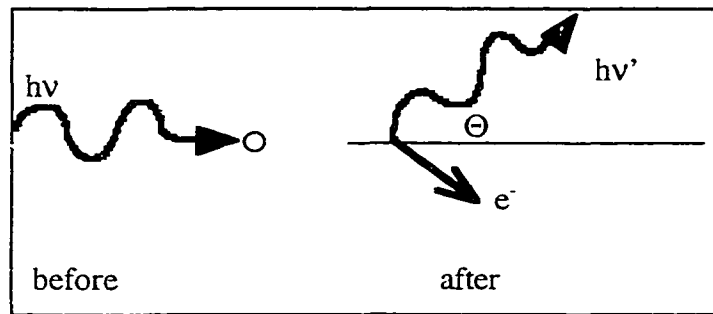


Figure B.2: Illustration of the Compton scattering interaction of a gamma-ray photon scattering off of an electron.

For very small angles ($\Theta \cong 0$) hv' is nearly equal to hv and the kinetic energy of the recoil electron is near zero. For the case where $\Theta = \pi$, the incident gamma-ray is completely back-scattered and the recoil electron is scattered in the original direction of the incident gamma-ray. The energy of the scattered gamma-ray and recoil electron is given by the equations below.

scattered gamma-ray: $hv' |_{\Theta=\pi} = \frac{hv}{1 + 2hv/m_0c^2} \quad (B.13)$

recoil electron: $E_e |_{\Theta=\pi} = hv \left(\frac{2hv/m_0c^2}{1 + 2hv/m_0c^2} \right) \quad (B.14)$

Pair production

Pair production occurs only if the gamma-ray has an energy greater than 1.022 MeV and if it is near the nucleus of an atom. When these conditions are met, the energy of the gamma-ray is converted into the production of an electron-positron pair. If the gamma-ray had an energy very close to 1.022 MeV then the positron appears at the detector with more kinetic energy than the electron because it experiences a repulsive force from the nuclear charge of a nearby nucleus. At higher gamma-ray energies this difference in kinetic energy of motion between the electron and positron disappears. The positron quickly interacts with a nearby electron and the two annihilate resulting in the production of two 511 keV gamma rays.

All three of these processes occur in gamma-ray detectors. For the project described in this thesis, the goal is the detection of the gamma-rays and x-rays from the decay of ^{125}I , in this case the photoelectric absorption and Compton scattering are all that occur since the maximum energy of the gamma-ray and x-ray photons encountered is 35 keV. An idealized energy spectrum showing the combination of the Compton scattering and photoelectric absorption events by the detector material is illustrated in Figure B.3 below.

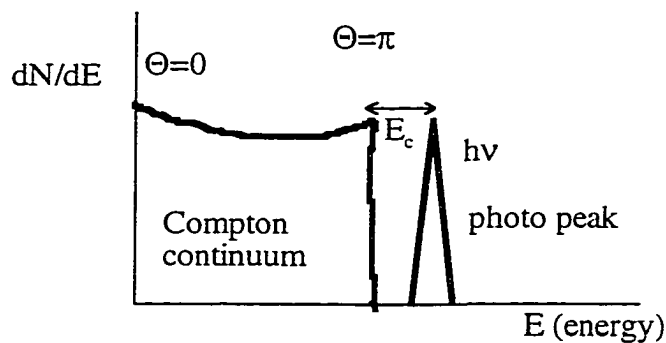


Figure B.3: General shape of a spectrum illustrating of combined photoelectric absorption events and Compton scattering of incident gamma-rays in an absorbing medium.

Medical imaging applications most often use materials known as scintillators. In this project, scintillators are used to detect and image the gamma-rays and x-rays emitted from ^{125}I .

B.3.3 Scintillators

A scintillator is a transparent material that generates pulses of light (scintillates) by converting the energy lost by ionizing radiation. In the case of medical imaging applications the ionizing radiation is x-rays, gamma-rays, and beta particles. As a high energy particle passes through the scintillator crystal some or all of the energy of the particle is deposited in the crystal material because of photoelectric absorption or Compton scattering. This eventually results in ionization and excitation phenomena which in turn lead to the emission of photons through luminescence, phosphorescence and delayed fluorescence. Ideally the conversion of the incident radiation to prompt fluorescence should dominate and conversion via phosphorescence and delayed fluorescence should be a minimum. Scintillation photons have wavelengths from ultraviolet to visible. This pulse of scintillation photons is detected by light sensitive measuring detectors such as photomultiplier tubes or photodiodes.

The most often used scintillators are either organic liquids and plastics, or inorganic alkali halide crystals, such as CsI(Na). The prompt fluorescence of some scintillators decays in times of ~0.5 nanoseconds to 5 nanoseconds. Inorganic scintillators may take as much as 5000 nanoseconds for light emissions to decay. The number of light photons emitted by a scintillator is often characterized as number of photons per MeV of absorbed energy. For a plastic scintillator the typical value is 1×10^4 photons/MeV of absorbed energy. An inorganic scintillator such as CsI(Na) has a light yield of 3.4×10^4 photons/MeV. There are other differences between organic and inorganic scintillators which will now be discussed.

Organic Scintillators

Organic scintillators are usually liquids or plastics, and as mentioned have very short decay times (a few nanoseconds) for the scintillation pulse. Organic scintillators are most often used for the detection of beta particles and neutrons. Fluorescence in organic scintillators occurs from transitions in the energy level structure of a single molecule and therefore occurs whether it is a solid, liquid or gas. The molecules that make up an organic scintillator have special energy level structures which are called π -electron structure. This π -electron structure is characterized by a series of singlet and triplet states. The states are further divided by a series of levels, called vibrational states. Prompt fluorescence (scintillation) results from the de-excitation between the lowest vibrational state of the singlet state and one of the vibrational states of the ground state. The triplet states can be populated from singlet states in a process called "inter-system crossing." Excited triplet states have longer decay times than singlets giving rise to delayed emission, called phosphorescence. An energy level diagram is shown in Figure B.4 to illustrate these concepts.

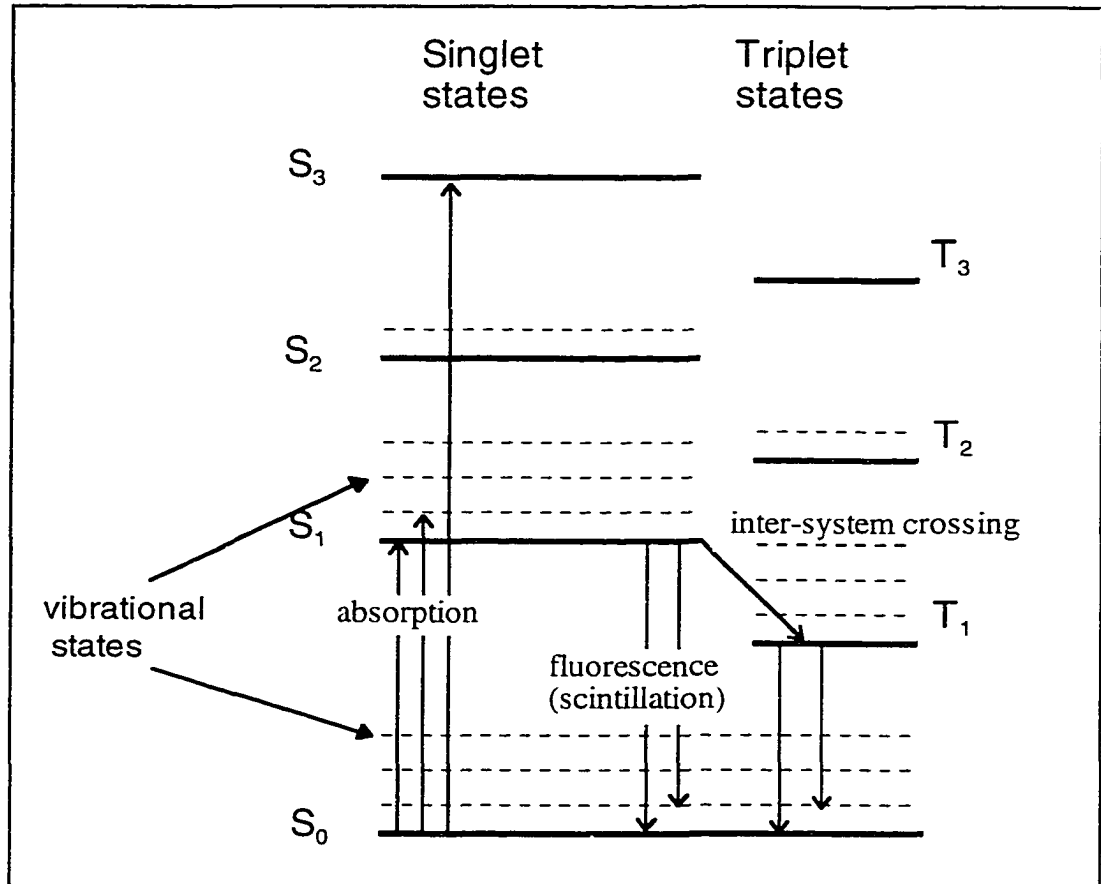


Figure B.4: Energy level diagram of the π -electron structure of an organic molecule. For molecules of typical organic scintillators the energy spacing between the S_0 and S_1 state is ~ 4 eV and is less between higher states.

Organic scintillators are less expensive and can be made into large sizes. Their low Z material makes them good for beta particle detection because it reduces back-scattering. When a beta particle is back-scattered it does not cause scintillation. For the inorganic scintillator thallium doped sodium iodide Na(Tl) the percentage of beta particles that back-scatter is $\sim 30\%$. Plastic scintillators consist of plastic host material which is doped with an organic scintillating molecule. It is through the Compton effect that gamma-rays transfer their energy into scintillation light. Because of their low Z and low density, organic scintillators have poor efficiency for high energy gamma-rays but are used for high rate

applications where speed is more important than efficiency. In molecular biology, liquid organic scintillators are often used for accurate counting of beta emitters (^3H , ^{14}C or ^{32}P) and low energy gamma-ray emitters (^{125}I).

Inorganic Scintillators

Inorganic crystals such as sodium doped cesium iodide are often used for gamma-ray detection because they are constructed out of high Z material and are denser than organic scintillators. Though inorganic scintillators are slower than organic scintillators, they have higher light output which is important for maximum energy resolution in gamma-ray detection. The energy states defined by the crystal lattice of the crystal material govern the scintillation mechanism for inorganic materials. The valence band is the lower energy band and the conduction band is the upper. This is in contrast to organic scintillators in which the energy levels of individual molecules are involved. The outer electron orbitals (the valence electrons) of the crystal define discrete groups of energy levels which are referred to as bands in semiconductors and insulators (see Figure B.5).

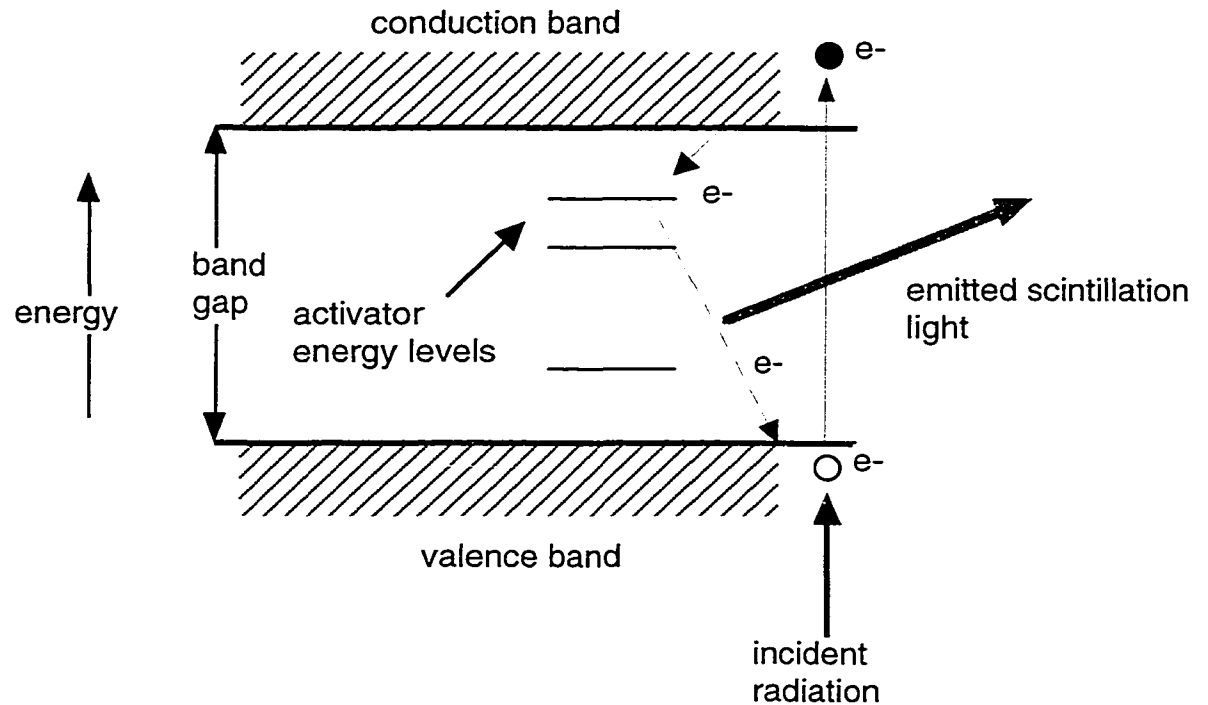


Figure B.5: Illustration of the energy bands in a scintillation crystal. The incoming radiation causes a valence electron to be raised to the conduction band. This electron drops down to activator energy levels which de-excite giving rise to emission scintillation photons.

The valence band contains electrons that are strongly bound at crystal lattice sites and these electrons do not move or conduct through the pure crystal. The conduction band represents electrons which are free to move through the crystal since they have enough energy. A pure insulator only has electrons in the valence band. Conductors have electrons populating the conduction band. In a pure crystal, no energy levels are located in the “forbidden” gap referred to as the band gap. Incident radiation on the crystal can provide sufficient energy to excite electrons to the conduction band. These electrons de-excite back down to the valence band and release their energy in the form of photons. Forbidden energy levels can exist in the gap between these energy levels in crystals that have impurities. Often impurities called activators or dopants are added to the crystal

during crystal growth to increase the efficiency of the scintillation process by forming energy levels in the band gap.

For many pure crystals, the band gap is so wide that the wavelength of the de-excitation photon may not be in the range of the light detection device. The impurities form activator energy levels that require less energy to be excited, and the wavelength of de-excitation photons are more often in the range of near ultraviolet or visible which is detectable by light measuring devices such as photomultiplier tubes. Sodium iodide, which is thallium activated (NaI[Tl]), because it contains high Z material and is dense (3.67 g/cc), is a common crystal scintillator used in particle physics and medical imaging for x-ray and gamma ray detection.

Many scintillation crystals are hygroscopic, that is, they readily absorb water vapor which eventually degrades the scintillator. Hygroscopic scintillation crystals are cut and polished in a pure nitrogen atmosphere, and then hermetically sealed. In Table B.1 is a summary of crystal scintillators that could be used in nuclear medicine.

SCINTILLATOR	NaI(Tl)	LSO	LuAP	GSO	YAP	CsI(Na)
Formula	NaI(Tl)	Lu ₂ (SiO ₄)O:Ce	LuAlO ₃ :Ce	Gd ₂ (SiO ₄)O:Ce	YAlO ₃ :Ce	CsI(Na)
Rel. Light Yield	100	75	>65	20-25	40	85
Peak Wavelength (nm)	410	420	365	440	365	420
Decay Constant (ns)	230	12,42	18	30-60	25	630
Density (g/cc)	3.67	7.40	8.34	6.71	5.37	4.51
Index of Refraction	1.85	1.82	1.94	1.85	1.95	1.84
Hygroscopic ?	yes	no	no	no	no	slight

Table B.1: Various properties of crystal scintillators considered for the present project.

The following section will now describe the operation of photomultiplier tubes. The most common scintillation detection device used in particle physics and medical imaging is the photomultiplier tube.

B.3.4 Photomultiplier Tubes

Photomultiplier tubes are very sensitive light detection devices that are capable of converting the faint light pulse from a scintillator to an electrical signal achieving a gain amplification factor as high as 1×10^8 . Photomultiplier tubes in addition to possessing high gain, have a fast response and can operate in radiation environments.

Light entering the window of the photomultiplier tube strikes a semiconductor photosensitive material called a photocathode. In a photomultiplier tube with a transmission photocathode, the photocathode material is deposited on the inside surface of the photomultiplier window of the evacuated glass envelope. Another type of photomultiplier tube, called a side window photomultiplier tube, has a reflection photocathode deposited on a structure inside the photomultiplier tube. In Figure B.6 is a diagram of the two types of photomultiplier tubes.

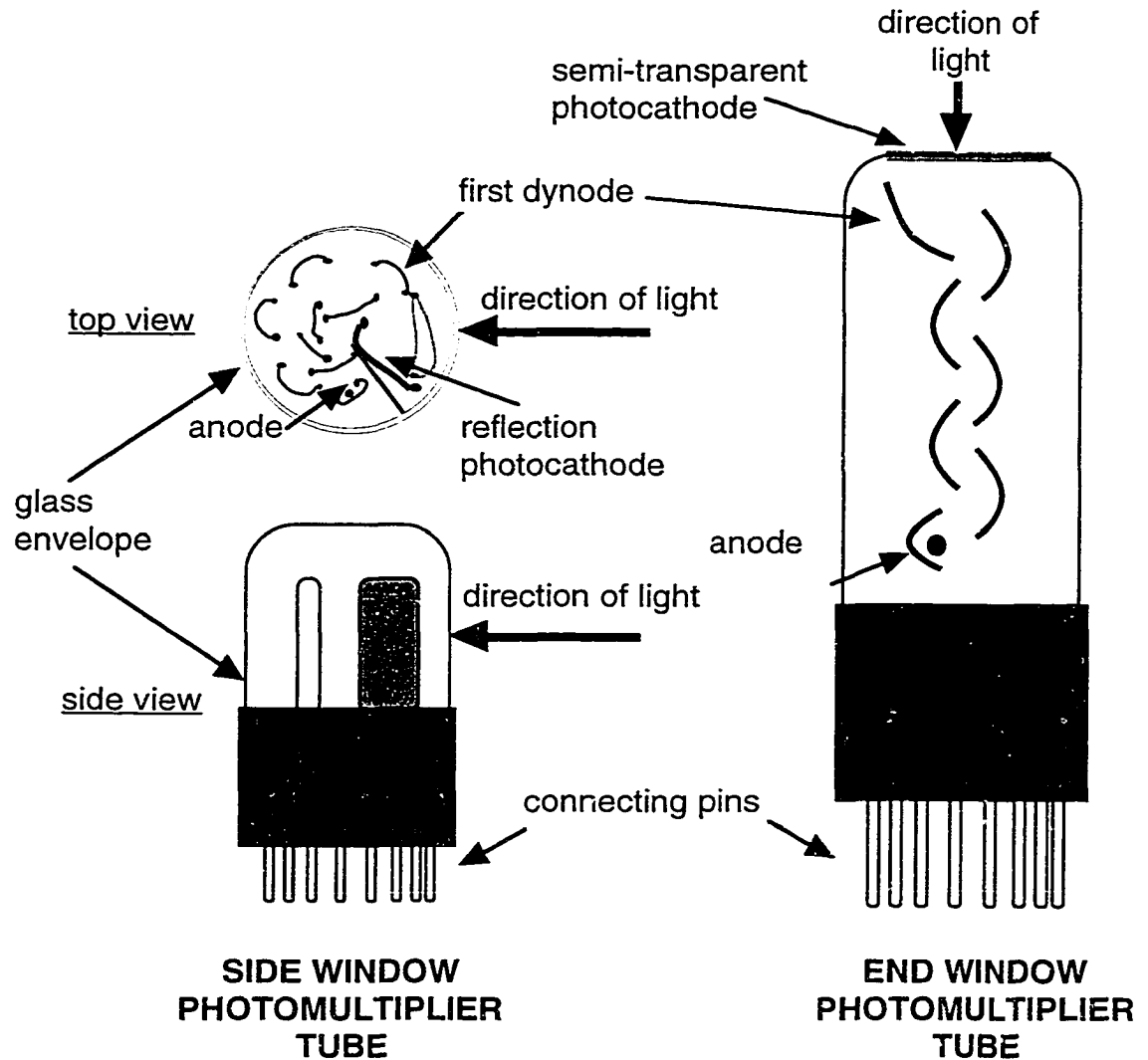


Figure B.6: Diagram illustrating the two types of photomultiplier tubes. When the light strikes the photocathode photoelectrons are released which are directed by an electric field to the first dynode. These photoelectrons strike the next dynode thus releasing additional secondary electrons. This multiplication process continues until the electrons are collected by the anode.

When a photon strikes the photocathode it causes electrons, called photoelectrons, to be released from the photocathode material through a process called the photoelectric effect. In the photoelectric effect, the absorption of the energy of the incident photon by an atom in the photocathode material results in an electron being ejected with a kinetic energy

which is a function of the energy of the incident photon. The energy (E) of the outgoing electron is defined by:

$$E = h\nu - E_b \quad (\text{B.14})$$

where E_b is the binding energy of the electron.

Most often the photocathode is made from a thin layer of Cs, Sb and K atoms that, for the end window photomultiplier tube, have been evaporated onto the inner surface of the entrance window of the photomultiplier tube. After the photon interaction, a photoelectron migrates to the photocathode surface and is thus able to escape. By the action of an externally produced electric field, the photoelectron is directed to a structure in the tube called the first dynode. On the surface of the dynode is a secondary electron emissive material that when struck by an electron is able to eject 3 to 4 additional electrons that are called secondary electrons. These electrons are then directed by the external electric field to additional dynodes that compose the remainder of the multiplication stage of the photomultiplier tube. The final output stage of photomultiplier tube is called the anode, and it is on the anode that the total charge is collected. The total electrical potential setup between the photocathode and anode is typically of the order of 1 kV to 2 kV.

The intensity of the photon pulse translates into a corresponding charge pulse at the anode, i.e. a large light pulse results in a large charge pulse at the anode. The intensity of the light pulse is characterized in terms of the number of photoelectrons produced at the photocathode. The faintest light pulse measurable generates a single photoelectron that results in a charge pulse equal to gain of the photomultiplier tube. The gain of the photomultiplier tube is defined by the dynode multiplication chain and is typically 1×10^8 . The quantum efficiency (QE) of the photomultiplier tube is determined by the photocathode. The quantum efficiency of a photocathode is usually between 20 and 30 % and is defined as:

$$QE = \frac{\text{\# of emitted photoelectrons}}{\text{\# of incident photons}} \quad (\text{B.15})$$

Typical photocathodes have a practical wavelength sensitivity going from near infrared up to the ultraviolet.

For the case of a standard photomultiplier tube, when a photon strikes the photocathode position information on where the photon was incident is not retained. Recently, position sensitive photomultiplier tubes have become available which use a parallel plate or grid type dynodes, and multiple anodes to obtain the position information of point of incidence. The position sensitive photomultiplier tube is the core of the imaging device of the detector system described in this thesis. The position sensitive photomultiplier tube used in this project uses fine mesh dynodes and crossed wire anode read out. The operation of the actual position sensitive photomultiplier tube is described in the main text of this thesis.

B.3.5 Final Detector Assembly

The choice of the major detector components, namely the scintillator and photomultiplier tube, depend upon the type and intensity of radiation to be detected. For the application of the project described in this dissertation, one required an imaging detector that could detect low intensity, low energy gamma-rays and x-rays resulting from the decay of ^{125}I . Since amounts of ^{125}I to be detected were relatively low, therefore the rate of incident gamma-rays and x-rays would also be low. Because of this a fast scintillator was not needed but rather one that would provide the most light given the low energy gamma-rays and x-rays to detect. The steps taken to arrive at the final detector system are described in the main text.

Bibliography

- [1] NEN[®]Research Products Catalog, DuPont NEN, June 1994.
- [2] J.R. Lever, "Radiotracer Production: Radioiodinated Compounds," in Principles of Nuclear Medicine, 2nd edition, eds: H.N. Wagner Jr, Z. Szabo, and J.W. Buchanan, W.B. Saunders Company, pp. 199-213, 1995.
- [3] K.J. Jeffries, S. Kim, and H.N. Wagner, "*In Vivo* Probes: Pharmacological Studies," in Principles of Nuclear Medicine, 2nd edition, eds: H.N. Wagner Jr, Z. Szabo, and J.W. Buchanan, W.B. Saunders Company, pp. 275-285, 1995.
- [4] A. Gjedde, "Glucose Metabolism," in Principles of Nuclear Medicine, 2nd edition, eds: H.N. Wagner Jr, Z. Szabo, and J.W. Buchanan, W.B. Saunders Company, pp. 54-71, 1995.
- [5] R.J. Jaszczak, and B.M.W. Tsui, "Single Photon Emission Computed Tomography (SPECT): General Principles," in Principles of Nuclear Medicine, 2nd edition, eds: H.N. Wagner Jr, Z. Szabo, and J.W. Buchanan, W.B. Saunders Company, pp. 317-327, 1995.
- [6] M.M. Ter-Pogossian, "Positron Emission Tomography: General Principles," in Principles of Nuclear Medicine, 2nd edition, eds: H.N. Wagner Jr, Z. Szabo, and J.W. Buchanan, W.B. Saunders Company, pp. 342-345, 1995.
- [7] H.O. Anger, "Scintillation Camera", *Review of Scientific Instrumentation*, vol. 29, pp. 27-33, 1958.
- [8] J.M. Links and J.C. Engdahl, "Planar Imaging," in Principles of Nuclear Medicine, 2nd edition, eds: H.N. Wagner Jr, Z. Szabo, and J.W. Buchanan, W.B. Saunders Company, pp. 307-316, 1995.
- [9] Collimator Catalog, Nuclear Fields Corporation, Des Plaines, Illinois.
- [10] H.O. Anger, "Radioisotope Camera", Instrumentation in Nuclear Medicine, vol. 1, ed. G.J. Hine (New York: Academic), pp. 485-552, 1967.
- [11] K. Ishizu, T. Mukai, Y. Yonekura, M. Pagani, T. Fujita, Y. Magata, S. Nishizawa, N. Tamaki, H. Shibasaki, and J. Konishi, "Ultra-high Resolution SPECT System Using Four Pinhole Collimators for Small Animal Studies," *Journal of Nuclear Medicine*, vol. 36, no. 12, pp. 2282-2287, December 1995.

- [12] R.J. Jaszczak, J. Li, H. Wang, M.R. Zalutsky, and R. E. Coleman, "Pinhole collimation for ultra-high-resolution, small-field-of-view SPECT," *Phys. Med. Biol.*, vol 39, pp. 425-437, 1994.
- [13] S.C. Moore, K. Kouris and I. Cullum, "Collimator Design for Single Photon Emission Tomography," *European Journal of Nuclear Medicine*, vol. 19, pp. 138-150, 1992.
- [14] H.O. Anger, "Radioisotope Cameras," *Instruments in Nuclear Medicine*, ed. G.J. Hine, Academic Press, Inc., New York, vol 1, pp. 485-552, 1967.
- [15] E.L. Keller, "Optimum Dimensions of Parallel-hole, Multi-aperture Collimators for Gamma-Ray Cameras," *The Journal of Nuclear Medicine*, vol. 9, no. 6, pp. 233-235, 1968.
- [16] J.A. Sorenson and M.E. Phelps, *Physics in Nuclear Medicine*, 2nd ed., Philadelphia, W.B. Saunders, p. 326, 1987.
- [17] G.F. Knoll, *Radiation Detection and Measurement*, John Wiley and Sons, Inc., New York, 1989.
- [18] M.R. Stytz and O. Frieder, "Three dimensional Medical Imaging Modalities: An Overview," *Critical Reviews in Biomedical Engineering*, vol 18, no. 1, pp. 1-25, 1990.
- [19] W.H. Bakker, E.P. Krenning, W.A. Breeman, J.W. Koper, P.P. Kooij, J.C. Reubi, J.G. Klijn, T.J. Visser, R. Docter and S.W. Lambert, "Receptor Scintigraphy with a radioiodinated Somatostatin Analogue: Radiolabeling, Purification, Biologic Activity, and In Vivo Application in Animals," *The Journal of Nuclear Medicine*, vol. 31, no. 9, pp. 1501-1509, September 1990.
- [20] R. Hichwa, "Are Animal Scanners Really Necessary for PET," *The Journal of Nuclear Medicine*, vol. 33, no. 4, pp. 1396-1397, August 1994.
- [21] R. Myers, T. Jones, S. Hume, P. Boomfield, S. Rajeswaran, A. Lammertsma, E. Hirani, R. Nutt, B. Jones, J. Young, M. Andreaco, C. Williams, L. Byars, "RATPET: Applications in small animals," *Society of Nuclear Medicine Meeting, Categorical Seminar: Animal Imaging in Nuclear Medicine*, Toronto, Canada, June 7, 1998.
- [22] W. Potter, "Potential for Small Animal Imaging in Drug Development and Discovery," *High Resolution PET & Single Photon Imaging in Small Animals: A Symposium on Recent Advances, Methods and Applications*, Albuquerque, NM, Nov. 16, 1997.
- [23] B. Langstrom and R.F. Dannals, "Radiotracer Production: Carbon-11 Compounds," in *Principles of Nuclear Medicine*, 2nd edition, eds: H.N. Wagner Jr, Z. Szabo, and J.W. Buchanan, W.B. Saunders Company, pp. 166-178, 1995.
- [24] G. Stocklin, "Radiotracer Production: Fluorine-18 Compounds," in *Principles of Nuclear Medicine*, 2nd edition, eds: H.N. Wagner Jr, Z. Szabo, and J.W. Buchanan, W.B. Saunders Company, pp. 178-194, 1995.

- [25] S.Z. Lever, "Radiotracer Production: Technetium and Rhenium Compounds," in Principles of Nuclear Medicine, 2nd edition, eds: H.N. Wagner Jr, Z. Szabo, and J.W. Buchanan, W.B. Saunders Company, pp. 213-220, 1995.
- [26] U.K. Bruner, O. Renn, M. Li, C.F. Meares, "Radiotracer Production: Radiometals and Their Chelates," in Principles of Nuclear Medicine, 2nd edition, eds: H.N. Wagner Jr, Z. Szabo, and J.W. Buchanan, W.B. Saunders Company, pp. 220-229, 1995.
- [27] F.F. Knapp Jr, C. Brihaye, and A.P. Callahan "Radionuclide Production: Generators," in Principles of Nuclear Medicine, 2nd edition, eds: H.N. Wagner Jr, Z. Szabo, and J.W. Buchanan, W.B. Saunders Company, pp. 220-229, 1995.
- [28] K. Ishizu, T. Mukai, Y. Yonekura, M. Pagani, T. Fujita, Y. Magata, S. Nishizawa, N. Tamaki, H. Shibasaki and J. Konishi, "Ultra-high Resolution SPECT System Using Four Pinhole Collimators for Small Animal Studies," *The Journal of Nuclear Medicine*, vol. 36, no. 12, pp. 2282-2287, December 1995.
- [29] D.A. Weber, M. Ivanovic, D. Franceschi, S.E. Strand, K. Erlandsson, M. Franceschi, H.L Atkins, J.A. Coderre, H. Susskind, T. Button, et al., "Pinhole SPECT: An Approach to In Vivo High Resolution SPECT Imaging in Small Laboratory Animals," *The Journal of Nuclear Medicine*, vol. 35, no. 2, pp. 342-248, February 1994.
- [30] R.J. Jaszczak, J. Li, H. Wang, M.R. Zalutsky and R. E. Coleman, "Pinhole collimation for ultra-high-resolution, small-field-of-view SPECT," *Physics in Medicine and Biology*, vol. 39, pp. 425-437, 1994.
- [31] D.A. Weber and M. Ivanovic, "Pinhole SPECT:Ultra-High Resolution Imaging for Small Animal Studies,"[editorial] *The Journal of Nuclear Medicine*, vol. 36, no. 12, pp. 2287-2289, December 1995.
- [32] F.A. Dilmanian, D.A. Weber, J.A. Coderre, D.D. Joel, K.-C. Shi, G.E. Meinken, P. Som, Y.-N. Tang, N.D. Volkow, C. Yee, A.B. Brill, M. Watanabe, M.;E. Inuzuka, K.Oba, R. Gerson, H. Iida, A. Hiruma, "A High-Resolution SPECT System Based on a Microchannel-Plate Imager," *IEEE Transactions on Nuclear Science*, vol.37, no.2, pt. 1, p. 687-695, 1990.
- [33] Hamamatsu Corporation, Bridgewater, N.J.
- [34] P.P. Antich, J. Anderson, A.Constaninescu, J. Prior, J. Fernando and R.W. Parkey, "High Resolution I-125 Imaging of Rat Brain Blood Flow with Plastic Scintillation Detectors and Position sensitive Photomultipliers," *The Journal of Nuclear Medicine*, 33:5, p. 1003, 1992.
- [35] P.V. Kulkarni, J. Anderson, P.P. Antich, J.O. Prior, Y. Zhang, J. Fernando, A. Constantinescu, N.C. Goomer, R.W. Parkey E. Fenyves, R.C. Chaney, S.C. Srivastava and L.F. Mausner, "New approaches in medical imaging using plastic scintillating detector," *Nuclear Instruments and Methods in Physics Research B*, vol. B79, pp. 921-925, 1993.

- [36] P.V. Kulkarni, P.P. Antich, A. Constaninescu, J. Anderson, J. Fernando, J. Prior, T. Nguyen, R.W. Parkey, S.D. Weitman, B.A. Kamen R.C. Chaney and E.J. Fenyvesy, "Imaging of Folate Receptors with I-125 Labeled Folate Using Small Animal Imaging System Built with Plastic Scintillating Optical Fibers," *International Society for Optical Engineering (SPIE)* vol. 2281 pp 76-81, 1994.
- [37] F. de Notaristefani, R. Pani, F. Scopinaro, L.M. Barone, K. Blazek, G. De Vincentis, T. Malatesta, P. Maly, R. Pellegrini, A. Pergola, A. Soluri and F. Vittori, "First Results from a YAP:Ce Gamma Camera for Small Animal Studies," *IEEE Transactions on Nuclear Science*, vol.43, no.6, p. 3264-3271, 1996.
- [38] R.Pani, F.Scopinaro, G.Depola, R.Pellegrini, A.Soluri; "Very High Resolution Gamma Camera Based on Position sensitive Photomultiplier Tube," *Physica Medica*, vol 9, no. 2-3, pp. 233-236, 1993.
- [39] L.H.Barone, K.Blazek, D. Bollini, A. Del Guerra, F. de Notaristefani, G. De Vincenis, G. Di Domenico, M. Galli, M. Giganti, P. Maly, R. Pani, R. Pellegrini, A. Pergola, A. Piffanilli, F. Scopinaro, A. Soluri, F. Vittori, "Toward a nuclear medicine with sub-millimeter spatial resolution," *Nuclear Instruments and Methods in Physics Research A* , vol. 360, pp. 302-306, 1995.
- [40] A. Valda Ochoa, L. Ploux, R. Mastrippolito, Y. Charon, P. Laniece, L. Pinot, L. Valentin, "An Original Emission Tomograph for In Vivo Brain Imaging of Small Animals," *IEEE Transactions on Nuclear Science*, vol.44, no.4, pp. 1533-1537, 1997.
- [41] M.V. Green and J. Seidel, "MousePET and the Limitations of Imaging," Society of Nuclear Medicine Meeting, *Categorical Seminar: Animal Imaging in Nuclear Medicine*, Toronto, Canada, June 7, 1998.
- [42] A. Srinivasan, S.S. Gambhir, A.L. Green, S.R. Cherry, S. Sharfstein, J.. Barrio, N. Satyamurthy, M. Namavari, L. Wu, A.J. Beck, M.E. Phelps, and H. Hershman, "A PET Reporter Gene (PRG) / PET Reporter Prober (PRP) Technology for Repeatedly Imaging Gene Expression in Living Animals," *The Journal of Nuclear Medicine*, vol. 37, no. 5, p. 107P, May, 1996.
- [43] H. Herschman, "Animal Models of Disease, Gene Therapy, and Potential for Using PET," High Resolution PET & Single Photon Imaging in Small Animals: A Symposium on Recent Advances, Methods and Applications, Albuquerque, NM, Nov. 16, 1997.
- [44] P.D. Cutler, S.R. Cherry, E.J. Hoffman, W.M. Digby, M.E. Phelps, "Design features and performance of a PET system for animal research," *Journal of Nuclear Medicine*, vol. 33, no. 4, pp. 595-604, April 1992.
- [45] S. Siegel, S.R. Cherry, A.R. Ricci, Y. Shao, M.E. Phelps, "Development of continuous detectors for a high resolution animal PET system," *IEEE Transactions on Nuclear Science*, vol.42, no.4, pt.1, p. 1069-1074, 1995.
- [46] Y. Shao; S.R. Cherry, S. Siegel and R.W. Silverman, "A study of inter-crystal scatter in small scintillator arrays designed for high resolution PET imaging," *1995 IEEE*

Nuclear Science Symposium and Medical Imaging Conference Record, vol. 2 , pp. 1006-1010, 1995.

[47] S.R. Cherry, Y. Shao, S. Siegel, R.W. Silverman, E. Mumcuoglu, K. Meadors, M.E. Phelps, "Optical fiber readout of scintillator arrays using a multi-channel PMT: a high resolution PET detector for animal imaging," *1995 IEEE Nuclear Science Symposium and Medical Imaging Conference Record*, vol.3, pp. 1766-1770, 1995.

[48] S.R. Cherry, Y. Shao, R.W. Silverman, K. Meadors, S. Siegel, A. Chatziioannou, J.W. Young, W. Jones, J.C. Moyers, D. Newport, A. Boutefnouchet, T.H. Farquhar, M. Andreaco, M.J. Paulus, D.M. Binkley, R. Nutt, M.E. Phelps, "MicroPET: a high resolution PET scanner for imaging small animals," *IEEE Transactions on Nuclear Science*, vol.44, no.3, pt.2, p. 1161-1166, June 1997.

[49] Philips Photonics / Photonis, Cedex, France.

[50] J.R. Barrio, S-C. Huang, D-C Yu, W.P. Melega, J. Quintana, S.R. Cherry, A. Jacobson, M. Namavari, N. Satyamurthy and M. Phelps, "Radiofluorinated L-m-Tyrosines: New In-Vivo Probes for Central Dopamine Biochemistry," *Journal of Cerebral Blood Flow and Metabolism*, vol. 16, no. 4 pp. 667-678, 1996.

[51] Z.A. Martinez, M. Colgan, L.R. Baxter Jr, J. Quintana, S. Siegel, A. Chatziioannou, S.R. Cherry, J.C. Mazziotta and M.E. Phelps, "Oral 18F-fluoro-2-deoxyglucose for primate PET studies without behavioral restraint: demonstration of principle," *American Journal of Primatology (CM4)*, vol. 42, no. 3 pp. 215-224, 1997.

[52] J. Seidel, W.R. Gandler, M.V. Green, "A Very High Resolution Single Slice Small Animal PET Scanner Based on Direct Detection of Coincidence Line Endpoints," *Journal of Nuclear Medicine*, vol 35, pp. 40P, 1994.

[53] C.A. Johnson, J. Seidel, R.E. Carson, W.R. Gandler, A. Sofer, M.V. Green, M.E. Daube-Witherspoon, " Evaluation of 3D Reconstruction Algorithms for a Small Animal PET Camera," *IEEE Transactions on Nuclear Science*, vol. 44, no. 3, pt.2, p. 1303-1308, June 1997.

[54] S. Weber, A. Terstegge, H. Herzog, R. Reinartz, P. Reinhart, F. Rongen, H.W. Muller-Garmer and H. Halling, "The Design of an Animal PET: Flexible Geometry for Achieving Optimal Spatial Resolution or High Sensitivity," *IEEE Transactions on Medical Imaging*, vol. 16, no. 5 , pp. 684-689, 1997.

[55] A. del Guerra, F. de Notaristefani, G. Di Domenico, T. Malatesta, R. Pani, R. Pellegrini, A. Turra, F. Vittori and G. Zavattini, "YAP:Ce Scintillator Coupled to a Position sensitive Photomultiplier for High Spatial Resolution Positron Emission Tomography," *Proceedings of the International Conference on Inorganic Scintillators and Their Applications, SCINT95*, pp. 17-20, 1996.

[56] D. Townsend, P. Frey, A. Jeavons, G. Reich, H.J. Tochon-Danguy, A. Donath, A. Christin and G. Schaller, "High density avalanche chamber (HIDAC) positron camera," *Journal of Nuclear Medicine*, vol. 28, no. 10, pp. 1554-1562, Oct. 1987.

[57] G. Charpak, *Annual Reviews of Nuclear Science*, vol 20, p. 195, 1970.

- [58] D.L. Hastings, J.V. Moore, M.L. Waller, P.D. Acton, N.J.F. Dodd, J.C. Hand, P.M. Nuttall, and A.P. Jeavons, "High Resolution PET Imaging of Tumours in Mice," Oxford Positron Systems Ltd., Oxford, UK, 1995.
- [59] M. Watanabe, H. Uchida, H. Okada, K. Shimizu, N. Satoh, E. Yoshikawa, T. Ohmura, T. Yamashita, E. Tanaka, "A High Resolution PET for Animal Studies," *IEEE Transactions on Medical Imaging*, vol. 11, no. 4, pp. 577-580, Dec. 1992.
- [60] M. Watanabe, H. Okada, K. Shimizu, T. Omura, E. Yoshikawa, T. Kosugi, S. Mori, T. Yamashita, "A High Resolution Animal PET Scanner Using Compact PS-PMT Detectors," *IEEE Transactions on Nuclear Science*, vol. 44, no. 3, pt. 2, p. 1277-1282, June 1997.
- [61] C.J. Marriott, J.E. Cadorette, R. Lecomte, V. Scasnar, J. Rousseau, J.E. van Lier, "High-resolution PET Imaging and Quantitation of Pharmaceutical Biodistributions in a Small Animal Using Avalanche Photodiode Detectors," *Journal of Nuclear Medicine*, vol. 35, no. 8, pp. 1390-1396, Aug. 1994.
- [62] O. Fries, S.M. Bradbury, J. Gebauer, I. Holl, E. Lorenz, D. Renker, S.I. Ziegler, "A small animal PET prototype based on LSO crystals read out by avalanche photodiodes," *Nuclear Instruments & Methods in Physics Research, Section A*, vol. 387, no. 1-2, p. 220-224, March 1997.
- [63] X. Liu, S. Rajeswaran, W. Smolik, S. Tavernier, S. Zhang, and P. Bruyndonckx, "Design and Physical Characteristics of a Small Animal PET Using BaF₂ Crystals and a Photosensitive Wire Chamber," *Nuclear Instruments & Methods in Physics Research, Section A*, vol. 382, no. 3, pp. 589-600, 1996.
- [64] P. Bruyndonckx, X. Liu, S. Tavernier, and S. Zhang, "Performance Study of a 3D Small Animal PET Scanner Based on BaF₂ Crystals and a Photo Sensitive Wire Chamber," *Nuclear Instruments & Methods in Physics Research, Section A*, vol. 392, no. 1-3, pp. 407-413, 1997.
- [65] Company literature, Integrated Detector and Electronics as, Hovk, Norway.
- [66] A.G. Weisenberger, S. Majewski, M. Saha, and E. Bradley, "Coincident Radiation Imaging of Iodine 125 for *In Vivo* Gene Imaging in Small Animals," *Nuclear Instruments & Methods in Physics Research*, vol. A392, pp. 299-303, 1997.
- [67] A.G. Weisenberger, E. Bradley, S. Majewski, and M. Saha, "Development of a Novel Radiation Imaging Detector System for *In Vivo* Gene Imaging in Small Animal Studies," *IEEE Transactions on Nuclear Science*, vol. 45, no. 3, pp. 1743-1749, June, 1998.
- [68] A.G. Weisenberger, E. Bradley, S. Majewski and M. Saha "A CsI(Na) Based Radiation Detector for High Resolution Imaging Studies Using Iodine 125 in Small Animal Research," *Proceedings of SPIE*, vol. 3115, pp.254-262, 1997.
- [69] A.G. Weisenberger, B. Kross, S. Majewski, R. Wojcik, E. Bradley and M. Saha "Design Features and Performance of a CsI(Na) Array Based Gamma Camera for Small

Animal Gene Research," 1997 IEEE Nuclear Science/Medical Imaging Conference, Albuquerque, Nov., 1997.

[70] M.K. Dewanjee, A.K. Ghafouripour, M. Kapadvanjwala, E.L. Oates, A. Krishan, D.M. Lopez, A.N. Serafini and G.N. Sfakianakis, "Radiolabeled Antisense Oligodeoxynucleotides: In Vitro and In Vivo Application," *Journal of Clinical Immunoassay*, vol. 16, no. 4, p. 276, 1993.

[71] M.K. Dewanjee, A.K. Ghafouripour, M. Kapadvanjwala, S. Dewanjee, A.N. Serafini, D.M. Lopez and G.N. Sfakianakis, "Noninvasive Imaging of c-myc Oncogene Messenger RNA with Indium-111-Antisense Probes in a Mammary Tumor-Bearing Mouse Model," *Journal of Nuclear Medicine*, vol. 35, no. 6, pp. 1054-1063, June 1994.

[72] M.K. Dewanjee, "Radiolabeled Antisense Probes: Diagnosis and Therapy," *Diagnostic Oncology*, vol. 3, pp. 189-208, 1993.

[73] K.G. Peters, P.S. Rao, B.S. Bell & L. A. Kindman, "Green Fluorescent Fusion Proteins: Powerful Tools for Monitoring Protein Expression in Live Zebrafish Embryos," *Dev. Biol.*, vol. 171 pp. 252-257, 1995.

[74] G. Taubes, "Firefly Gene Lights up Lab Animals from Inside Out," *Science*, vol. 276, p. 1993, 27 June, 1997.

[75] T. Gura, "Jellyfish Proteins Light Up Cells," *Science*, vol. 276, p. 1989, 27 June, 1997.

[76] J.G. Tjuvajev, G. Stockhammer, R. Desai, H. Uehara, K. Watanabe, B. Gansbacher and R.G. Blasberg, "Imaging the expression of transfected genes *in vivo*," *Cancer Research. (CNF)*, vol. 55, no. 24, pp. 6126-32, Dec 15, 1995.

[77] J.G. Tjuvajev, R. Finn, K. Watanabe, R. Joshi, T. Oku, J. Kennedy, B. Beattie, J. Koutcher, S. Larson and R. G. Blasberg, "Noninvasive imaging of herpes virus thymidine kinase gene transfer and expression: a potential method for monitoring clinical gene therapy," *Cancer Research. (CNF)*, vol. 56, no. 18, pp. 4087-95, Sep 15, 1996.

[78] J.D. Watson, M. Gilman, J. Witkowski, M. Zoller, Recombinant DNA, 2nd edition, pp. 216-217, 1992.

[79] M. Sasaki, H.W. Muller-Gartner, J.R. Lever, H.T. Ravert, R.F. Dannals, T.R. Guilarte and H.N. Wagner Jr., "Assessment of Brain Muscarinic Acetylcholinergic Receptors in Living Mice Using a Simple Probe, [¹²⁵I]-4-Iododexetimide and [¹²⁵I]-4-Iodolevetimide," *Neuropharmacology*, vol. 32, no. 12, pp. 1441-1443, 1993.

[80] C.M. Lederer, and V.S. Shirley, *Table of Isotopes*, 7th ed., John Wiley & Sons, Inc., New York, 1978.

[81] M.K. Dewanjee, Radioiodination: Theory, Practice, and Biomedical Application, Kluwer Academic Publisher, Boston, 1992.

- [82] D. L. Horrocks and P. R. Klein, "Theoretical Considerations for Standardization of ^{125}I by the Coincidence Method," *Nuclear Instruments & Methods in Physics Research.*, vol. 124, pp. 585-589, 1975.
- [83] A.K. Drukier, "MultiPhoton Detection," *Workshop on Ultrahigh Sensitivity Quantification Methodologies and Instrumentation for Biomedical Applications*, NIST, Gaithersburg, MD, July 1995.
- [84] F.F. Knapp Jr and S. Mirzadeh "Radionuclide Production: Reactors," in Principles of Nuclear Medicine, 2nd edition, eds: H.N. Wagner Jr, Z. Szabo, and J.W. Buchanan, W.B. Saunders Company, pp. 135-144, 1995.
- [85] H. Kume, S. Muramatsu and I. Masahiro, "Position sensitive Photomultiplier Tubes for Scintillation Imaging", *IEEE Transactions in Nuclear Science*, vol. -33:359-369, 1986.
- [86] R. Pani, F.Scopinaro, G.Depola, R.Pellegrini, A.Soluri; "Very High Resolution Gamma Camera Based on Position sensitive Photomultiplier Tube," *Physica Medica*, vol. 9. no. 2-3, pp. 233-236, 1993.
- [87] N.J. Yasillo, R.A. Mintzer, J.N. Aarsvold, R.N. Beck, T. A. Block, C.T. Chen, M. Cooper, S.F. Heimsath, K.L. Mathews, C.E. Ordonez, X. Pan, T.C. Vazquez, and C. Wu, "A Single-Tube Minature Gamma Camera," *Conference Record of the 1993 IEEE Medical Imaging Conference*, Vol 2, 1073-1076, 1994.
- [88] Photomultiplier Tube: Principle to Application, Hamamatsu Corporation, 1994.
- [89] D. Steinbach, S. Majewski, M. Williams, B. Kross, A.G. Weisenberger and R. Wojcik, "Development of a Small Field of View Scintimammography Camera Based on a YAP Crystal Array and a Position sensitive PMT," *Conference Record of the 1996 IEEE Medical Imaging Conference*, pp. 1251-1256, 1996.
- [90] A. Breskin, G. Charpak, C. Demierre, S. Majewski, A Policarpo, F. Sauli and J. C. Santiard, "High-Accuracy, Bidimensional Read-Out of Proportional Chambers with Short Resolution Times, *Nuclear Instruments & Methods in Physics Research A*, vol. 143, pp. 29-39, 1977.
- [91] E. Gatti, A. Longoni, H. Okuno, and P. Semenza, "Optimum Geometry for Strip Cathodes or Grids in MWPC for Avalanche Localization Along the Anode Wires," *Nuclear Instruments & Methods in Physics Research*, vol. 163, pp. 83-92, 1979.
- [92] Sparrow Corporation, Starkville, MS.
- [93] S. Baccaro, K. Blazek, F. de Notaristefani, P. Maly, J.A. Mares, R. Pani, R. Pellegrini and A. Soluri, "Scintillation properties of YAP:Ce," *Nuclear Instruments & Methods in Physics Research A*, vol. 361, pp. 209-215, 1995.
- [94] Isotope Products Laboratories, Burbank, CA.

- [95] Hamamatsu Technical Data, "Position Sensitive Photomultiplier Tubes with Crossed Wire Anodes R2486 Series," Hamamatsu Corporation, Bridgewater N.J, Aug, 1989.
- [96] NIH Image for Macintosh Computer, available from National Institutes of Health, Bethesda, MD.
- [97] P. J. Morgan, P. Barrett, H. E. Howell and R. Helliwell, "Melatonin Receptors: Localization, Molecular Pharmacology and Physiological Significance," *Neurochem Int.* vol 24, no. 2, pp. 101-146, 1994.
- [98] Amersham Pharmacia Biotech Inc., Piscataway, NJ.
- [99] G.F. Knoll, "Chapter 3: Counting Statistics and Error Prediction," in Radiation Detection and Measurement, pp. 65-102, John Wiley and Sons, Inc., New York, 1989.
- [100] Hilger Analytical Ltd., Kent, England.
- [101] A. Truman, A.J. Bird, D. Ramsden and Z. He, "Pixellated CsI(Tl) arrays with position sensitive PMT readout", *Nuclear Instruments and Methods in Physics Research A*, 353(1994) pp. 375-378, 1994.
- [102] Scionix Holland B.V., Bunnik, the Netherlands.
- [103] Thermo Electron -Tecomet, Precision Assemblies Operations, Woburn, MA.
- 104 Dr. John Lever, Department of Environmental Health Sciences, Johns Hopkins University, private communication, 1998.
- [105] T. Mochizuki, V.L. Villemagne, U. Scheffel, X. Liu, J.L. Musachio, R.F. Dannals, and H.N. Wagner Jr, "A simple probe measures the pharmacokinetics of (125I)RTI-55 in mouse brain in vivo," *European Journal of Pharmacology*, vol. 338, pp. 17-23, 1997.
- [106] J.W. Boja, M.W. Mitchell, A. Patel, T.A. Carroll, F.I. Lewin, P. Abraham, and M.J. Kuhar, "High-affinity binding of (¹²⁵I)RTI-55 to dopamine and serotonin transporters in rat brain," *Synapse*, vol. 12, pp. 27-36, 1992.
- [107] U. Scheffel, R.F. Dannals, E.J. Cline, G.A. Ricaurte, F.I. Carrol, P. Abraham, A.H. Lewin, and M.J. Kuhar, "[¹²³I / ¹²⁵I]RTI-55, an in vivo label for serotonin transporter," *Synapse*, vol. 11, pp. 134-139, 1992.
- [108] E.K. Shaya, U. Scheffel, R.F. Dannals, G.A. Ricaurte, F.I. Carroll, H. Wagner Jr, M.J. Kuhar, and D.F. Wong, "In vivo imaging of dopamine reuptake sites in the primate brain using single photon emission computed tomography (SPECT) and iodine-123 labeled RTI-55," *Synapse*, vol. 10, pp. 169-172, 1992.
- [109] S. Agrawal, Z.Jiang, Q. Zhao, D. Shaw, and A. Roskey, "Mixed-backbone oligonucleotides as second generation antisense oligonucleotides: in vitro and in vivo studies," *Proceedings of the National Academy of Science*, vol 94, no. 6, pp. 2620-2625 18 March, 1997.

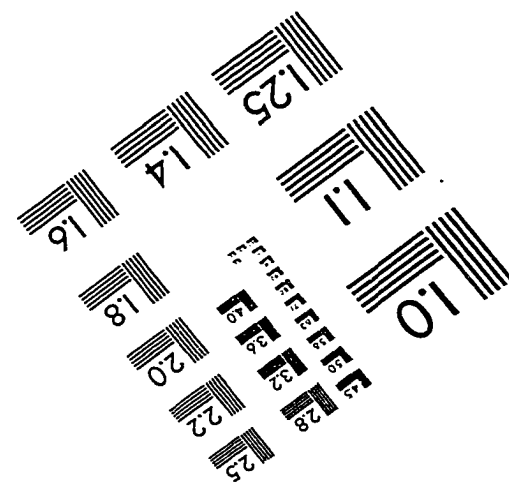
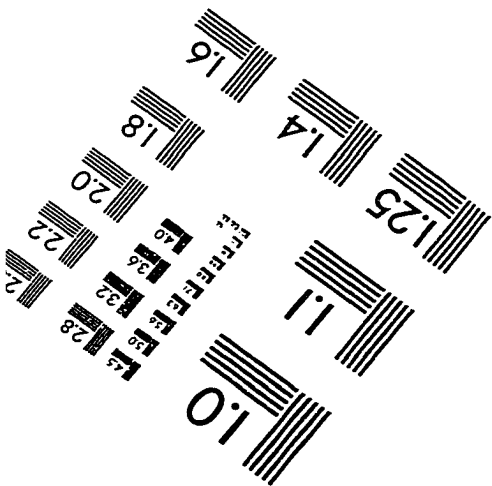
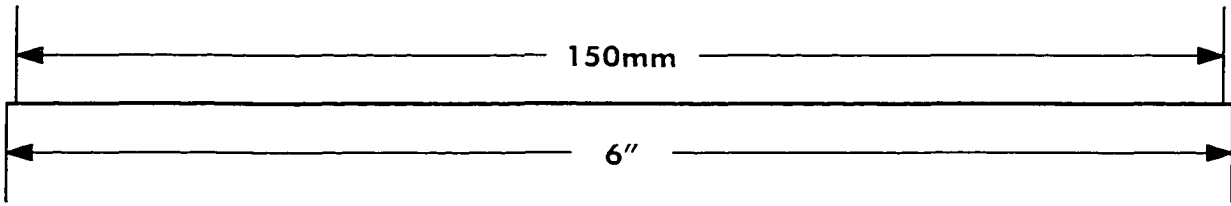
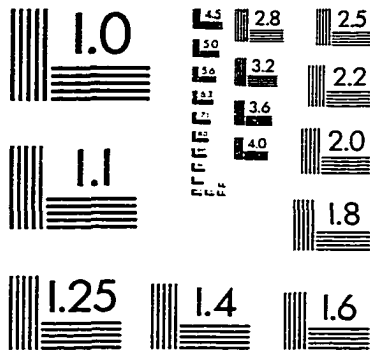
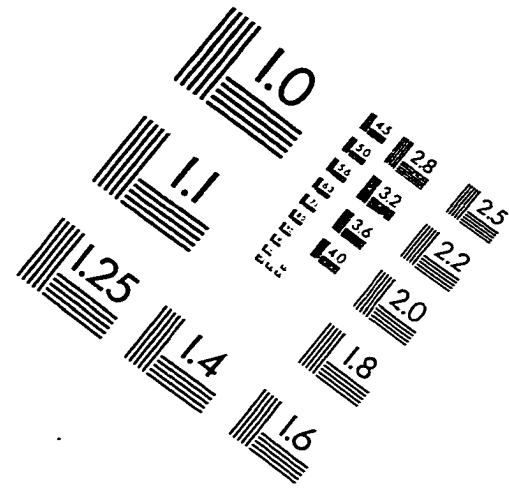
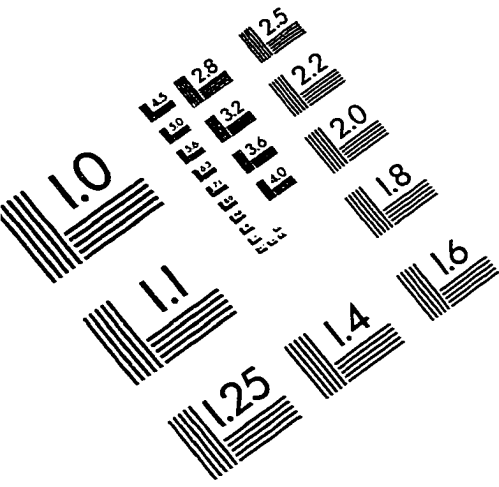
- [110] Dr. Mark Williams, Dept of Radiology, University of Virginia, private communication, 1998.
- [111] Dr. Henry Wagner, Jr, Divisions of Nuclear Medicine and radiation Health Science, Johns Hopkins University, private communication, 1998.
- [112] Dr. Amos Breskin, Weizzman Institute of Science, Rehovot, Israel, private communication, 1998.
- [113] J.D. Watson, M. Gilman, J. Witkowski, M. Zoller, Recombinant DNA, 2nd ed., W.H. Freeman and Co., New York, 1992.
- [114] B. Lewin, Genes V, Oxford University Press, New York, 1994.
- [115] G. Taubes, "Firefly Gene Lights up Lab Animals from Inside Out," *Science*, vol. 276, p. 1993, 27 June, 1997.
- [116] T. Gura, "Jellyfish Proteins Light Up Cells," *Science*, vol. 276, p. 1989, 27 June, 1997.
- [117] W.D. Ehman and D.E. Vance, Radiochemistry and Nuclear Methods of Analysis, John Wiley and Sons, Inc., New York, 1991.
- [118] Super-Kamiokande Collaboration, "Evidence for Massive Neutrinos," *Super-Kamiokande Press Release*, Takayame, Japan, June 5, 1998.
- [119] C.M. Lederer and V.S. Shirley, Table of Isotopes, 7th ed., John Wiley & Sons, Inc., New York, 1978.

Vita

Andrew Gerard Weisenberger

Drew was born in West Chester, Pennsylvania on August 4th, 1957. He attended Devon Preparatory School in Devon, Pennsylvania and graduated in June, 1976. In May of 1980 he received his Bachelor of Science degree in Astronomy with a minor in Physics from Villanova University in Villanova, Pennsylvania. Drew received his Masters of Science degree in Astronomy from the University of Florida in Gainesville, Florida in May of 1985. While a graduate student and following graduation from the University of Florida, Drew was employed by the Space Astronomy Laboratory/Space Science Institute in Gainesville, Florida. In 1990, Drew left Gainesville and joined the staff of the Detector Development Group in the Physics Division at Thomas Jefferson National Accelerator Facility (formerly CEBAF) in Newport News, Virginia. Drew intends to continue detector development for biomedical and nuclear physics applications at Thomas Jefferson National Accelerator Facility.

IMAGE EVALUATION TEST TARGET (QA-3)



APPLIED IMAGE, Inc
1653 East Main Street
Rochester, NY 14609 USA
Phone: 716/482-0300
Fax: 716/288-5989

© 1993, Applied Image, Inc., All Rights Reserved